Hill, Max John Samuel (2024) *Furthering the understanding and 3D printing of dipeptide based low molecular weight hydrogels.* PhD thesis.

https://theses.gla.ac.uk/84512/

Furthering the Understanding and 3D Printing of Dipeptide Based Low Molecular Weight Hydrogels

Max John Samuel Hill

Submitted in fulfilment of the requirements for the Degree of Doctor of Philosophy

School of Chemistry

College of Science and Engineering

University of Glasgow

April 2024

Abstract

Hydrogels produced from Low Molecular Weight Gelators (LMWGs) are an extremely versatile class of material, with a myriad of applications. However, many aspects of these materials are still not well understood. These gels can be formed via a range of methods, yet are inherently fickle in their formation, with minute differences within the gelation processes often causing significant changes to the properties of the final materials produced. As such, some important variables during gelation can be overlooked and are assumed to be insignificant, which is not always the case. Even for those variables that are shown to have an effect, this does not necessarily apply to similar low molecular weight gels formed via different gelation triggers. This Thesis will explore some additional considerations for low molecular weight gels, whilst further developing their suitability for 3D printing towards biomedical applications.

First, we demonstrate the successful 3D printing of two *N*-protected dipeptide based low molecular weight hydrogels in tandem to produce multi-layered 3D printed gel samples. Each gel differs in mechanical properties. Thus, through oscillatory rheology, we show changes to the overall sample mechanical properties depending on the number and ordering of the different printed gel layers. These findings were compared to non-printed equivalent multi-layered gel samples. Whilst inherently stiffer, the non-printed gel samples displayed the same trends in mechanical properties as the printed gels. We then explored the borders between separately printed gels via confocal microscopy and determined a lack of interface, with printed strips of gel remaining discrete and maintaining clear boundaries. This separation was highlighted through confocal microscopy experiments incorporating multiple different fluorescent dyes.

Secondly, we probe the impact of imposed spatial constraints on two different low molecular weight hydrogels. Gels were produced using either a solvent-switch or pH gelation trigger within different sized vessels and their localised mechanical properties compared via cavitation rheology. These were compared to differences in network microstructure observed by confocal microscopy. Solvent-triggered gels displayed differences both in network microstructure and localised mechanical properties when formed in different sized vessels, whilst pH triggered equivalent gels did not. The former possesses a more compartmentalised microstructure of the underlying gelator network whilst the latter is instead underpinned by a more uniform network. These network differences align with the different responses to imposed spatial constraints between the two differently triggered gels. This study was expanded to gels formed in non-uniform vessels with smaller and larger portions, the results of which further confirmed initial observations.

Finally, we explore the surface of different supramolecular hydrogels for any potential differences in the underlying gelator network here. As an initial step towards better understanding the application of needle-induced cavitation rheology to low molecular weight gels, needle puncture experiments were performed on solvent and pH triggered gels. These initially alluded to a difference in the gelator network at the gels surface. Through confocal microscopy we observed changes within fibre alignment and density within the microstructure close to the surface of these gels. However, in subsequent oscillatory rheology and nanoindentation experiments we saw no difference in the mechanical properties. These observations were confirmed by follow up puncture data, which confirmed initial surface related data to be an instrument artefact.

Acknowledgements

To start, I can't thank my supervisor Prof. Dave Adams enough. Thank you for the constant support, advice and guidance over the last 3.5 years. Without that (very relaxed) initial zoom call, I would never have started a PhD and moved to Glasgow. Ever since, you have been great, being reasonable and always understanding as a supervisor, yet pushing me to do my best and make the most of the PhD. During the overwhelming or difficult moments you were always available to help nullify the worries and put it into perspective with a plan or a simple 'chill out'. I'll miss our weekly chats, including your occasional disbelief at my musical ignorance. I finally worked out hanging captions.

Thank you to the School of Chemistry and all of the staff that have supported my research and made it a wonderful place to work. Thank you to Dr Steven Magennis for your support and time. Special thanks to Dr Chris Syme and Dr Ben Russell for their constant microscope support and good (often unrelated) chat, especially when it (quite literally) went bang.

I thank my examiners Dr Bernhard Schmidt and Dr Tom McDonald for taking the time and effort to read through and help to improve this Thesis. I don't envy you having to pick through it in the slightest!

I thank the Graduate School for the funding that enabled me to visit the US for a research trip, greatly enhancing my PhD experience. Thank you to Prof. Al Crosby and the Crosby group for hosting me during my time at UMass, you were all lovely and it was a wonderful enriching experience that taught me so much and one that I'm extremely grateful for. Especially to Jennifer and Gabriela for looking after and helping me day to day, even once I'd returned home.

A massive thank you to all the Adams and Draper group members past and present that I've had the joy to work alongside and be guided by. To Bart, thank you for ALL the support, in just about everything. From synthesising gelators for me at the start to building the 3D printer and cavitation rheometer (and constantly having to fix or maintain them), I'm beyond grateful for everything, our lab would grind to a halt without you. I will miss seeing your new whacky (and usually perfectly over complicated, but wonderfully so) contraptions or projects. Alex, thank you for the wide-ranging support and top office banter, I can't wait to hear all about the Loch group one day. Dipankar, thank you for your support with nanoindentation and collecting data on my behalf. Ana Mari, thank you for helping me start out in the lab, showing me the ropes and just being lovely. Lisa, thank you for patiently putting up with all my silly questions or giving me encouragement after nervous presentations. Courtenay, Libby, Becky and Jakki, thank you for help and support. Chloe and Rebecca, thank you for all the good laughs, occasional shared panics and good times at conferences. Simona, I can't thank you enough for all the scattering and fitting guidance and support, you rock. Nick and Connor, thank you for all the outrageous laughs. Rui, always keep your chin up and never lose your can-do attitude, I hope to be 10% as enthusiastic as you one day. Emma, thank you for listening to me prattle on about confocal and cavitation, the mantle is yours now. Fin, it was great to see you come back for the PhD, I just wish it had been sooner to enable more laughs.

Thank you to my school chemistry teachers, Mr Sharp and Mrs Aggrey. Mr Sharp you instilled in me my love of chemistry, kicking off my journey and eventually leading me to this point today. You saw and nurtured my interest in the subject, leading me to want to take it further. I still envision a mole, a sheep and a dumbbell to remember the formula. Mrs Aggrey, I have never had as memorable a teacher as you, the definitions you narrated to us will forever be etched permanently into my memory. You helped me decide to pursue chemistry at uni when I was on the fence.

To all my friends who helped me settle, keep busy and sane during my time here, I can't thank you enough. Nick and Matthew, two of my earliest friends up here, I'll never forget the memories of initially meeting you both. From Nick turning up on my doorstep as a complete stranger to find me sleeping on a mattress with all my stuff scattered around it cult ritual style, having just moved in the night before, to just casually letting himself in my flat unannounced nowadays. Or to my first interaction with Matthew being to dump him upside down and make him swim out of a boat. Or team meals, drinks or brews, all have been great. Calum, Rosie, Fi, Ruth, Osh and Erin, the slightly later, but just as welcome, additions. Thanks for all the paddles, good times and putting up with this grumpy PhD student. To Andrew, Brianna and Gregor, my climbing pals, thanks for all the good times, good laughs and helping me develop a sport I found far, far too late. To Simon, Miro and the rest of Granite, I just wish I had met you all sooner, but thank you for putting up with my polo mediocrity. Simon - I can't wait till we can spend our days modding cars and boats in a vet funded garage.

To Helena, thank you for always checking in and putting up with my crap. To Peter, thank you for all the hilarious memories, beers, dinners and paddling. You are one of the smartest people I know, yet also one of the most humble.

Jack and Jamie, thank you for all the support I could ever ask for moving up here, from spare key storage to airport lifts, to dinners and beers. Not many people are lucky enough to have two of their longest friends five minutes down the road. Jack, my best mate and forever the fool, thanks for the support, beers/brandies and front-room karaoke to help get me through from start to finish.

I thank all my family for their support, love and listening to me waffle on about gels at Christmas.

To my nan and grandad, two of the people who mean most to me in this world and to which I owe a great many opportunities. As, at times, stand in parents and forever my biggest fans (despite one of them thinking I'm a pharmacist and the other constantly joking about never expecting me to finish) I am forever grateful for you both.

To Kaitla, my entire world and my person, thank you for everything. You brighten every single one of my days and have kept me going when I had had enough. You kept me motivated, supported me and kept me chugging along through the final slog. You are without doubt the best thing to come out of my time here.

Last, but by no means the least, I owe my biggest thank you to my mum Julie. I owe everything I am, all the opportunities I had, to you. You smashed it as a single mum and I never went without or felt anything less than privileged to be raised by a single parent. You saw a desire to learn in me and made sure I pushed myself always. Thank you for accepting me moving away (and then further), even though I know it was hard. Thank you for your support during the hard, and harder times during the last few years. You have enabled and encouraged me to develop and grow into the person I am. Thank you.

Declaration of Authorship:

I, Max J. S. Hill, declare that, except where explicit reference is made to the contribution of others, this Thesis is the result of my own work and has not been submitted for any other degree at the University of Glasgow or any other institution. The research was carried out at the University of Glasgow between 2020 – 2024, under the supervision of Professor Dave J. Adams.

- *Max J. S. Hill*

List of publications arising from this thesis:

Multi-layer 3D printed dipeptide-based low molecular weight gels
M. J. S. Hill and D. J. Adams, *Soft Matter*, 2022, **18**, 5960-5965.

Effect of imposing spatial constraints on low molecular weight gels
M. J. S. Hill, A. M. Fuentes-Caparrós and D. J. Adams, *Biomacromolecules*, 2023, **24**, 9, 4253-4262.

Abbreviations

δ	Indentation
Φ_{DMSO}	Volume fraction of DMSO to water
γ	Shear rate
1D	One dimensional
^{1}H NMR	Proton nuclear magnetic resonance
3D	Three dimensional
AFM	Atomic force microscopy
Air SEM	Air scanning electron microscopy
ASEM	Atmospheric scanning electron microscopy
CLSM	Confocal laser scanning microscopy
CRAB	Cavitation rheology analyser box
Cryo-TEM	Cryogenic transmission electron microscopy
D	Aspartic acid
DBS	1,3:2,4-Dibenzylidene-D-sorbitol
DBS-hydrazide	1,3:2,4-Dibenzylidene-D-sorbitol-diacylhydrazide
d_C	Critical depth
DMSO	Dimethyl sulfoxide
DMSO-d_6	Deuterated dimethyl sulfoxide
E	Young's Modulus
E_C	Elastic cavitation modulus
EEO	Electroendosmosis
ESEM	Environmental scanning electron microscopy
F	Phenylalanine
Fmoc	Fluorenylmethyloxycarbonyl
F-δ	Force-displacement
F-z	Force-indentation
G	Glycine
G'	Shear storage modulus
G''	Shear loss modulus
GalC7	*N*-heptyl-D-galactonamide

GdL	Glucono-δ-lactone
GoF	Goodness of fit
H_2O	Water
IR	Infra-red
K	Lysine
L	Leucine
LMWG	Low molecular weight gelator
LVER	Linear viscoelastic region
M	Molar
Nap	2-Naphthylmethyl ether
NMR	Nuclear magnetic resonance
P_C	Critical pressure
PP	Parallel plate
R	Radius
SANS	Small angle neutron scattering
SAXS	Small angle X-ray scattering
SEM	Scanning electron microscopy
TEM	Transmission electron microscopy
UV	Ultraviolet
UV-vis	Ultraviolet-visible
V	Valine
Y	Tyrosine

Table of Contents

Chapter 1

Introduction

1.1 Gels

Gels are a class of soft material that present characteristic traits of both solids and liquids, displaying viscoelastic properties.[1-3] They comprise a spanning solid-like gelator network of interconnected or entangled one-dimensional fibres that immobilise the bulk flow of solvent, yielding a solid-like material.[3]

Gels can largely be categorised into two main groups based on the solvent from which they are predominantly formed. Aqueous solvents give rise to hydrogels and organic solvents give rise to organogels.[4, 5] Both have a multitude of respective applications, with hydrogels often better suited to biomedical applications due to the inherent biocompatibility of their solvent phase.[6, 7]

Gels can also be categorised based on how the underlying network is formed from its constituent building blocks. Those formed from covalent crosslinks connecting polymer chains are called chemical gels,[8] whilst those formed by the self-assembly of components driven by non-covalent intramolecular forces are referred to as physical, or supramolecular gels (Figure 1.1).[9-11] The underpinnings of these classes of material leads to different characteristic properties and thus applications.[1, 12] Chemical gels, due to their stronger covalent linkages, are typically more robust and of a greater mechanical strength than their supramolecular counterparts.[9] Although often possessing lower mechanical properties, physical gels can be responsive to external stimuli.[13-15] This behaviour stems from the relatively weak, and thus reversible, forces from which they are formed.[16] The non-covalent intramolecular forces that anchor the network of gelator fibres, such as ionic, hydrogen bonding, dipole-dipole, π-π stacking and van der Waals interactions are all reversible, allowing for the selective formation and destruction of this type of gel when subject to appropriate stimuli. Solvent-switching,[17-19] temperature cycling,[20] pH change,[21] photoinitiation[22] and introduction of an ionic solution[23, 24] have all been demonstrated as viable methods to allow for the assembly and disassembly of gelator networks.

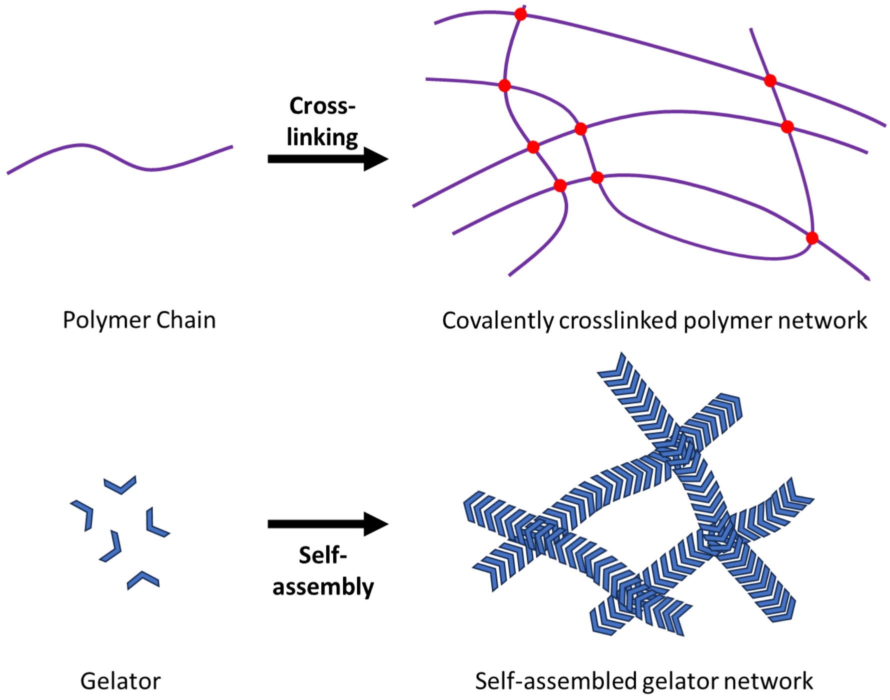

Figure 1.1 Cartoon schematic of (top) chemical and (bottom) supramolecular gel formation.

1.2 Low Molecular Weight Gelators

One class of supramolecular hydrogels arises from the self-assembly of small organic molecules, known as low molecular weight gelators (LMWGs), into anisotropic one-dimensional fibres.[4, 5, 25, 26] The overall aggregated shape of the fibres depends largely on the chemical structure and packing of the gelator molecules, but external factors such as pH, temperature, solvent, or the presence of metal ions can also affect fibre morphology.[24, 27-29] Self-assembly of the monomer LMWG sub-units into one dimensional fibres is driven by the hydrophobic effect, with alignment often reliant on hydrogen bonding and π-π stacking between compatible functional groups.[30] The resulting fibres can then entangle with others to form a solid-like gelator network, resembling a mesh that can immobilise solvent via capillary forces and surface tension,[4, 5] producing a gel (Figure 1.2).[27]

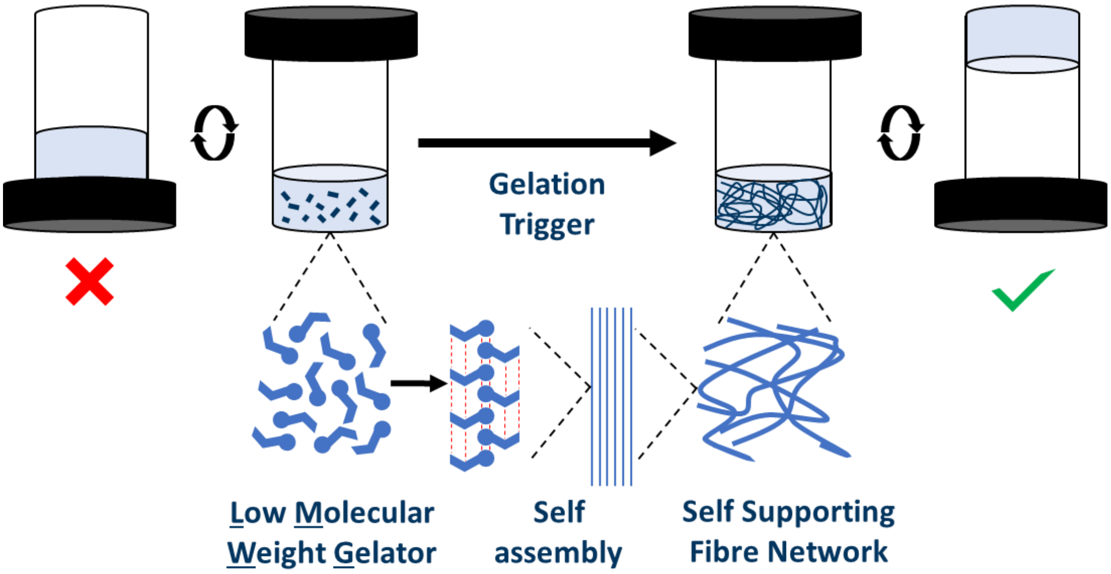

Figure 1.2 Cartoon diagram of hierarchical self-assembly forming low molecular weight gels in vials**.**

Early examples of LMWGs have been known since the late 19th century,[31] with interest slowly rising from the 1930s onwards.[32] Early applications included lubricants, pharmaceuticals and food additives.[10, 33-35] These early systems were typically discovered by serendipity, with efforts largely centred on controlling the end material properties via additives, modulators and processing. It was not until the end of the 20th century that the focus was instead shifted to the foundational molecular building blocks of these materials, and early attempts at rational design of LMWGs began.[26, 32, 36] Since then, the field has been rejuvenated, with exponential growth in novel LMWG systems and countless applications reported.[10, 37] For LMWGs that can entrap water to produce hydrogels, many can be generally classified by the structural motifs they contain (Figure 1.3).[4]

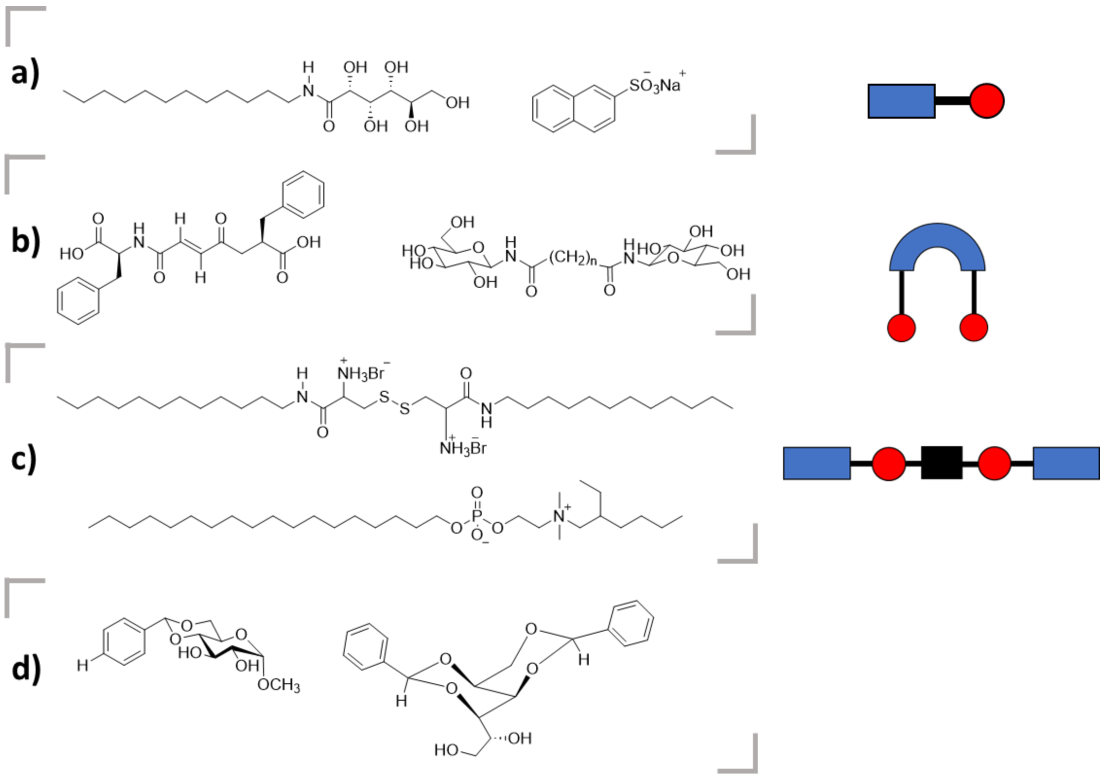

Figure 1.3 Chemical structures of examples of different classes of LMWG, with simplified cartoon representations of key structural motifs**.** a) Amphiphiles b) Bolaamphiphiles c) Gemini Surfactants d) Sugar based LMWGs. Polar hydrophilic groups are shown in red, hydrophobic groups in blue and flexible aliphatic linker chains in black.[4]

Whilst not a definitive, nor necessarily exclusive set of classifications, these do outline some key themes within this class of gelator, as described by Hanabusa.[38] Most LMWGs are relatively small amphiphilic molecules, enabling them to interact with one another as well as surrounding water molecules.[4] It is the balance of these interactions that enables the hierarchical self-assembly of these molecules, and subsequent solvent immobilisation, once an appropriate gelation trigger has been applied. Studying these trends helps to inform the rational design of new LMWGs and as such, has moved the field away from serendipitous discovery to targeted molecular engineering of successful new gelators.[26, 32, 38, 39] Once a new LMWG system has been produced, these often quickly give rise to a related family of LMWGs through subsequent chemical modifications.[20] These can target hydrophilicity,[40] minimum gelation concentration,[5] gelation triggers[21, 22, 41, 42] or desired chemical functionality.[43-45] However, despite much consideration and many attempts, there is still yet to be a definitive set of rules as to whether a molecule will be a successful LMWG or not.[26, 32, 37, 46]

1.2.1 *N*-protected dipeptide LMWGs

One particular family of LMWGs that has garnered a lot of interest over the last two decades are *N*-functionalised dipeptides.[37, 47] First reported in 1995 by Vegners[48] and moving into popular focus around a decade later,[17, 49-51] the study of these LMWGs and the materials they produce have grown exponentially in the last 20 years.[52] These consist of a dipeptide with the *N*-terminus protected through the covalent binding of an appropriate protecting group, commonly Fmoc, Nap or other aromatic moieties (Figure 1.4).[17, 53-55] The aromatic sub-units play a significant role in the self-assembly, and thus gelation, of these LMWGs through π-π stacking.[56, 57]

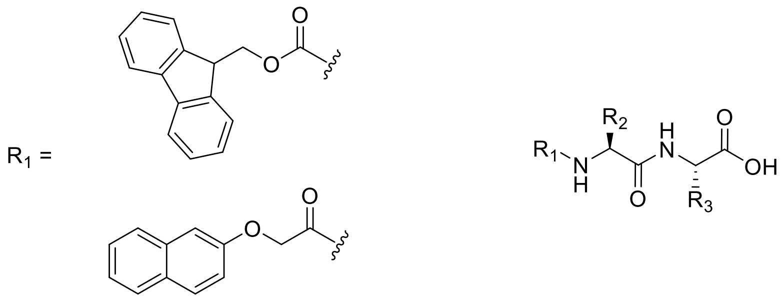

Figure 1.4 General chemical structure of an N-protected dipeptide (right), where R_1 can be an Fmoc (top) or Nap (bottom) protecting group. Both R_2 and R_3 are amino acids side chains.

The modular nature of these gelators allows fine tuning of their properties via the selection of desired side chains and associated functional groups from the corresponding amino acids.[57] Steric bulk,[58] hydrophobicity,[57, 59] chirality[60-63] and even chain length can all be tailored through careful choice of different amino acid building blocks.[64] Couple this with the choice of various protecting groups available to cap the *N*-terminus of the dipeptide and the degree of tuneability is increased yet further.[55, 65, 66] This yields a family of materials with a wide range of potential applications.[67, 68] The dipeptide base gives these LMWGs the potential of inherent biocompatibility, opening up further applications within the biomedical fields provided they are paired with a suitable protecting group,[69] solvent[70-72] and gelation trigger.[73] Here, the Nap protecting group prevails over Fmoc with greater stability at higher pH,[74, 75] as is often encountered when preparing these materials.[18, 21] LMWG decomposition into potentially cytotoxic degradants is therefore less likely when employing this protecting group, bolstering its suitability for biomedical applications.[55, 65, 66]

1.3 Gelation Triggers

1.3.1 pH

Within the literature, gelation of *N*-protected dipeptide LMWG systems is predominantly triggered via pH cycling.[30] The carboxylic acid group at the *C*-terminus is first deprotonated to the carboxylate by raising the pH above the respective pK_a, allowing for dissolution of the now charged gelator in water (Figure 1.5ai). The pH is then subsequently lowered below the pK_a of the gelator, re-protonating the carboxylic acid group. This renders the gelator molecules insoluble and hydrophobic, driving self-assembly (Figure 1.5aii & 1.5aiii).[24, 30, 76] The changes in pH can be achieved most simply by addition of aliquots of base followed by acid but can be refined with the use of a slow acidification trigger based on the hydrolysis of glucono-δ- lactone (GdL). [21, 77] Diffusion of the GdL occurs significantly quicker than its hydrolysis, ensuring for a uniform and gradual pH reduction, promoting homogenous gelation (Figure 1.5b). In addition to these, a pH cycle can be enacted through enzymatic reaction,[78] photoacid[22] or electrochemistry.[79] These methods can lead to finer control over gelation,[79] even allowing for directed spatiotemporal control in some cases.[78-81] pH triggered systems often lead to significantly more homogenous materials than other methods,[21] thus making the mechanical properties more reproducible.[18] This gelation method can also facilitate the straightforward tuning of the final gel properties with respect to pH and mechanical properties, if so desired.[82]

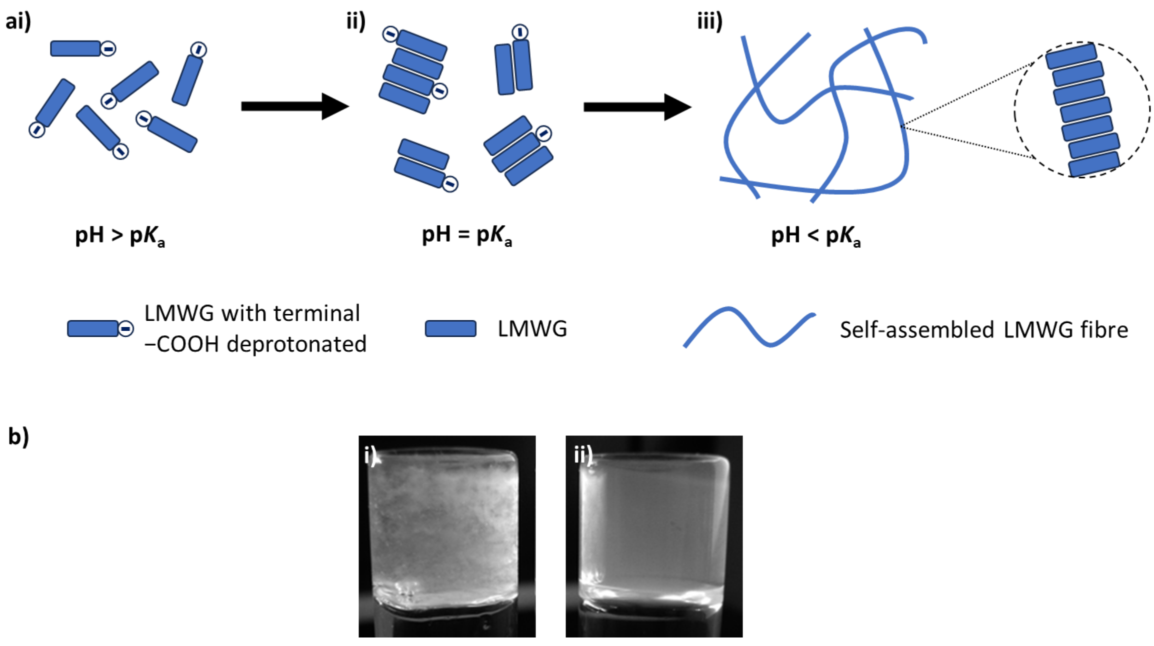

Figure 1.5 a) Cartoon overview of pH triggered gelation process for *N*-protected dipeptide low molecular weight gels. b) Photograph of differences in homogeneity of exemplar pH triggered low molecular weight hydrogels produced via (i) addition of mineral acid or (ii) a slow acidification trigger. Section b is adapted from ref.[21] with permission from the Royal Society of Chemistry.

1.3.2 Solvent-switch

Gelation can also be triggered by a solvent-switch approach, in which the LMWG is first dissolved in a suitable organic solvent, such as DMSO (Figure 1.6).[83-85] This is followed by the addition of water as an anti-solvent, causing a phase separation where the now insoluble gelator molecules are driven to self-assemble.[17] The formation of the gelator network occurs via a nucleation and growth process wherein one-dimensional fibres propagate from nucleation points, growing at the expense of LMWG rich organic solvent droplets which are scavenged and incorporated via Ostwald ripening.[83, 86] Gelation of this type usually occurs rapidly, with simpler preparation and shorter lead times than pH triggered gels.[18]

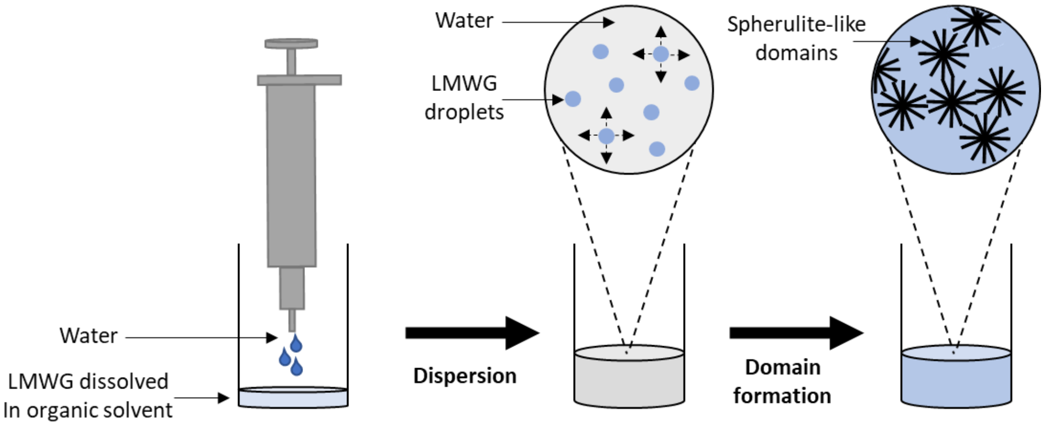

Figure 1.6 Cartoon overview of the solvent triggered gelation process within low molecular weight gels and the resulting spherulite-like domain based microstructure generated.

1.3.3 Heat-Cool

From the above methods we can see that generally for gelation to occur the LMWG is first solubilised and subsequently made insoluble. Whilst both methods are highly effective, gelation can be achieved via a simpler approach; a heat-cool cycle.[1] Here, a LMWG suspension is dissolved into an aqueous LMWG solution by adequate heating, which increases the gelator solubility in water.[87] Upon cooling, the now reduced solubility will drive the LMWG to self-assemble, constructing the gelator network and producing a gel.[20] Thermal cycling is one of the oldest gelation methods, likely owing to the close thermodynamic link to crystallisation.[5] This approach to gelation is prevalent in the polymer gel field,[88] especially within the realm of biopolymers, such as gelatin and agarose.[89-92] As such, it follows that early forays into low molecular weight gels during the fields infancy utilised this method as well.[31, 48]

Despite one of the earliest reports of *N*-protected dipeptide gels being formed by this method,[48] it was not widely adopted for these LMWGs, with pH, solvent or metal ion triggers typically preferred instead.[24] Many LMWGs of this class simply lack the necessary solubility below the solvents boiling point to render this approach viable.[93] For example, FmocFF and NapFF (Figure 1.7), two of the most prevalent and well-studied examples of this gelator class within the literature, are insoluble in water.[53, 93] The additional phenyl rings of the phenyl alanine residues aid self-assembly by providing additional π-π stacking interactions, but increase the hydrophobicity.[94, 95] However, in practice this may not be a significant loss. The heat-cool process can lead to significant variability in the gels produced.[37] Even small deviations in procedure, such as heating rate, cooling rate, vessel size and material (to name but a few) will all impact the final gel properties, hindering their reproducibility.

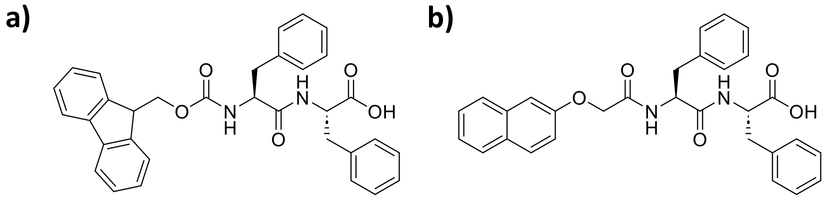

Figure 1.7 Chemical structures of the LMWGs FmocFF (F = phenylalanine) (a) and 2NapFF (b).

Despite the lack of efficacy for the *N*-protected dipeptide LMWGs, this is not to say the heat-cool method is redundant within the realm of low molecular weight gels. Many low molecular weight systems, such as those based on sorbitol derivatives or alkylgalactonamides (Figure 1.8),[20, 96, 97] have been shown to be fully compatible with thermal gelation.

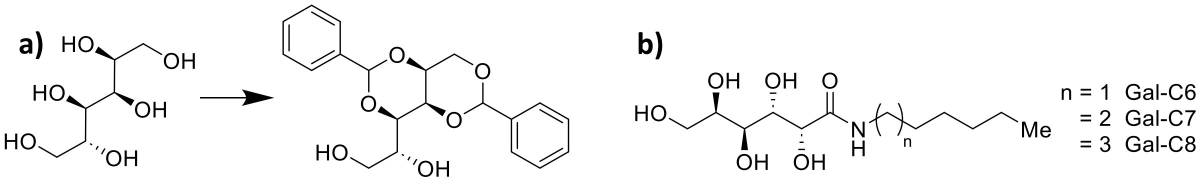

Figure 1.8 Chemical structures of (a) sorbitol and (b) alkylgalactonamide based LMWG systems.

1.4 Differences in Gelator Network Microstructure

It is known now that different gelation triggers, and even variations within preparation methods, lead to distinct low molecular weight gels.[21, 41, 42] This usually results in unique mechanical and other physical properties. These can be linked to observed differences in the underlying gelator network.[41, 84, 98] The morphology adopted by this fibrous network is termed the microstructure,[99] as it is a feature of the realm between the nanoscale molecular assembly and bulk macroscopic material properties. Here, observations can be made via microscopy with regard to fibre size, shape, density, as well as overall network properties, such as pore size or the type of aggregates seen.[100] These vary with applied gelation triggers due to different resulting thermodynamic phase separation mechanisms that produce these underlying architectures.[4]

1.4.1 pH triggered gelator networks

Typically, uniform mesh-like networks are seen in pH triggered gels of *N*-protected dipeptide LMWGs.[18] The LMWG molecules become dissolved in solution when the system pH is high enough to deprotonate the terminal carboxyl group.[76] At this stage, some dipeptide LMWGs will form surfactant-like aggregates.[30] For example, high pH solutions of two related LMWGs, 2NapFF and 2NapVG, form worm-like micelles or spherical micelles respectively (Figure 1.9).[101, 102] Upon a decrease in pH and ensuing re-protonation of the terminal carboxylate groups, the LMWG molecules are rendered insoluble and there is often a shape change of the micellar aggregates.[76] This leads to the formation of a dense fibrous network, wherein both fibre morphology and network mesh size are generally uniform (Figure 1.9aii & aiii).[18, 76]

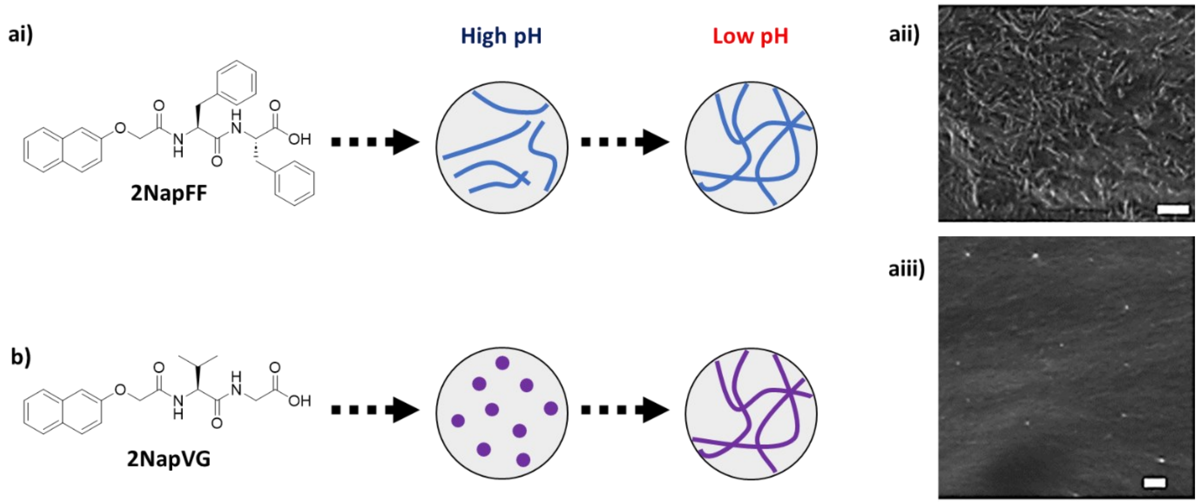

Figure 1.9 Cartoon representations of the self-assembled aggregation behaviour of the dipeptide LMWGs (a) 2NapFF and (b) 2NapVG (V = Valine, G = Glycine) in high pH solutions pre-gelation. 2NapFF forms worm-like micelles whilst 2NapVG forms spherical micelles.[24, 102, 103] Part ai) and b) are reproduced from ref.[103] with permission from Georg Thieme Verlag KG, © 2020. aii) and aiii) show the resulting uniform gelator network underpinning a 2NapFF pH triggered gel via scanning electron microscopy (aii) and confocal microscopy (aiii) as reported by Colquhoun *et al*.[93] All scale bars are 5 µm in length. Figure parts aii and aiii are adapted from ref.[93] with permission from the Royal Society of Chemistry.

1.4.2 Nucleation and growth in solvent and heat-triggered gelator networks

Solvent and heat-triggered low molecular weight gels instead adhere to a nucleation and growth phase separation process (Figure 1.10).[4, 104, 105] The overarching network is constructed from fibre growth stemming from discrete nucleation points within the gelator solution.[83] The cause of these nucleation point differs within solvent and heat-triggered systems.[104]

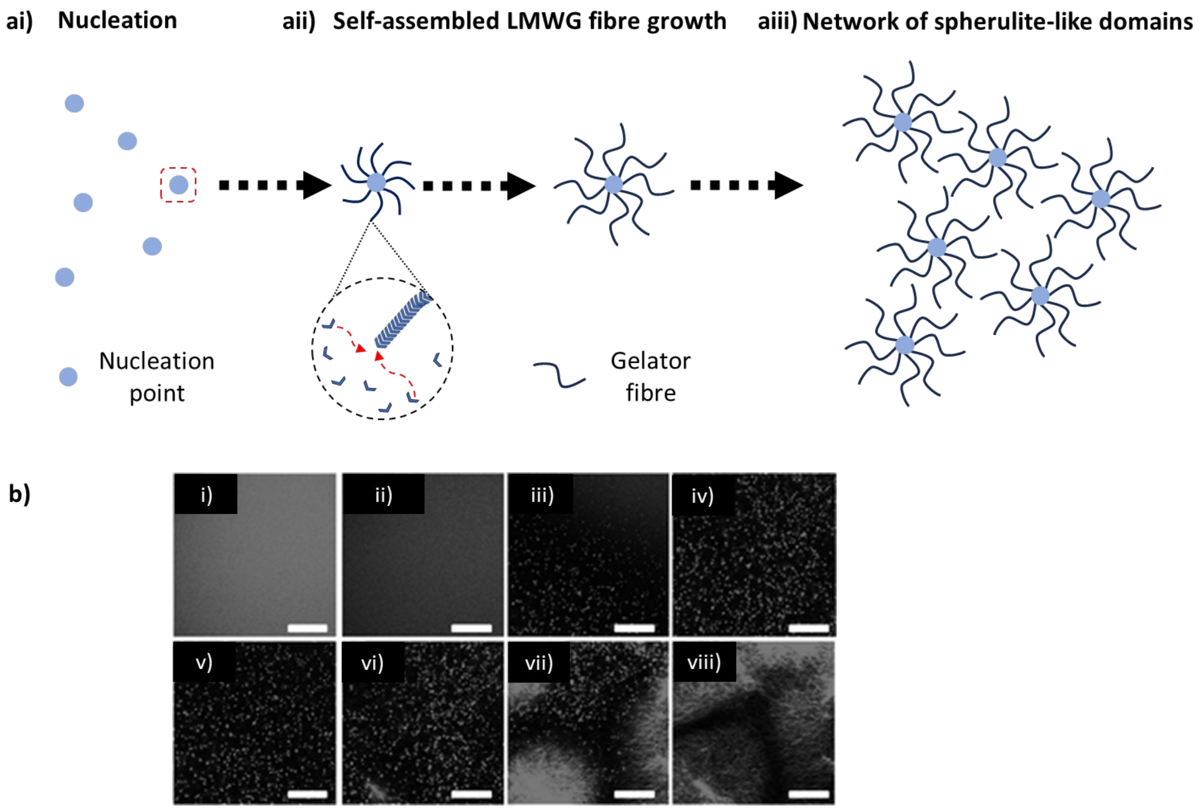

Figure 1.10 a) Cartoon schematic of spherulite-like domain formation through a nucleation and growth process. b) Confocal microscopy images showing nucleation and growth within a solvent triggered FmocLG low molecular weight gel taken over the first two minutes after gelation is triggered. Scale bars = 20 µm. Figure part b) is reproduced from ref.[41] with permission from the Royal Society of Chemistry.

Within the solvent-triggered networks, the addition of a non-favourable anti-solvent, typically water, to the dissolved LMWG solution yields a colloidal dispersion of LMWG rich organic solvent droplets suspended throughout the water component (Figure 1.10ai).[41, 106] This is entropically unfavourable and if coupled with an appropriate solvent: anti-solvent system such as DMSO: water, wherein the two separate solvent phases are miscible and interact favourably with one another, will thermodynamically drive the self-assembly of LMWG molecules (Figure 1.10aii).[107] Fibres therefore start to grow from some of these super-saturated droplets which act as random nucleation points. Multiple fibres can stem from the same point and growth is most likely closer to the centre of these droplets, where there are the most available molecular building blocks. This leads to the radial propagation of fibres, leading to spherulite-like domains, reminiscent of those commonly seen in organogel systems (Figure 1.10aiii).[107-109] These spherulites will grow at the expense of other LMWG rich droplets through Ostwald ripening as gelation continues.[83, 86] In some cases, this process will give rise to a fibrillar network wherein these spherulites act as the junctions between fibres.[106] However in others they remain relatively distinct, tethered to one another by spanning fibres between domain centres. This leads to a significantly less uniform, more compartmentalised overall microstructure, with fluctuations in fibre size and density, but also spherulite size and morphology.[106] Variations at this domain level are expected between different LMWGs, but have also been shown to be sensitive to different solvents,[84] solvent ratios,[41] temperature,[106] and even vessel size.[110] All of which typically correlate to a measurable change in bulk physical properties, such as turbidity or viscoelastic response.[41]

Heat-cool triggered gelation systems create underlying gelator networks following this overall nucleation and growth process in a similar manner, with a few key differences.[4, 87, 111] There is no 'good' solvent within this system, so the nucleation points are not a result of organic solvent droplets saturated with LMWG. Instead, the system is heated to the point at which solubility increases enough to allow for complete LMWG dissolution. Following this, nucleation events occur spontaneously at random points throughout the single phase LMWG solution once the system has cooled down past the T_{gel} temperature. At this point solubility has decreased enough to thermodynamically drive the nucleation and subsequent self-assembly of the now poorly soluble LMWG. In this way, thermal gelation is a closely related mechanism to that underpinning crystallisation, even sometimes being deemed 'crystallisation gone wrong'.[104] Both are non-equilibrium self-assembly processes, with gels often being formed as the kinetically trapped first product, that in some cases can give rise to a subsequent crystalline thermodynamic product given the right conditions (Figure 1.11).[83]

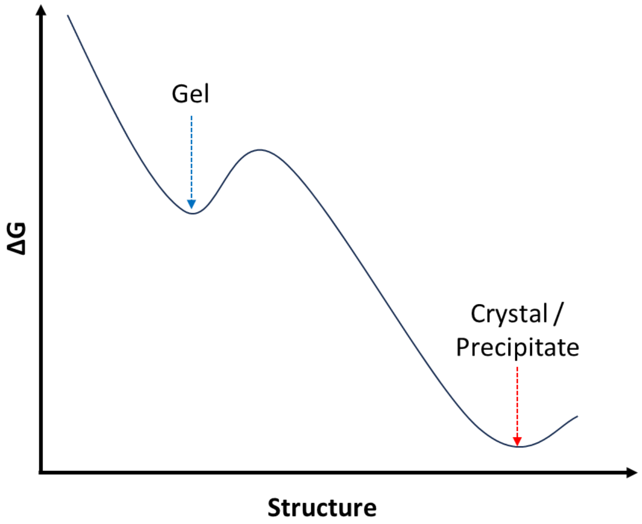

Figure 1.11 Potential thermodynamic pathways to gels as a kinetically trapped product preceding crystal formation.[83]

Fibre growth again follows a nucleation and growth phase separation process here, propagating out radially from said nucleation points. Spherulite-like domains are therefore also commonly seen within these systems.[107] At this point, there are different routes to overall network formation. In some case, these spherulites will continue to grow, expanding outwards, until they encroach on one another.[112] Spherulite growth is now frustrated as continued expansion is terminated by adjacent bordering domains.[113] This can lead to the overall microstructure of these networks consisting of mutually exclusive spherulites jammed together (Figure 1.12a).[114] An alternate pathway involves spherulites remaining relatively compact, producing the overarching network through the linking and assembly of the spherulites themselves as pre-assembled building blocks to form fibres (Figure 1.12b).[105, 113]

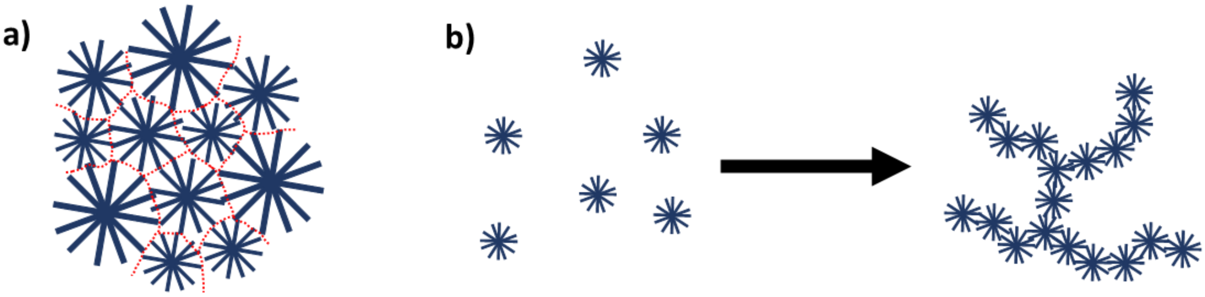

Figure 1.12 Cartoon representations of different routes of growth/assembly for heat-cool gels consisting of spherulite-like domains. a) Spherulite-like aggregates 'jammed' together.[112] b) Overall fibrous network formed from individual domains sequentially joined together.[105]

1.5 Characterisation of Low Molecular Weight Gels

Low molecular weight gels are complex systems, so gaining a better understanding of them through effective characterisation is crucial.[115] Due to their dynamic nature and solid-like properties, gels can be challenging materials to characterise. It often requires the effective combination of a plethora of wide-ranging analytical techniques to fully describe these materials.[37]

1.5.1 Molecular assembly to bulk materials

At the fundamental molecular level, nuclear magnetic resonance (NMR) and infra-red (IR) spectroscopy can be used to analyse and correlate molecular structures pertaining to gelation. NMR and IR can also be used alongside circular dichroism, ultraviolet-visible (UV-vis) and fluorescence spectroscopies to probe molecular packing within microstructures formed upon aggregation and self-assembly of gelator molecules.[116, 117]

Zooming out from the nanoscale, exploration of the underlying microstructures gelator networks adopt under differing conditions enables us to gain further insight into how sensitive these materials truly are. Variations in macroscopic properties can be correlated to observed significant differences within the microscale that we would otherwise be oblivious to.[41] Quantification of bulk mechanical properties are often more relevant when considering real-world applications of these materials.[118]

1.5.2 Electron microscopy

Traditionally within the field, electron microscopy has been used to probe the microstructure of gelator networks.[115] Scanning electron microscopy (SEM) has long been used to visualise the mesh-like gelator network within gels (Figure 1.13). Its use has provided insight into fibre thickness, size, and density, even allowing for clear identification of different networks within multi-component systems.[93, 119]

However, for this technique to be effectively applied to gels, samples require extensive drying under high vacuum and sputter coating with metal.[120, 121] This removes the solvent and is therefore actually characterising the corresponding xerogels instead of the native hydrated gel. It follows that this would alter the network within drastically given these materials are normally ≥ 99% solvent but, at the very least, would be expected to result in substantial drying artefacts that cause significant deviation from the true native structure.[122, 123]

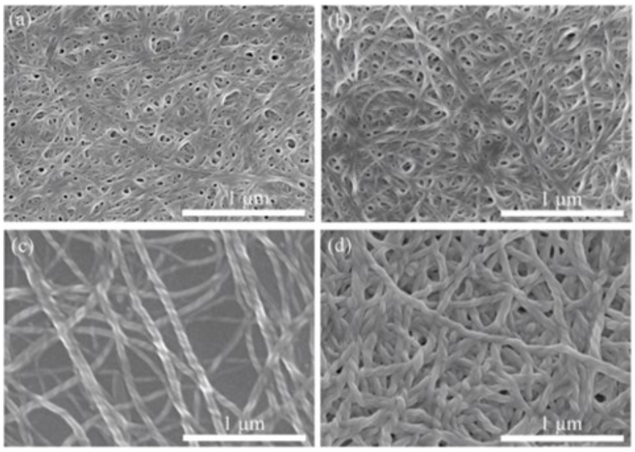

Figure 1.13 SEM images of solvent triggered low molecular weight gels of a sorbitol derived LMWG.[124] Scale bars = 1 µm. Reprinted (adapted) with permission from *Langmuir,* 2014, 30, 44, 13422–13429. Copyright 2014, American Chemical Society.

Cryogenic transmission electron microscopy (Cryo-TEM) has been proposed as an alternative to SEM.[125] Here the aqueous liquid component within samples is vitrified by plunge freezing samples in a liquid cryogen.[126] Samples preparation of this manner should prevent network artefacts from ice crystal formation.[127] This would provide a more accurate representation of the fibrous gelator networks present within the native gels. Recently, this technique was used to great effect in tandem with neutron scattering to elucidate the gelator packing and thus fibre composition for a naphthalene dipeptide LMWG.[128] However, Cryo-TEM is typically limited to samples prepared as thin films.[126] This spatial confinement in itself may alter the gelator network within, especially within low molecular weight gels.[110, 114]

Environmental SEM (ESEM)[129] and more recent iterations as Atmospheric SEM (ASEM)[130, 131] or Air SEM[132] may solve these issues.[133] Within these techniques the sample is exposed to weaker vacuum or atmospheric pressure, so gels could remain hydrated during imaging. This would bridge the disconnect that currently exists between imaging techniques available to characterise gel microstructures. SEM provides significantly higher resolution but incurs drying effects, whilst confocal microscopy can image gels in their native hydrated environment, but only at lower magnifications.

1.5.3 Confocal microscopy

More recently, confocal fluorescence microscopy has become increasingly popular in the visualisation of microstructures within low molecular weight gels (Figure 1.14).[116, 134-137] Through the incorporation of an appropriate fluorescent dye, this technique allows for the observation of underlying gel networks in their native hydrated state providing a key advantage over the electron microscopies.[115] This is usually paired with a trade-off in resolution as standard confocal microscopy techniques are restricted to much lower magnifications due to the diffraction limit.[138, 139] More recently, this has been overcome with greater widespread access to super resolution microscopy techniques.[140, 141] These systems do carry their own drawbacks with respect to sample preparation and compatibility as well as acquisition times being far longer.[141]

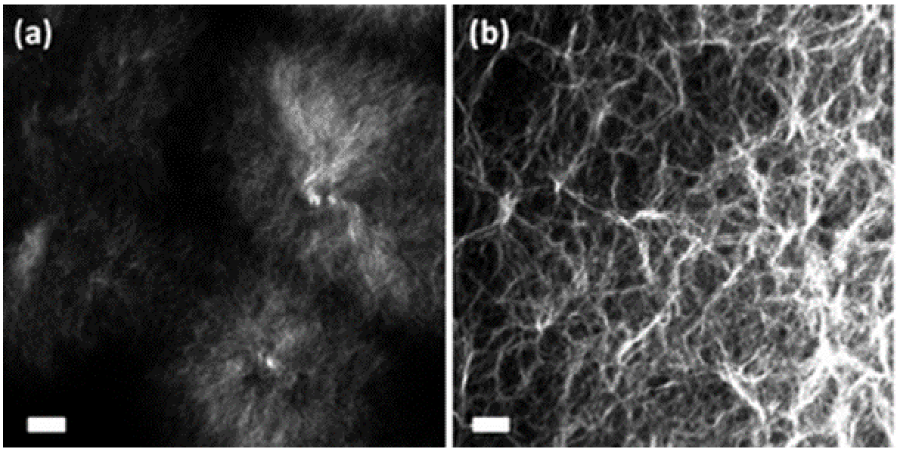

Figure 1.14 Example confocal images of different gelator networks within solvent triggered FmocLG low molecular weight gels formed at a) 10 % and b) 30% DMSO in water. Scale bars = 10 µm. Reproduced with permission from ref.[41] with permission from the Royal Society of Chemistry.

The choice of a suitable dye for the LMWG system being studied is crucial.[142] The dye molecules need to integrate well into the gelator network for adequate resolution and clear imaging. Too high an affinity for water and the solvent component will be imaged instead, resulting in no detail on the gelator network being achieved. As is a common theme in this field, suitable fluorescent dyes to study low molecular weight gels by confocal microscopy are often discovered by chance, usually by initially screening whichever dyes are readily available or easily accessible. Once a dye is found to work well, this tends to be adopted as the default, promoting consistency but potentially missing out on superior alternatives. Continued screening of additional dyes is therefore beneficial, especially for new systems. For gels of dipeptide LMWGs, this can be aided by taking inspiration from the imaging of protein aggregates in biology,[143, 144] where confocal microscopy has long been a standard technique.[145, 146] Another approach also prevalent in biological fields would be the direct attachment of a fluorophore onto the LMWG molecules.[135, 147, 148] This dismisses concerns as to how well external dyes integrate with or disrupt the gelator network and thus how representative the imaging is of the true native microstructure.[149] It also avoids any potential incompatibility issues or modifications to the dyes fluorescence through interactions with LMWG molecules.[150, 151] However, this also raises the question of whether these modified LMWGs, which are typically bigger and possess a different log P value, self-assemble in the same, or at least similar, manner as their root LMWG molecules. It would therefore be expected that these modifications will themselves influence the network observed. In an ideal system, the native LMWG would inherently incorporate a fluorescent motif that would enable direct imaging of the gelator network via confocal microscopy, without an external dye or chemical modification. This would guarantee a truly accurate representation of the microstructures within. Whilst the Fmoc and Nap capped dipeptide LMWGs described above do in theory possess this capability, with both aromatic groups being natively fluorescent,[54, 57, 152] in reality it is not so straightforward. Gelation can modify the fluorescence profile,[57] or quench emission entirely. There is also a significant practical limitation here in that many commonly accessible confocal microscopes lacking support for imaging in the UV region, largely due to cost.[153] This shortfall may result from reduced compatibility with biological systems which, as the major field of application, limits widespread adoption.

Confocal microscopy also allows for 3D visualisation of gelator fibre microstructure through Z-stacks. Taking a Z-stack involves shifting the focal point into the sample, building up an overall 3D image from sequential 2D slices iteratively penetrating into the sample.[154] However, there are limitations to this if the sample is thick or opaque, as low molecular weight gels can often be.[155] Confocal microscopy has even been shown to enable clear distinction between multiple components of different morphologies within a single system.[137, 148] Using the technique in this way could prove exceedingly useful for applications requiring multi-component low molecular weight gels.

1.5.4 Small angle scattering

Small angle neutron (SANS) and x-ray (SAXS) scattering techniques have become significantly more important in the characterisation of these materials in recent years.[116, 156] These allow the gelator fibre morphology to be probed (Figure 1.15). Like confocal microscopy, these can be carried out on gels in-situ, but necessitate samples be formed in very thin glass capillaries, which is expected to affect the network present within some LMWG systems.[110, 114] SANS additionally requires that samples be formed with deuterated solvent, which has the potential to subtly alter materials.[157]

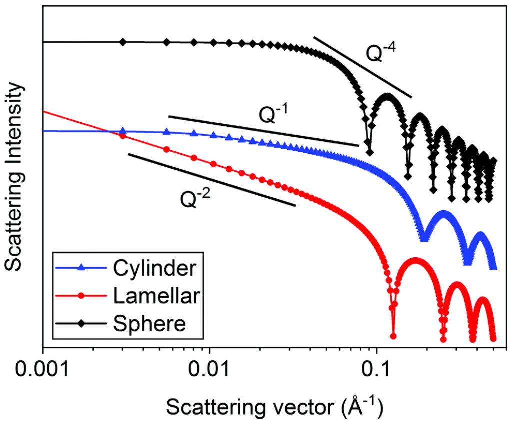

Figure 1.15 Typical scattering patterns of different types of 1D self-assembled structures. Reproduced with permission from ref.[156] with permission from the Royal Society of Chemistry.

1.5.5 Oscillatory rheology

One of the most common, and indeed relevant, methods of characterising the mechanical properties of these classes of viscoelastic materials is through oscillatory rheology.[2] This technique applies oscillatory shear to a material and quantifies its response to this shear stress over time.[158] To at least some extent, many definitions of gels rely on these viscoelastic properties.[159-161] Rheological mechanical viscoelastic properties are broken down into the elastic component and the viscous component.[162] The former relates to a materials resistance to an applied shear stress and is represented by the storage modulus, G′. The latter corresponds to the viscous component, which is a measure of how a material flows under an applied shear stress, represented by the loss modulus, G″. These can be used to assess how a material will behave when subject to high shear-stress in differing applications. Different types of sample can be characterised with the most appropriate of a wide range of different measuring geometries.[163] Many *N*-protected dipeptide gels, and likely other similar systems, are well suited to a cup and vane or suitably sized parallel plate geometry, depending on the specific application they are being considered for (Figure 1.16a and 1.16b).[164-166]

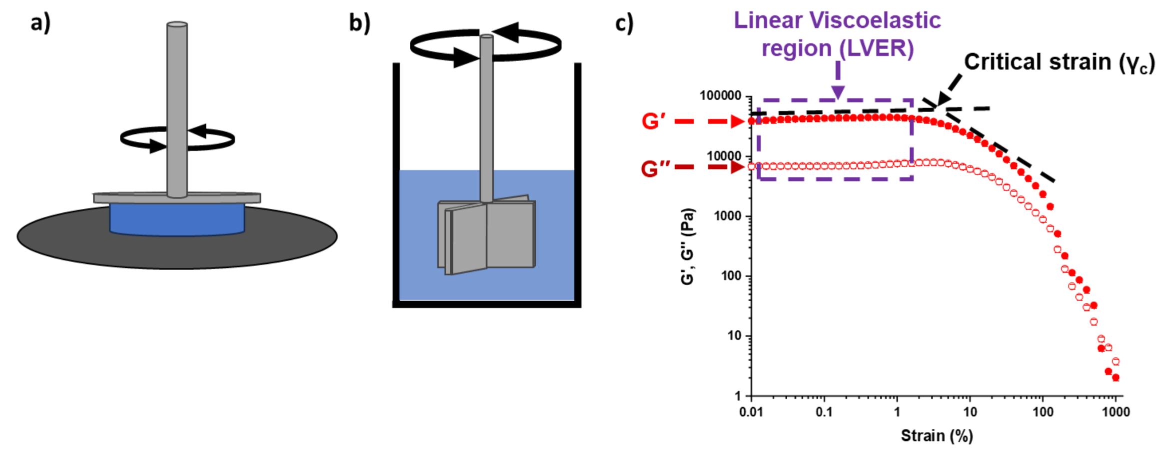

Figure 1.16 Schematic diagram of a a) parallel plate and b) cup and vane rheometer geometry. Gel samples are shown in blue. c) Diagram to illustrate definitions of LVER (purple) and γ_c (black) on an exemplar rheological strain sweep typical of aromatic N-protected dipeptide low molecular weight gels.

From strain sweeps of these gels, we can compare their viscoelastic response through differences in the linear viscoelastic region (LVER) and critical strain (γ_C) values (Figure 1.16c). The LVER corresponds to the region within these plots at which G′ and G″ remain constant under increasing strain up until the gel starts to break and their values deviate significantly. γ_C is the point at which the gelator network has been broken and is derived by the intersection between two tangents drawn from the LVER and post-LVER (Figure 1.16c).

Recently, Fuentes-Caparrós *et al.* demonstrated the ability to distinguish between layers of gels formed at different compositions and the corresponding slight differences in measured mechanical properties.[166] This highlights the sensitivity of this technique and proves it useful for the successful characterisation of heterogenous layered gel samples, a theme becoming increasing relevant for these materials as they are considered for future biomedical applications. However, in some cases there are concerns of this technique being an adequate representation of the shear-stresses experienced during some of these applications, such as gel bioprinting and cell culture,[167, 168] so other alternatives within this field are also of note.

1.5.6 Cavitation rheology

Cavitation rheology, a less widely established micro-rheological technique, is an alternative to bulk oscillatory rheology that utilises the cavitation effect to probe a materials viscoelastic response (Figure 1.17).[169] This is achieved by the formation of a cavitation bubble within a sample.[169-171] This can be achieved via various methods, usually by pumping a pressurised fluid through a hollow needle embedded in the sample, known as needle induced cavitation.[169] Other methods also exist, such as laser or acoustic induced cavitation, but needle based systems are by far the most prevalent.[169] This thesis will only focus on needle induced cavitation. The highest pressure achieved before cavitation takes place and the pressure then starts to fall is deemed the critical pressure, P_c (Figure 1.17c).[170] The critical pressures measured for different materials can be converted into calculated shear moduli and have been shown to correlate with rheological data.[170, 171]

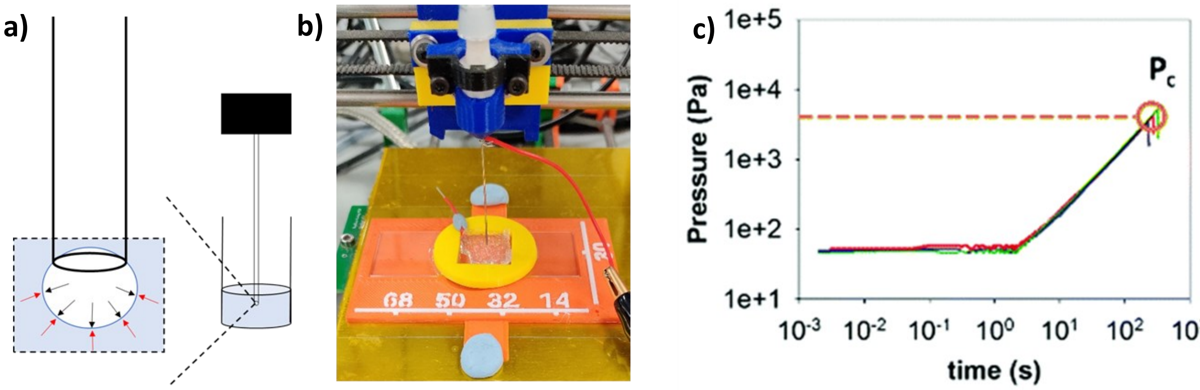

Figure 1.17 (a) Schematic diagram of cavitation rheology. (b) An image of a typical setup within our lab performing cavitation rheology on a 3D printed low molecular weight gel. c) Gel cavitation rheology plot, reproduced with permission from ref.[171] with permission from the Royal Society of Chemistry.

A key advantage of this technique is the sampling; it requires very small minimum sample volumes compared to bulk rheology and does not require specific sample shapes or containers. Differing mechanical properties across a non-uniform sample can be probed as opposed to bulk rheology where only the overall sample response is measured. Currently, the technique suffers from decreased reliability compared to bulk rheology, with the error attached to generated data sets usually being significantly higher than the highly reproducible data possible with oscillatory rheometers.[169] Partially, this stems from a lack of standardised instruments.[169] Whilst procedures are usually well reported, with experimental procedures and equipment extensively described,[170, 171] details are inevitably lost. This is coupled with a lack of standardised procedures for this type of testing, making results generated across research groups hard to compare effectively. The Crosby group continue to develop the theoretical understanding within this field through computer simulated network modelling paired with the diligent testing of well-established polymer systems.[172-176] They also have continued to apply cavitation rheology in combination with other techniques to both diverse and novel chemical and biological systems.[169, 177-179]

The ability to test localised mechanical properties through cavitation rheology may prove exceedingly useful in the future when determining suitability of new low molecular weight gel systems for cell culture, tissue engineering and bioprinting applications. Here, target sample volumes can often be sub-millilitre, making oscillatory rheology challenging. The growth of a cavitation bubble would be expected to be a more relevant rheological system than oscillatory shear when trying to model cell growth in gels towards these biomedical applications (Figure 1.18).[168, 180]

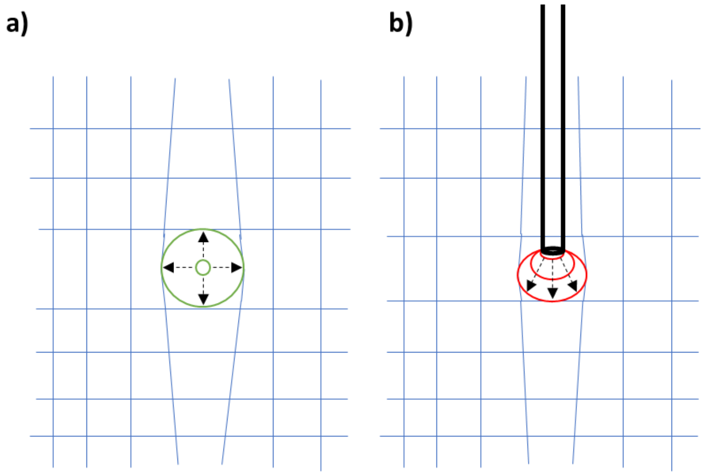

Figure 1.18 Schematic diagram to show how potential cell growth (green) within a gel (a) may be suitably modelled by the growth of a cavitation bubble (red) within a gel during cavitation rheology (b). In both cases, the idealised network is shown by the blue lines.

1.5.7 Nanoindentation

Nano-indentation also provides an alternative means to oscillatory rheology when probing small scale mechanical properties.[181, 182] Here, a micrometre scale probe indents a material with low applied load to generate the Young's modulus.[183] Testing in this way can generate a profile of material strength across a region of a sample or across different samples, allowing for the comparison of different mechanical properties (Figure 1.19).

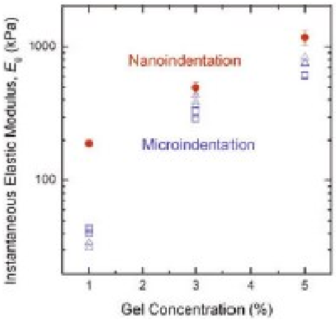

Figure 1.19 Nanoindentation and microindentation derived elastic moduli of 1%, 3%, or 5% agarose gels. Reproduced from ref.[181] with permission from Springer Nature.

Nanoindentation also allows for the testing of smaller samples than possible with bulk rheology. It can be used to some extent in the same capacity as an atomic force microscope (AFM), but with far simpler and quicker sample preparation and data acquisition.[183] The instrument itself is significantly cheaper than an AFM and can be adapted from a standard high power optical microscope. However, it does have disadvantages.[184] Whilst far more widely accessible than an equivalent AFM system, the instrument and specifically the indentation probes themselves are still expensive and fragile. The resolution and overall capability of a nano-indenter is far reduced from an AFM, but for many applications, this is an acceptable trade-off.[183]

1.6 Applications of Low Molecular Weight Gels - Bioprinting

1.6.1 3D printing

Additive manufacturing, more commonly known as 3D printing, is an incredibly diverse manufacturing process, that has vast potential across many industries, such as aerospace and the biomedical field.[185] This technique involves the sequential deposition of layers of material in a well-defined and controlled manner to fabricate pre-designed structures in 3D space.[186] Printed material can range from more traditional substrates, such as plastic, metal and ceramic, through to innovative and technically advanced media, such as cell-laden hydrogels[187]. Advances in printing techniques, the materials used and the printers themselves, as well as their greater availability in recent years has vastly broadened the scope of this field. This has allowed incredibly innovative and intricate designs to be produced even on the most basic of commonly available equipment. We are fast approaching the point that an end-user's imagination and commitment to a project will become a significant limiting factor (Figure 1.20).

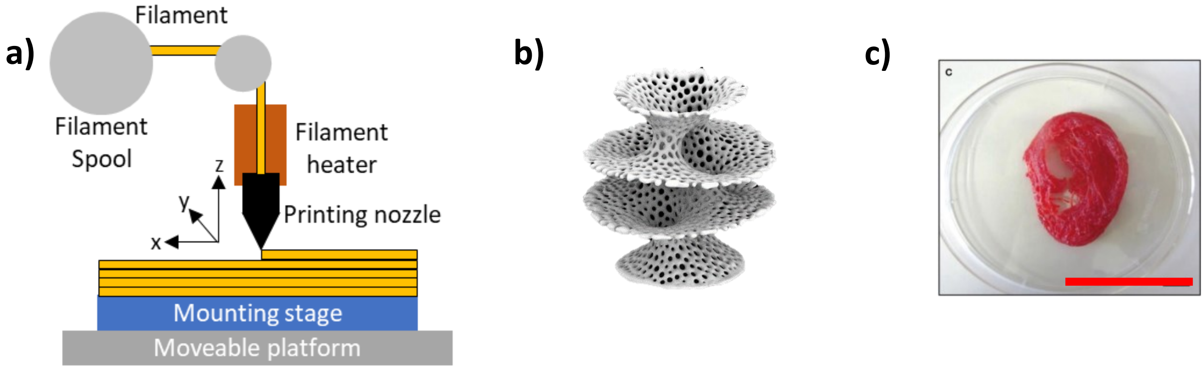

Figure 1.20 A simplified schematic for a typical fusion deposition modelling style 3D printer (a),[188] alongside an example of an intricate 'lattice style' 3D printed model (b)[189] and an artificial ear printed from a short sequence peptide hydrogel in a copolymer support (c),[190] at a clinical scale. Scale bar (red) = 40 mm. Part C is adapted from ref.[190] by Chiesa *et al.*

1.6.2 Bioprinters

Extrusion based bioprinters are by far the most common example amongst researchers within the biomedical fields today.[191] They are low cost and widely accessible, with many groups retrofitting standard extrusion-based printers with custom paste extruders 3D printed with the original printer parts to replace the standard filament extrusion nozzles. Reid *et al.* effectively demonstrated this, successfully converting a standard 3D printer into a bioprinter using in-house fabricated parts and standard lab consumables, enabling the accurate placement of solutions containing cells.[192] In these systems, repairs are cost effective and can be carried out in-house on the fly, as well as allowing for rapid iteration of design to trial new systems or methods. Whilst extrusion based printers achieve lower printing speeds and reduced cell viability, they maintain moderate resolutions and have the advantage of being able to print higher viscosity materials than alternative options, giving them a broader operational range.[193]

These printers use pneumatic pressure,[194] a screw,[195] or a more traditional piston to drive the biomaterial out of a paste extruder that can be programmed to move in the x, y & z planes.[196] Of these, the piston driven systems are by far the most commonly used as they translate to a simple syringe and plunger based set-up, fitted with an appropriate nozzle for extrusion. Biomaterial is then extruded upon compression of the plunger either straight onto a glass plate, termed direct extrusion (Figure 1.21a)., or into a support-bath (Figure 1.21b). The support bath can provide structural support through viscosity or aid post-printing processing.[197] From here on, extrusion-based bioprinting will be the assumed technique, unless otherwise stated.

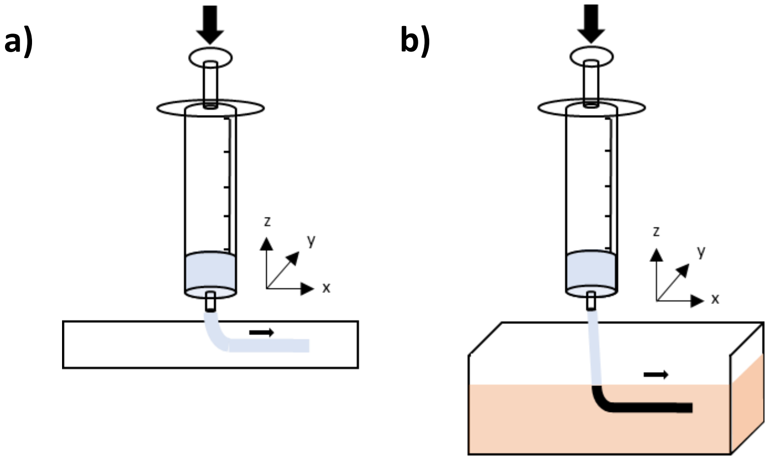

Figure 1.21 Schematic diagrams of extrusion-based 3D bioprinting, with (a) direct extrusion and (b) bath-supported methods shown.

1.6.3 Biomaterials as printing inks

Just as traditional printing technologies rely on ink as their printing media, bioprinters utilise bioinks.[198] These are defined as the combination of biomaterials loaded with desired cell types for 3D printing. Given their delicate biological payload and the intense process by which they are delivered, it follows that there are criteria governing a biomaterials suitability as a bioink.[199]

Key properties for successful bioink candidates suitable for bioprinting include: biocompatibility, thixotropy and shear recovery.[200] Biocompatibility requires that materials and methods of manufacture are non-toxic and promote cell viability. These qualities allow the bioink to effectively host viable cells loaded within, with the possibility of sterile preparation methods highly desirable. Thixotropy is a time-dependent shear thinning property; a typically viscous thixotropic material will flow under shear stress and upon removal of this stress, the material will return to its viscous state over time.[201] This behaviour stems from shear recovery, whereby a material is able to recover its viscoelastic mechanical properties through facilitating mechanisms after being subject to high shear stress. The former two features are vital for ensuring printability of a prospective bioink.[198]

1.6.4 Low molecular weight gels for 3D printing

In recent attempts to produce new bioinks, efforts have turned towards low molecular weight hydrogels.[193] Being responsive to external stimuli coupled with their typically modular tuneable nature enables them to be directly tailored to purpose for 3D printing, with properties selected by choosing appropriate molecular building blocks.[118] Chalard *et al.* have demonstrated the successful printing of a small amphiphilic molecule, *N*-heptyl-ᴅ-galactonamide (GalC7).[202] This LMWG amphiphile has been previously demonstrated by this group to be formed via a straightforward one stage synthesis, whilst also forming hydrogels via thermal cycling.[96] These gels are biocompatible and shown to promote the viability of stem cells.[96] To print this LMWG, a gelator solution was extruded via syringe and needle into a support bath of DMSO and water. This dual solvent system provides an appropriate solvent-switch trigger to encourage rapid gelation of the extruded solution, depositing a gel filament (Figure 1.22).[202]

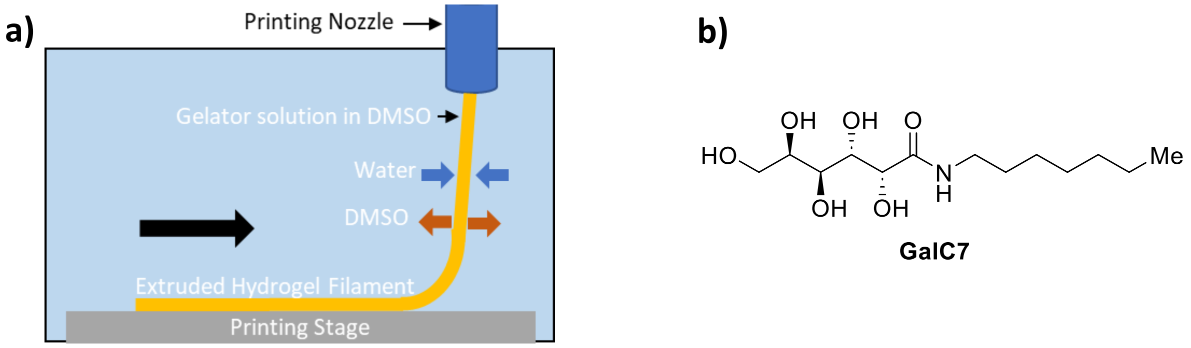

Figure 1.22 (a) Overview schematic diagram of bath-facilitated extrusion 3D printing of solvent-switch *N*-heptyl-ᴅ-galactonamide (GalC7) gel filaments, with GalC7 chemical structure shown (b).[202] Figure reproduced from Additive Manufacturing, Volume 33, Chalard *et al.*, "3D printing of a biocompatible low molecular weight supramolecular hydrogel by dimethylsulfoxide water solvent exchange",[202] Article 101162, pages 1-7, Copyright (2020), with permission from Elsevier.

This solvent switch based extrusion method was refined to allow for good adhesion to a glass printing stage by optimising the system to encourage gelation of the extruded material just as it was reaching the printing bed, which enabled consistent and precise 3D printed structures. The system clearly displays inherent tuneability within the printing process to reach desired bioink mechanical properties, without the need for chemical modification. However, gels must be printed within a support bath. Biocompatibility persists despite the introduction of DMSO, as this can be subsequently washed out. This process may impact the overall effectiveness, with more direct printing being desirable.

Working towards this, Jian *et al.* successfully printed LMWG based bioinks that did not require a support bath.[203] Here the careful selection of two *N*-functionalised dipeptide LMWGs FmocYD and FmocYK (Figure 1.23a & 1.23b) enabled the co-printing of these two gels to form self-supporting structures. This relies upon the interactions between two oppositely charged functional groups within the amino side chains of the different LMWGs. These two different gel layers are used to provide a more robust overall sample that possesses higher mechanical properties (Figure 1.23c). These were shown to promote cell viability, demonstrating good biocompatibility.

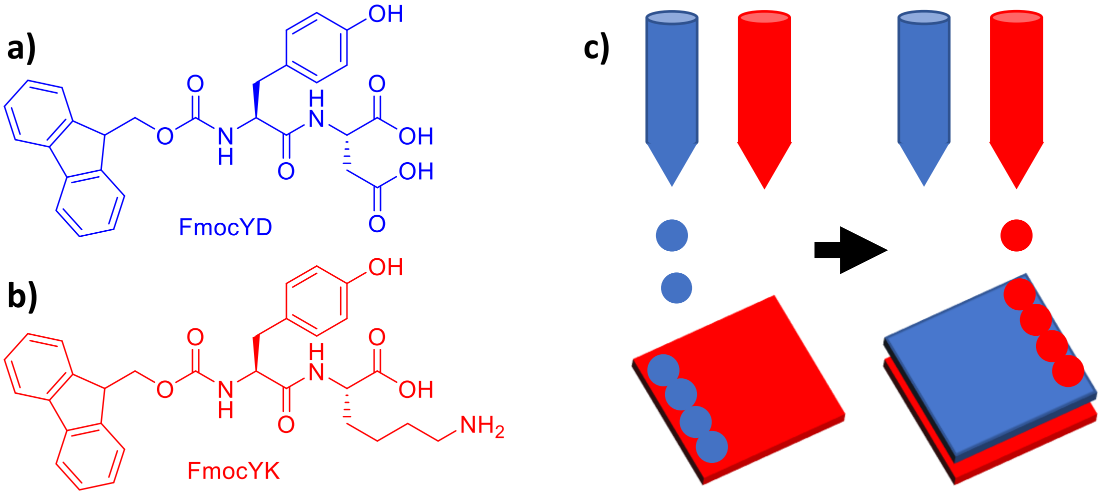

Figure 1.23 LMWGs (a) FmocYD & (b) FmocYK used to form alternating layers of printed gel (c).[203]

Whilst this system does make a step towards direct 3D printing as a potential bioink, and clearly demonstrates inherent tuneability, it does have its limits. It used inkjet bioprinting, a typically less favourable technique that can have limitations as to the complexity of structures that are printable due to inks spreading out or migrating post-printing. The layers take time to gel, and it is unclear whether cells could be loaded before printing and continue to remain viable after the process.

Finally, Nolan *et al.* have successfully demonstrated direct extrusion based bioprinting of dipeptide low molecular weight gels.[204] Their approach utilised the *N*-functionalised dipeptide, Fmoc-diphenylalanine (FmocFF), but studied its direct extrusion as a single component bioink. This negates the need for a support bath or other post-printing modification, in contrast to the above works.[202, 203] FmocFF gels were shown to be consistently extrudable with good precision from pre-formed gels within printing cartridges. Effective recovery of the gels mechanical properties was seen after the high shear stress imparted throughout the printing process. Residual effects of the extrusion process on both the mechanical properties of the gels as well as their underlying microstructure were investigated. Multilayer gels containing different dyes were also produced. Their work explicitly details the optimisation of the extrusion, and thus printing, process for this specific system, providing a generalised set of guidelines for developing this class of LMWG based gel and a readily available printer to do so. Subsequent work by Fuentes-Caparrós *et al.* was later shown to develop upon this initial system, by expanding to multi-layered samples printed from gels of differing LMWG concentration.[166]

Whilst this system is in good agreement with the necessary mechanical requirements of bioinks, biocompatibility issues are of concern. The system would need to be subsequently assessed for cell viability as whilst the gelator itself has been shown to be biocompatible,[205] the relatively high DMSO content is well above the commonly accepted cytotoxic level of >0.1 %. This may be removed by subsequent washing as outlined previously by Chalard *et al*.[202]

Nolan *et al.*'s work presents a key prevailing issue within gel 3D printing as a whole; the usually serendipitous, trial and error driven discovery of effective examples of 3D printable low molecular weight gels.[204] It is clear that further work needs to be carried out into examining why certain gels are suitable for 3D printing whilst others are not. This would enable the creation of a set of guidelines that promote the informed and rationalised prediction of effectively printable candidate gels.

1.7 Aim of the present study

As highlighted, low molecular weight gels produced from *N*-protected dipeptide LMWGs have great potential for innovative applications across a wide range of fields. Yet many aspects of these materials are still poorly understood and at times not even considered. This Thesis aims to further both the understanding and application of these gels.

Chapter 2 shows how the gels of two different dipeptide LMWGs can be 3D printed in combination with one another to produce multi-layered printed gel samples with heterogeneous mechanical properties. These properties can be modified by utilising different combinations of printed gel layers. The interface between printed gels was then explored. This builds towards applying these materials in a biomedical setting.

Chapter 3 demonstrates the effect of imposing spatial constraints on dipeptide low molecular weight gels formed by different gelation triggers and how the responses of these differ.

Finally, Chapter 4 explores potential network differences at the surface of these gels and shows no correlation between observed network differences and measured mechanical properties.

Chapters 3 and 4 explore two aspects of this class of material that, to the best of our knowledge, have not previously been considered and aim to further the existing understanding within this field.

1.8 References

1. T. Tanaka, *Sci. Am.*, 1981, **244**, 124-138.
2. C. J. Rueb and C. F. Zukoski, *J. Rheol.*, 1997, **41**, 197-218.
3. A. R. Hirst, B. Escuder, J. F. Miravet and D. K. Smith, *Angew. Chem. Int. Ed.*, 2008, **47**, 8002-8018.
4. L. A. Estroff and A. D. Hamilton, *Chem. Rev.*, 2004, **104**, 1201-1218.
5. P. Terech and R. G. Weiss, *Chem. Rev.*, 1997, **97**, 3133-3160.
6. N. Chirani, L. H. Yahia, L. Gritsch, F. L. Motta and S. Chirani, *J. Biomed. Sci.*, 2015, **4**, 1-23.
7. A. G. Marangoni, in *Edible Oleogels*, ed. A. G. Marangoni and N. Garti, AOCS Press, Urbana, 1st edn, 2011, ch. 1, pp. 1-17.
8. A. Keller, *Faraday Discuss*., 1995, **101**, 1-49.
9. Q. Yu and E. J. Amis, Makromol. Chem., *Macromol. Symp*., 1993, **76**, 193-200.
10. D. K. Smith, *Soft Matter*, 2024, **20**, 10-70.
11. D. B. Amabilino, D. K. Smith and J. W. Steed, *Chem. Soc. Rev.*, 2017, **46**, 2404-2420.
12. R. G. Weiss and P. Terech, *Molecular Gels*, Springer, Dordrecht, 2016.
13. S. Panja and D. J. Adams, *Chem. Soc. Rev.*, 2021, **50**, 5165-5200.
14. Z. Sun, Q. Huang, T. He, Z. Li, Y. Zhang and L. Yi, *ChemPhysChem*, 2014, **15**, 2421-2430.
15. X. Yan, F. Wang, B. Zheng and F. Huang, *Chem. Soc. Rev.*, 2012, **41**, 6042-6065.
16. P. R. A. Chivers and D. K. Smith, *Nat. Rev. Mater*., 2019, **4**, 463-478.
17. A. Mahler, M. Reches, M. Rechter, S. Cohen and E. Gazit, *Adv. Mater*., 2006, **18**, 1365-1370.
18. J. Raeburn, G. Pont, L. Chen, Y. Cesbron, R. Lévy and D. J. Adams, *Soft Matter*, 2012, **8**, 1168-1174.
19. N. A. Dudukovic and C. F. Zukoski, *Langmuir*, 2014, **30**, 4493-4500.
20. B. O. Okesola, V. M. P. Vieira, D. J. Cornwell, N. K. Whitelaw and D. K. Smith, *Soft Matter*, 2015, **11**, 4768-4787.
21. D. J. Adams, M. F. Butler, W. J. Frith, M. Kirkland, L. Mullen and P. Sanderson, *Soft Matter*, 2009, **5**, 1856-1862.
22. J. Raeburn, T. O. McDonald and D. J. Adams, *Chem. Comm.*, 2012, **48**, 9355-9357.
23. K. McAulay, P. A. Ucha, H. Wang, A. M. Fuentes-Caparrós, L. Thomson, O. Maklad, N. Khunti, N. Cowieson, M. Wallace, H. Cui, R. J. Poole, A. Seddon and D. J. Adams, *Chem. Comm.*, 2020, **56**, 4094-4097.
24. A. Z. Cardoso, L. L. E. Mears, B. N. Cattoz, P. C. Griffiths, R. Schweins and D. J. Adams, *Soft Matter*, 2016, **12**, 3612-3621.
25. D. J. Abdallah and R. G. Weiss, *Adv. Mater*., 2000, **12**, 1237-1247.
26. J. H. Van Esch and B. L. Feringa, *Angew. Chem. Int. Ed.*, 2000, **39**, 2263-2266.
27. J. Raeburn, A. Z. Cardoso and D. J. Adams, *Chem. Soc. Rev.*, 2013, **42**, 5143.
28. L. Chen, T. O. McDonald and D. J. Adams, *RSC Adv*., 2013, **3**, 8714-8720.
29. J. Smilek, S. Jarábková, T. Velcer and M. Pekař, *Polymers*, 2019, **11**, 927.
30. E. R. Draper and D. J. Adams, *Langmuir*, 2019, **35**, 6506-6521.
31. M. J. Meunier, *Ann. Chim. Phys*., 1891, **22**, 214-432.
32. J. H. van Esch, *Langmuir*, 2009, **25**, 8392-8394.
33. R. Zsigmondy and W. Bachmann, *Z. Chem. Ind. Kolloide*, 1912, **11**, 145-157.
34. J. Poppe, *Thickening and Gelling Agents for Food*, Springer New York, NY, 1997.

35. R. G. Armisen, in *Handbook of Hydrocolloids*, ed. G. O. Phillips and P. A. Williams, Woodhead Publishing, Cambridge, 2nd edn., 2009, ch. 4, pp. 82-105.
36. K. Hanabusa, M. Yamada, M. Kimura and H. Shirai, *Angew. Chem., Int. Ed. Engl.*, 1996, **35**, 1949-1951.
37. E. R. Draper and D. J. Adams, *Chem*, 2017, **3**, 390-410.
38. K. Hanabusa and M. Suzuki, *Polym. J.*, 2014, **46**, 776-782.
39. M. De Loos, B. L. Feringa and J. H. Van Esch, *Eur. J. Org. Chem.*, 2005, **17**, 3615-3631.
40. H. Goyal, S. Pachisia and R. Gupta, *Cryst. Growth Des.*, 2020, **20**, 6117-6128.
41. L. Chen, J. Raeburn, S. Sutton, D. G. Spiller, J. Williams, J. S. Sharp, P. C. Griffiths, R. K. Heenan, S. M. King, A. Paul, S. Furzeland, D. Atkins and D. J. Adams, *Soft Matter*, 2011, **7**, 9721-9727.
42. H. Wang, Z. Yang and D. J. Adams, *Mater. Today*, 2012, **15**, 500-507.
43. M. D. Segarra-Maset, V. J. Nebot, J. F. Miravet and B. Escuder, *Chem. Soc. Rev.*, 2013, **42**, 7086-7098.
44. X. Yang, G. Zhang and D. Zhang, *J. Mater. Chem.*, 2012, **22**, 38-50.
45. L. Xu, M. Zhao, Y. Yang, Y. Liang, C. Sun, W. Gao, S. Li, B. He and Y. Pu, *J. Mater. Chem. B*, 2017, **5**, 9157-9164.
46. R. V. Ulijn and A. M. Smith, *Chem. Soc. Rev.*, 2008, **37**, 664-675.
47. Y. Zhang, H. Gu, Z. Yang and B. Xu, *J. Am. Chem. Soc.*, 2003, **125**, 13680-13681.
48. R. Vegners, I. Shestakova, I. Kalvinsh, R. M. Ezzell and P. A. Janmey, *J. Pept. Sci.*, 1995, **1**, 371-378.
49. S. Toledano, R. J. Williams, V. Jayawarna and R. V. Ulijn, *J. Am. Chem. Soc.*, 2006, **128**, 1070-1071.
50. Z. Yang, H. Gu, Y. Zhang, L. Wang and B. Xu, *Chem. Comm.*, 2004, **2**, 208-209.
51. Z. Yang, G. Liang and B. Xu, *Chem. Comm.*, 2006, **7**, 738-740.
52. L. Li, L. Xie, R. Zheng and R. Sun, *Front. Chem.*, 2021, **9**, 739791.
53. C. Diaferia, E. Rosa, E. Gallo, G. Morelli and A. Accardo, *Chem. Eur. J.*, 2023, **29**, e2023006.
54. A. D. Martin and P. Thordarson, *J. Mater. Chem*. B, 2020, **8**, 863-877.
55. Z. Yang, G. Liang, M. Ma, Y. Gao and B. Xu, *J. Mater. Chem.*, 2007, **17**, 850-854.
56. X. Mu, K. M. Eckes, M. M. Nguyen, L. J. Suggs and P. Ren, *Biomacromolecules*, 2012, **13**, 3562-3571.
57. C. Tang, R. V. Ulijn and A. Saiani, *Eur. Phys. J. E*, 2013, **36**, 111.
58. K. Karmakar and S. Haldar, *RSC Adv.*, 2016, **6**, 71025-71045.
59. D. J. Adams, L. M. Mullen, M. Berta, L. Chen and W. J. Frith, *Soft Matter*, 2010, **6**, 1971-1980.
60. K. McAulay, B. Dietrich, H. Su, M. T. Scott, S. Rogers, Y. K. Al-Hilaly, H. Cui, L. C. Serpell, Annela, E. R. Draper and D. J. Adams, *Chem. Sci.*, 2019, **10**, 7801-7806.
61. M. Qin, Y. Zhang, C. Xing, L. Yang, C. Zhao, X. Dou and C. Feng, *Chem. Eur. J.*, 2021, **27**, 3119-3129.
62. S. Kuila, A. K. Singh, A. Shrivastava, S. Dey, T. Singha, L. Roy, B. Satpati and J. Nanda, *J. Phys. Chem. B*, 2023, **127**, 4808-4819.
63. Q. Guan, K. McAulay, T. Xu, S. E. Rogers, C. Edwards-Gayle, R. Schweins, H. Cui, A. M. Seddon and D. J. Adams, *Biomacromolecules*, 2023, **24**, 2847-2855.
64. H. Arakawa, K. Takeda, S. L. Higashi, A. Shibata, Y. Kitamura and M. Ikeda, *Polym. J.*, 2020, **52**, 923-930.
65. B. L. Abraham, W. Liyanage and B. L. Nilsson, *Langmuir*, 2019, **35**, 14939-14948.
66. I. W. Hamley, *ACS Appl. Bio Mater.*, 2023, **6**, 384-409.

67. K. L. Morris, L. Chen, A. Rodger, D. J. Adams and L. C. Serpell, *Soft Matter*, 2015, **11**, 1174-1181.
68. S. Awhida, E. R. Draper, T. O. McDonald and D. J. Adams, *J. Colloid Interface Sci.*, 2015, **455**, 24-31.
69. P. G. Argudo, R. Contreras-Montoya, L. Álvarez De Cienfuegos, M. T. Martín-Romero, L. Camacho and J. J. Giner-Casares, *J. Phys. Chem. B*, 2019, **123**, 3721-3730.
70. C. F. Brayton, *Cornell Vet.*, 1986, **76**, 61-90.
71. M. Awan, I. Buriak, R. Fleck, B. Fuller, A. Goltsev, J. Kerby, M. Lowdell, P. Mericka, A. Petrenko, Y. Petrenko, O. Rogulska, A. Stolzing and G. N. Stacey, *Regen. Med.*, 2020, **15**, 1463-1491.
72. J. Galvao, B. Davis, M. Tilley, E. Normando, M. R. Duchen and M. F. Cordeiro, *FASEB J.*, 2014, **28**, 1317-1330.
73. C. Diaferia, G. Morelli and A. Accardo, *J. Mater. Chem. B*, 2019, **7**, 5142-5155.
74. Y. Li and X. Liu, *Chem. Comm.*, 2014, **50**, 3155-3158.
75. L. A. Carpino, *Acc. Chem. Res.*, 1987, **20**, 401-407.
76. L. Chen, K. Morris, A. Laybourn, D. Elias, M. R. Hicks, A. Rodger, L. Serpell and D. J. Adams, *Langmuir*, 2010, **26**, 5232-5242.
77. V. Jayawarna, M. Ali, T. A. Jowitt, A. F. Miller, A. Saiani, J. E. Gough and R. V. Ulijn, *Adv. Mater.*, 2006, **18**, 611-614.
78. S. Panja and D. J. Adams, *Chem. Comm.*, 2019, **55**, 47-50.
79. J. Raeburn, B. Alston, J. Kroeger, T. O. McDonald, J. R. Howse, P. J. Cameron and D. J. Adams, *Mater. Horiz.*, 2014, **1**, 241-246.
80. S. Panja, A. M. Fuentes-Caparrós, E. R. Cross, L. Cavalcanti and D. J. Adams, *Chem. Mater.*, 2020, **32**, 5264-5271.
81. E. R. Draper, E. G. B. Eden, T. O. McDonald and D. J. Adams, *Nat. Chem.*, 2015, **7**, 848-852.
82. R. E. Ginesi, N. R. Murray, R. M. Dalgliesh, J. Doutch and E. R. Draper, *Chem. Eur. J.*, 2023, **29**, e202301042.
83. J. L. Andrews, E. Pearson, D. S. Yufit, J. W. Steed and K. Edkins, *Cryst. Growth Des.*, 2018, **18**, 7690-7700.
84. J. Raeburn, C. Mendoza-Cuenca, B. N. Cattoz, M. A. Little, A. E. Terry, A. Z. Cardoso, P. C. Griffiths and D. J. Adams, *Soft Matter*, 2015, **11**, 927-935.
85. C. Yuan, A. Levin, W. Chen, R. Xing, Q. Zou, T. W. Herling, P. K. Challa, T. P. J. Knowles and X. Yan, *Angew. Chem. Int. Ed.*, 2019, **58**, 18116-18123.
86. P. Taylor, *Colloids Surf. A: Physicochem. Eng. Asp.*, 1995, **99**, 175-185.
87. S. Roldán-Vargas, F. Smallenburg, W. Kob and F. Sciortino, *Sci. Rep.*, 2013, **3**, 2451.
88. Z. Bashir, *J. Polym. Sci. B: Polym Phys.*, 1992, **30**, 1299-1304.
89. J. S. Winter, *et al.*, *Defence Technical Information Center*, AD-A008 396, 1975, 157.
90. I. Tomka, J. Bohonek, A. Spühler and M. Ribeaud, *J. Photogr. Sci.*, 1975, **23**, 97-103.
91. M. R. Letherby and D. A. Young, *J. Chem. Soc., Faraday Trans. 1*, 1981, **77**, 1953-1966.
92. P. Serwer, *Electrophoresis*, 1983, **4**, 375-382.
93. C. Colquhoun, E. R. Draper, R. Schweins, M. Marcello, D. Vadukul, L. C. Serpell and D. J. Adams, *Soft Matter*, 2017, **13**, 1914-1919.
94. A. Rajbhandary, W. W. Brennessel and B. L. Nilsson, *Crys. Growth Des.*, 2018, **18**, 623-632.
95. K. A. Houton, K. L. Morris, L. Chen, M. Schmidtmann, J. T. A. Jones, L. C. Serpell, G. O. Lloyd and D. J. Adams, *Langmuir*, 2012, **28**, 9797-9806.
96. A. Chalard, L. Vaysse, P. Joseph, L. Malaquin, S. Souleille, B. Lonetti, J.-C. Sol, I. Loubinoux and J. Fitremann, *ACS Appl. Mater. Interfaces*, 2018, **10**, 17004-17017.

97. D. Bordignon, B. Lonetti, C. Coudret, P. Roblin, P. Joseph, L. Malaquin, A. Chalard and J. Fitremann, *J. Colloid Interface Sci.*, 2021, **603**, 333-343.
98. J. A. N. Zasadzinski, A. Chu and R. K. Prud'Homme, *Macromolecules*, 1986, 19, 2960-2964.
99. C. G. Shull, P. B. Elkin and L. C. Roess, *J. Am. Chem. Soc.*, 1948, **70**, 1410-1414.
100. T. Rossow and S. Seiffert, *Polym. Chem*., 2014, **5**, 3018-3029.
101. K. McAulay, H. Wang, A. M. Fuentes-Caparrós, L. Thomson, N. Khunti, N. Cowieson, H. Cui, A. Seddon and D. J. Adams, *Langmuir*, 2020, **36**, 8626-8631.
102. E. R. Draper, M. Wallace, R. Schweins, R. J. Poole and D. J. Adams, *Langmuir*, 2017, **33**, 2387-2395.
103. K. McAulay, L. Thomson, L. Porcar, R. Schweins, N. Mahmoudi, D. J. Adams and E. R. Draper, *Organic Materials*, 2020, **2**, 108-115.
104. D. K. Kumar and J. W. Steed, *Chem. Soc. Rev*., 2014, **43**, 2080-2088.
105. R. D. Chakravarthy, I. Sahroni, C. W. Wang, M. Mohammed and H. C. Lin, *ACS Nano*, 2023, **17**, 11805-11816.
106. P. Zhou, R. Xing, Q. Li, J. Li, C. Yuan and X. Yan, *Matter*, 2023, **6**, 1945-1963.
107. J. W. P. Schmelzer, in *Molecular Gels*, ed. R. G. Weiss and P. Terech, Springer Netherlands, Dordrecht, 1st edn, 2006, ch. 4, pp. 131-160.
108. X. Huang, S. R. Raghavan, P. Terech and R. G. Weiss, *J. Am. Chem. Soc.*, 2006, **128**, 15341-15352.
109. X. Huang, P. Terech, S. R. Raghavan and R. G. Weiss, *J. Am. Chem. Soc.,* 2005, **127**, 4336-4344.
110. M. J. S. Hill, A. M. Fuentes-Caparrós and D. J. Adams, *Biomacromolecules*, 2023, **24**, 4253-4262.
111. F. Tanaka, in *Molecular Gels*, ed. R. G. Weiss and P. Terech, Springer Netherlands, Dordrecht, 1st edn, 2006, ch. 1, pp. 17-77.
112. B. Yuan, X. Y. Liu, J. L. Li and H. Y. Xu, *Soft Matter*, 2011, **7**, 1708-1713.
113. K. Zhang, K. Xue and X. J. Loh, *Gels*, 2021, **7**, 77.
114. W. Chen, Y. Yang, C. H. Lee and A. Q. Shen, *Langmuir*, 2008, **24**, 10432-10436.
115. E. R. Draper and D. J. Adams, *Chem. Soc. Rev.*, 2018, **47**, 3395-3405.
116. G. Yu, X. Yan, C. Han and F. Huang, *Chem. Soc. Rev.*, 2013, **42**, 6697-6722.
117. V. J. Nebot and D. K. Smith, in *Functional Molecular Gels*, ed. B. Escuder and J. F. Miravet, The Royal Society of Chemistry, London, 2014, ch. 2, pp. 30-66.
118. T. Jungst, W. Smolan, K. Schacht, T. Scheibel and J. Groll, *Chem. Rev.*, 2016, **116**, 1496-1539.
119. C. Colquhoun, E. R. Draper, E. G. B. Eden, B. N. Cattoz, K. L. Morris, L. Chen, T. O. McDonald, A. E. Terry, P. C. Griffiths, L. C. Serpell and D. J. Adams, *Nanoscale*, 2014, **6**, 13719-13725.
120. P. Echlin, *Handbook of Sample Preparation for Scanning Electron Microscopy and X-Ray Microanalysis*, Springer US, NY, 2011.
121. F. D. Martinez-Garcia, T. Fischer, A. Hayn, C. T. Mierke, J. K. Burgess and M. C. Harmsen, *Gels*, 2022, **8**, 535.
122. J. W. Steed, *Chem. Comm*., 2011, **47**, 1379-1383.
123. L. L. E. Mears, E. R. Draper, A. M. Castilla, H. Su, Zhuola, B. Dietrich, M. C. Nolan, G. N. Smith, J. Doutch, S. Rogers, R. Akhtar, H. Cui and D. J. Adams, *Biomacromolecules*, 2017, **18**, 3531-3540.
124. J. Li, K. Fan, X. Guan, Y. Yu and J. Song, *Langmuir*, 2014, **30**, 13422-13429.
125. C. Marmorat, A. Arinstein, N. Koifman, Y. Talmon, E. Zussman and M. Rafailovich, *Sci. Rep.*, 2016, **6**, 25495.
126. G. Weissenberger, R. J. M. Henderikx and P. J. Peters, *Nat. Methods*, 2021, **18**, 463-471.
127. C. Efthymiou, M. A. K. Williams and K. M. McGrath, *Food Hydrocoll*., 2017, **73**, 203-212.

128. R. R. Sonani, S. Bianco, B. Dietrich, J. Doutch, E. R. Draper, D. J. Adams and E. H. *Egelman, Cell Rep. Phys. Sci.,* 2024, **5,** 101812.
129. G. D. Danilatos, *Scanning*, 1980, **3**, 215-217.
130. H. Nishiyama, M. Koizumi, K. Ogawa, S. Kitamura, Y. Konyuba, Y. Watanabe, N. Ohbayashi, M. Fukuda, M. Suga and C. Sato, *Ultramicroscopy*, 2014, **147**, 86-97.
131. Y. Ominami, in *Compendium of Surface and Interface Analysis*, ed. The Surface Science Society of Japan, Springer Singapore, Singapore, 2018, ch. 28, pp. 165-169.
132. D. A. Muller, K. X. Nguyen, Y. Han, B. D. A. Levin and M. E. Holtz, *Microsc. Microanal.*, 2018, **24**, 342-343.
133. Z. Kaberova, E. Karpushkin, M. Nevoralová, M. Vetrík, M. Šlouf and M. Dušková-Smrčková, *Polymers*, 2020, **12**, 578.
134. A. D. Dinsmore, E. R. Weeks, V. Prasad, A. C. Levitt and D. A. Weitz, *Appl. Opt.*, 2001, **40**, 4152-4159.
135. J. Zhong, T. Zhao and M. Liu, *NPG Asia Mater.*, 2022, **14**, 38.
136. B. R. Denzer, R. J. Kulchar, R. B. Huang and J. Patterson, *Gels*, 2021, **7**, 158.
137. R. Kubota, K. Nakamura, S. Torigoe and I. Hamachi, *ChemistryOpen*, 2020, **9**, 67-79.
138. T. Wilson, *Confocal Microscopy*, Academic Press, Cambridge, MA, 1990.
139. J. B. Pawley, in *Fundamental Limits in Confocal Microscopy*, ed. J. B. Pawley, Springer US, Boston, 3rd edn, 2006, ch. 2, pp. 20-42.
140. K. Prakash, B. Diederich, R. Heintzmann and L. Schermelleh, Philos. Trans. R. Soc. A, 2022, **380**, 20210110.
141. E. Fuentes, K. Boháčová, A. M. Fuentes-Caparrós, R. Schweins, E. R. Draper, D. J. Adams, S. Pujals and L. Albertazzi, *Chem. Eur. J.*, 2020, **26**, 9869-9873.
142. G. Bkaily, D. Jacques and P. Pothier, in *Methods in Enzymology*, ed. P. Michael Conn, Elsevier, Amsterdam, 1999, vol. 307, ch. 8, pp. 119-135.
143. S. Freire, M. H. De Araujo, W. Al-Soufi and M. Novo, Dy*es Pigm.*, 2014, **110**, 97-105.
144. S. Marchesan, K. E. Styan, C. D. Easton, L. Waddington and A. V. Vargiu, *J. Mater. Chem*. B, 2015, **3**, 8123-8132.
145. T. Suzuki, K. Fujikura, T. Higashiyama and K. Takata, *J. Histochem. Cytochem.*, 1997, **45**, 49-53.
146. B. Demeule, R. Gurny and T. Arvinte, *Int. J. Pharm.*, 2007, **329**, 37-45.
147. S. E. Cowan, E. Gilbert, A. Khlebnikov and J. D. Keasling, *Appl. Environ. Microbiol.*, 2000, **66**, 413-418.
148. S. Onogi, H. Shigemitsu, T. Yoshii, T. Tanida, M. Ikeda, R. Kubota and I. Hamachi, *Nat. Chem.*, 2016, **8**, 743-752.
149. T. N. Tikhonova, N. N. Rovnyagina, Z. A. Arnon, B. P. Yakimov, Y. M. Efremov, D. Cohen-Gerassi, M. Halperin-Sternfeld, N. V. Kosheleva, V. P. Drachev, A. A. Svistunov, P. S. Timashev, L. Adler-Abramovich and E. A. Shirshin, *Angew. Chem. Int. Ed.*, 2021, **60**, 25339-25345.
150. J. Raeburn, L. Chen, S. Awhida, R. C. Deller, M. Vatish, M. I. Gibson and D. J. Adams, *Soft Matter*, 2015, **11**, 3706-3713.
151. H. Xie, J. Zhang, R. T. K. Kwok, J. W. Y. Lam, Z. Li and B. Z. Tang, *APL Mater.*, 2022, 10, 080905.
152. R. Irshad, S. Asim, A. Mansha and Y. Arooj, *J. Fluoresc.*, 2023, **33**, 1273-1303.
153. N. S. Claxton, T. J. Fellers and M. W. Davidson, in *Encyclopedia of Medical Devices and Instrumentation*, ed. J. G. Webster, John Wiley & Sons, NY, 2006.
154. A. D. Elliott, *Curr. Protoc. Cytom.*, 2020, **92**, 1.

155. P. Ravarino, N. Di Domenico, M. Barbalinardo, D. Faccio, G. Falini, D. Giuri and C. Tomasini, *Gels*, 2022, **8**, 98.
156. D. McDowall, D. J. Adams and A. M. Seddon, *Soft Matter*, 2022, **18**, 1577-1590.
157. K. McAulay, H. Wang, A. M. Fuentes-Caparros, L. Thomson, N. Khunti, N. Cowieson, H. Cui, A. Seddon and D. J. Adams, *Langmuir*, 2020, **36**, 8626-8631.
158. H. A. Barnes, J. F. Hutton and K. Walters, *An Introduction to Rheology*, Elsevier, Amsterdam, 1989.
159. D. J. Lloyd, in *Colloid Chemistry*, ed. J. Alexander, Chemical Catalog Company, New York, 1926, vol. 1, pp. 767-782.
160. K. Almdal, J. Dyre, S. Hvidt and O. Kramer, *Polym. Gels Networks*, 1993, **1**, 5-17.
161. K. Almdal, J. Dyre, S. Hvidt and O. Kramer, *Makromol. Chem., Macromol. Symp.*, 1993, **76**, 49-51.
162. S. A. Khan, J. R. Royer and S. R. Raghavan, in *Aviation Fuel Safety With Improved Fire Safety*, National Academy Press, Washington DC, 1997, ch. 6, pp. 31-46.
163. P. J. Cullen, C. P. O'Donnell and M. Houška, *J. Texture Stud.*, 2003, **34**, 1-20.
164. J. R. Mitchell, *J. Texture Stud.*, 1980, **11**, 315-337.
165. C. Fuentes, McAulay, Rogers, Dalgliesh and Adams, *Molecules*, 2019, **24**, 3855.
166. A. M. Fuentes-Caparrós, Z. Canales-Galarza, M. Barrow, B. Dietrich, J. Läuger, M. Nemeth, E. R. Draper and D. J. Adams, *Biomacromolecules*, 2021, **22**, 1625-1638.
167. F. Andriamiseza, D. Bordignon, B. Payré, L. Vaysse and J. Fitremann, *J. Colloid Interface Sci.*, 2022, **617**, 156-170.
168. K. Y. Lee and D. J. Mooney, *Chem. Rev.*, 2001, **101**, 1869-1880.
169. C. W. Barney, C. E. Dougan, K. R. McLeod, A. Kazemi-Moridani, Y. Zheng, Z. Ye, S. Tiwari, I. Sacligil, R. A. Riggleman, S. Cai, J. H. Lee, S. R. Peyton, G. N. Tew and A. J. Crosby, *Proc. Nat. Acad. Sci.*, 2020, **117**, 9157-9165.
170. J. A. Zimberlin, N. Sanabria-Delong, G. N. Tew and A. J. Crosby, *Soft Matter*, 2007, **3**, 763-767.
171. A. M. Fuentes-Caparrós, B. Dietrich, L. Thomson, C. Chauveau and D. J. Adams, *Soft Matter*, 2019, **15**, 6340-6347.
172. C. W. Barney, I. Sacligil, G. N. Tew and A. J. Crosby, *Soft Matter*, 2022, **18**, 4220-4226.
173. C. W. Barney, Z. Ye, I. Sacligil, K. R. McLeod, H. Zhang, G. N. Tew, R. A. Riggleman and A. J. Crosby, *Proc. Nat. Acad. Sci.*, 2022, **119**, e2112389119.
174. S. B. Hutchens, S. Fakhouri and A. J. Crosby, *Soft Matter*, 2016, **12**, 2557-2566.
175. S. Kundu and A. J. Crosby, *Soft Matter*, 2009, **5**, 3963-3968.
176. C. W. Barney, Y. Zheng, S. Wu, S. Cai and A. J. Crosby, *Soft Matter,* 2019, **15**, 7390-7397.
177. S. R. Polio, A. N. Kundu, C. E. Dougan, N. P. Birch, D. E. Aurian-Blajeni, J. D. Schiffman, A. J. Crosby and S. R. Peyton, *PLoS ONE*, 2018, **13**, e0204765.
178. C. E. Dougan, Z. Song, H. Fu, A. J. Crosby, S. Cai and S. R. Peyton, *Biophys. J.*, 2022, **121**, 2721-2729.
179. A. S. Mijailovic, S. Galarza, S. Raayai-Ardakani, N. P. Birch, J. D. Schiffman, A. J. Crosby, T. Cohen, S. R. Peyton and K. J. Van Vliet, *J. Mech. Behav. Biomed. Mater.*, 2021, **114**, 104168.
180. J. J. Norman, J. M. Collins, S. Sharma, B. Russell and T. A. Desai, *Tissue Eng. Part A*, 2008, **14**, 379-390.
181. M. L. Oyen, *Exp. Tech.*, 2013, **37**, 73-87.
182. B. Bhushan and M. L. B. Palacio, in *Encyclopedia of Nanotechnology*, ed. B, Bhushan, Springer, Dordrecht, 1st edn, 2012, pp. 1576-1596.

183. G. Ciccone, M. Azevedo Gonzalez Oliva, N. Antonovaite, I. Lüchtefeld, M. Salmeron-Sanchez and M. Vassalli, *J. Vis. Exp.*, 2022, **179**, e63401.
184. C. A. Schuh, *Mater. Today*, 2006, **9**, 32-40.
185. N. Shahrubudin, T. C. Lee and R. Ramlan, *Procedia Manuf.*, 2019, **35**, 1286-1296.
186. A. Su, S J. Al'Aref, in *3D Printing Applications in Cardiovascular Medicine*, ed. S. J. Al'Aref, B. Mosedegh, S. Dunham, J. K. Min, Academic Press, 1st edn, London, 2018, ch. 1, pp. 1-10.
187. H. N. Chia and B. M. Wu, *J. Biol. Eng.*, 2015, **9**, 4.
188. R. Zou, Y. Xia, S. Liu, P. Hu, W. Hou, Q. Hu and C. Shan, *Compos. B Eng.*, 2016, **99**, 506-513.
189. A. Nahmias, 3D Printed Art | Parametric House, (accessed 16.4.24, 2024).
190. I. Chiesa, C. Ligorio, A. F. Bonatti, A. De Acutis, A. M. Smith, A. Saiani, G. Vozzi and C. De Maria, *Front. Med. Technol.*, 2020, **2**, 571626.
191. S. Ramesh, O. L. A. Harrysson, P. K. Rao, A. Tamayol, D. R. Cormier, Y. Zhang and I. V. Rivero, *Bioprinting*, 2021, **21**, e00116.
192. J. A. Reid, P. A. Mollica, G. D. Johnson, R. C. Ogle, R. D. Bruno and P. C. Sachs, *Biofabrication*, 2016, **8**, 025017.
193. J. M. Unagolla and A. C. Jayasuriya, *Appl. Mater. Today*, 2020, **18**, 100479.
194. P. S. Maher, R. P. Keatch, K. Donnelly, R. E. Mackay and J. Z. Paxton, *Rapid Prototyp. J.*, 2009, **15**, 204-210.
195. L. Ning, B. Yang, F. Mohabatpour, N. Betancourt, M. Sarker, P. Papagerakis and X. Chen, *Biofabrication*, 2020, **12**, 025011.
196. A. Skardal, J. Zhang, L. McCoard, X. Xu, S. Oottamasathien and G. D. Prestwich, *Tissue Eng. Part A*, 2010, **16**, 2675-2685.
197. T. Bhattacharjee, S. M. Zehnder, K. G. Rowe, S. Jain, R. M. Nixon, W. G. Sawyer and T. E. Angelini, *Sci. Adv.*, 2015, **1**, e1500655.
198. P. S. Gungor-Ozkerim, I. Inci, Y. S. Zhang, A. Khademhosseini and M. R. Dokmeci, *Biomater. Sci.*, 2018, **6**, 915-946.
199. K. Holzl, S. Lin, L. Tytgat, S. Van Vlierberghe, L. Gu and A. Ovsianikov, *Biofabrication*, 2016, **8**, 032002.
200. A. S. Theus, L. Ning, B. Hwang, C. Gil, S. Chen, A. Wombwell, R. Mehta and V. Serpooshan, *Polymers*, 2020, **12**, 2262.
201. J. Mewis and N. J. Wagner, *Adv. Colloid Interface Sci.*, 2009, **147-148**, 214-227.
202. A. Chalard, M. Mauduit, S. Souleille, P. Joseph, L. Malaquin and J. Fitremann, *Addit. Manuf.*, 2020, **33**, 101162.
203. H. Jian, M. Wang, Q. Dong, J. Li, A. Wang, X. Li, P. Ren and S. Bai, *ACS Appl. Mater. Interfaces*, 2019, **11**, 46419-46426.
204. M. C. Nolan, A. M. Fuentes Caparrós, B. Dietrich, M. Barrow, E. R. Cross, M. Bleuel, S. M. King and D. J. Adams, *Soft Matter*, 2017, **13**, 8426-8432.
205. W. T. Truong, Y. Su, D. Gloria, F. Braet and P. Thordarson, *Biomater. Sci.*, 2015, **3**, 298-307.

Chapter 2

Multi-layered 3D Printed Low Molecular Weight Hydrogels

Chapter 2 – Multi-layered 3D Printed Low Molecular Weight Hydrogels

This Chapter is adapted in part from the following publication:

‘Multi-layer 3D printed dipeptide-based low molecular weight gels’

Soft Matter, 2022, **18**, 5960-5965.

M. J. S. Hill and D. J. Adams

Open Access: Published under CC-BY

The gelator molecules used in this chapter were synthesised by B. Dietrich and D. J. Adams. All other experiments and work were carried out by M. J. S. Hill.

2.1 Introduction

3D printing is a fabrication technique that enables the sequential controlled deposition of layers of material to produce a designed structure.[1] Whilst most 3D printers commonly achieve this through the extrusion of heated plastic filament, other substrates can be used.[2] Through suitable modifications to a printer, hydrogels can be extruded and effectively printed.[3, 4] This has been demonstrated for a range of different gels, with well-defined patterns produced.[4] Controlled formation of hydrogels in this manner has promising biomedical applications, particularly within tissue engineering and the delivery of drugs.[5-10] Many reported polymer and peptide based extruded hydrogel systems can be found in the literature.[11] Often these gels are used as 'bioinks' and are initially deposited as viscous gelator solutions.[12, 13] Gelation is then triggered by a range of stimuli, such as a change in temperature,[14] UV photocuring,[15-17] addition of cross-linking agents,[18] printing into fixing solutions or pre-existing gels.[19, 20] Compared to this, significantly fewer examples of 3D printed low molecular weight gels have been reported.[21] These physical gels contain underlying networks built from reversible non-covalent interactions. These reversible links allow this underpinning network to be deformed, broken and reform, enabling recovery of strain from applied shear stress.[22] The gels are therefore thixotropic, giving them potential as a substrate for 3D bioprinting. Like their chemical counterparts, low molecular weight gels can also be deposited as a gelator solution that is subsequently gelled through the above-mentioned means.[4, 12, 13] However, unlike chemical gels, some low molecular weight gels can be pre-formed and subsequently extruded.[23-25] As gelation precedes extrusion rather than occurring post-printing, this should conceptually enable predefined properties within the final printed material by choosing appropriate gels to print.[23] This relies upon the formed gels being extrudable and will also be determined by how the materials properties are affected by the extrusion process.[23, 26]

The majority of existing 3D printed gels systems comprise printed gel layers formed from a single gelator.[12, 13, 21, 23, 26] These rudimentary systems ease setup, initial testing and optimisation of the printing process,[23] but have limited overall functionality. 3D printing enables gels to be produced in a range of shapes rather than simply adopting that of the vessel or mould they are more traditionally 'cast' in.[2] Through varying the gelator, or subsequent concentrations, it also enables the layering of different printed gels to give a heterogenous construct.[26] This mirrors biological tissue better than traditional gels that are typically of a more homogenous composition,[27] allowing for multi-layered systems that are a significant step towards this key goal within the field of bioprinting.[28, 29] Different component materials enables the mechanical properties of the sample to be varied throughout, either as subtle variations or more significant differences in strength or stiffness.[26, 30]

Multi-layered gel systems lead to questions about what occurs when separate independent gels are extruded in close proximity, producing a boundary. Systems that rely on gelation occurring post extrusion could lead to integration of initially separate materials if gelator solutions were to amalgamate after extrusion, but before gelation.[31] If this were to occur, a difference in mechanical properties would not be expected to be seen across these border regions. Where differing mechanical properties are induced with different gelator concentrations, layers may not remain independent if diffusion occurs, homogenising these dynamic systems. Extruded pre-formed gel would be expected to be more likely to remain distinct, due to preservation of the pre-existing gelator network during extrusion.[23, 26] Here, separately printed materials would remain as such, despite being printed in close proximity to one another.

We have previously demonstrated a 3D printed low molecular weight gel system where gel layers with different gelator concentration, and thus differing mechanical properties, were used to produce a multi-layered sample with heterogenous mechanical properties throughout.[26] This system used arguably the most prominent example from the well-established Fmoc protected dipeptide family of low molecular weight gelators, FmocFF (Fig 2.1).[32, 33]

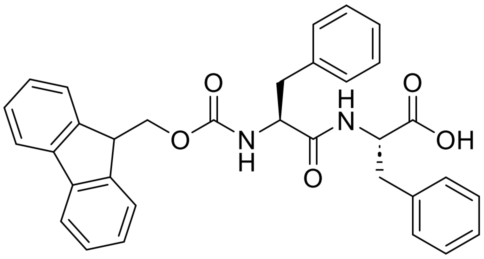

Figure 2.1 Chemical structure of FmocFF.

FmocFF can form hydrogels at physiological pH through a range of gelation triggers, most commonly solvent-switching and pH.[27, 34-36] This gives promise as a soft material with applications in cell culture or tissue engineering within the biomedical field.[32, 33, 37] Solvent triggered FmocFF gels have been successfully 3D printed previously, wherein a modified 3D printer was used to extrude the pre-formed gels from syringes.[23] These extruded gels were shown to possess similar mechanical properties post-printing to their unprinted equivalents (Figure 2.2). Slight differences within the absolute magnitudes of *G*′ and *G*′′ and breakdown profile were observed.

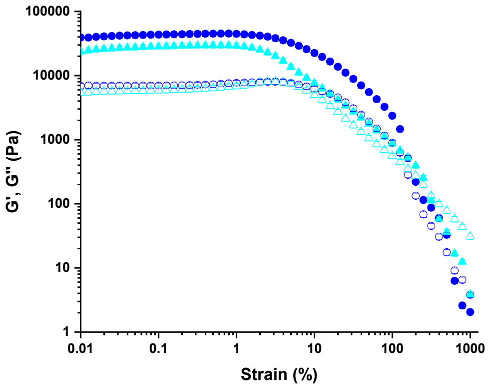

Figure 2.2 Rheological strain sweeps comparing samples of single layers of unprinted (dark blue circles) and printed (light blue triangles) of FmocFF gel (5 mg mL^{-1}, DMSO : H_2O 20%, printed at 4 µL mm^{-1}). *G*′ is represented by filled shapes and *G*′′ hollow shapes.[23]

In this chapter, the potential for multiple layers of gels printed atop one another was also demonstrated.[23] This was then developed beyond multiple layers of identical gel, to produce gel layers of different stiffness.[26] Using these to construct a sample possessing heterogenous mechanical properties moved a step closer to the ultimate goal of mimicking natural tissue, which is itself inherently non-homogenous.[28-30] Within this study, the gelator concentration was varied to achieve differences in stiffness within the subsequent gel layers.[26] A stiffer gel is produced from increased gelator concentration, leading to a more densely populated underlying fibrous gelator network.[38] The relative position of these stiffer layers within the sample, as well as their ratio to less stiff gel layers was shown to impact the samples overall mechanical properties.[26]

This chapter will demonstrate successful 3D printing of multi-layered constructs that comprise layers of gel stemming from two different LMWGs, each with their unique composition and microstructure. These gel components each have unique mechanical properties, resulting in overall mechanical properties dictated by the specific combination of gel layers. Oscillatory rheology will be used to clearly show these differences. We will also explore the interfacing of printed solvent switch triggered low molecular weight gels coming together at gel: gel boundaries when printed in close proximity to one another. This is shown via confocal microscopy and enabled through the incorporation of multiple different fluorescent dyes. These further develop the already established 3D printing of pre-formed low molecular weight gels, whilst allowing for a better understanding of how these materials behave post printing.

2.2 Results and Discussion

2.2.1 3D printing FmocFF and 2NapFV gels

The effective extrusion and subsequent 3D printing of dipeptide based low molecular weight gels has been previously demonstrated.[23, 26, 31] Through trialling a few different low molecular weight gels thought to be suitable, a system was devised allowing for the extrusion of pre-formed low molecular weight gels from syringes.[23, 26] As part of this, optimisations to the extrusion and overall printing process, including parameters such as printing speed, height and shear rate (γ), were made to ensure reproducible printed material.[23] It also involved exploring gels formed via different gelation triggers, such as pH or solvent-switching. The latter proved to be most suitable for printing within the system used. To form solvent triggered gels, gelator is dissolved into an organic solvent, in this case DMSO. Water is subsequently added, driving the self-assembly of the now insoluble gelator molecules. Strips of printed gel could then be used to build up more complex shapes and designs (Figure 2.3).

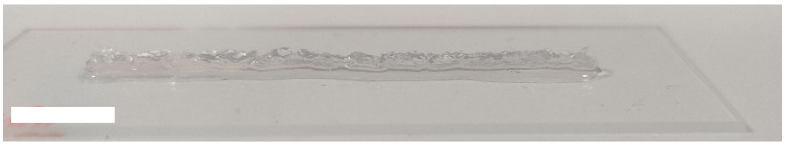

Figure 2.3 Image of a 50 mm strip of FmocFF solvent-switch (5 mg mL^{-1} DMSO:H_2O, 20:80) gel printed onto a glass microscope slide. Scale bar (white) = 10 mm.

FmocFF was used as the initial gelator from which to make low molecular weight gels for printing (Figure 2.1).[23] The mechanical properties of the printed gels were compared to their unprinted equivalents, via oscillatory rheology (Figure 2.2). Layers of FmocFF gel could be formed by printing in a serpentine pattern within a square mould (Figure 2.4a). Additional layers could then be sequentially printed on top of one another to form a multi-layered sample (Figure 2.4b), with the overall stiffness increasing with additional printed layers (Figure 2.4c).[26]

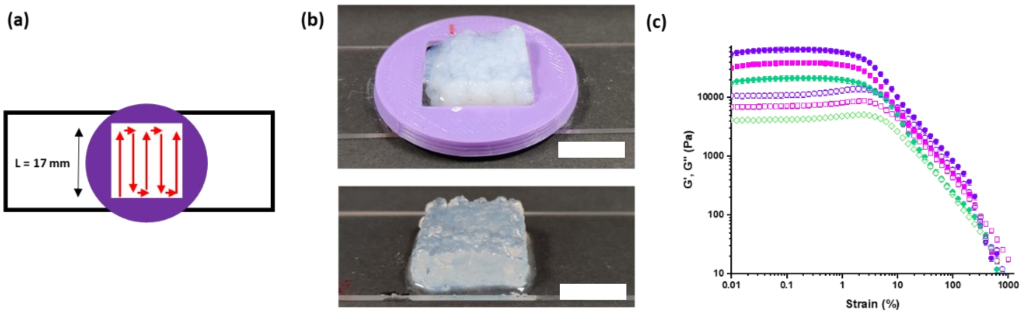

Figure 2.4 a) Cartoon schematic of printing pattern used to form gel layers in a mould (purple). b) Printed multi-layered FmocFF gels. c) Rheological strain sweeps (Strain: 0.01 – 1000%) of samples comprising 1 (green), 2 (pink) and 3 (purple) layers of printed FmocFF gel (5 mg mL^{-1}, ϕ_{DMSO} = 0.2, printed at 4 µL mm^{-1}). G′ is represented by filled shapes and G′′ hollow shapes. Scale bars (white) = 10 mm.

To produce heterogeneous mechanical properties within a sample, different gelators were used to form gels layers, each of an inherently different stiffness. In the absence of a definitive list of printable gelators or simply a guiding parameter set that would imply successful extrusion, we selected 2NapFV (Figure 2.5a), a known gelator related to FmocFF, to make alternate gel layers from.[35] When formed via a DMSO : H_2O solvent switch, 2NapFV gels were shown to be printable from a syringe in the same way as FmocFF gels have been previously shown to be (Figure 2.5b).[23, 26] These gels also displayed the same trend in mechanical properties between printed and unprinted equivalents when compared via rheology (Figure 2.5c). Both gels displayed good shear recovery of mechanical properties post-printing (see Appendix A, Figures A.1 and A.2).

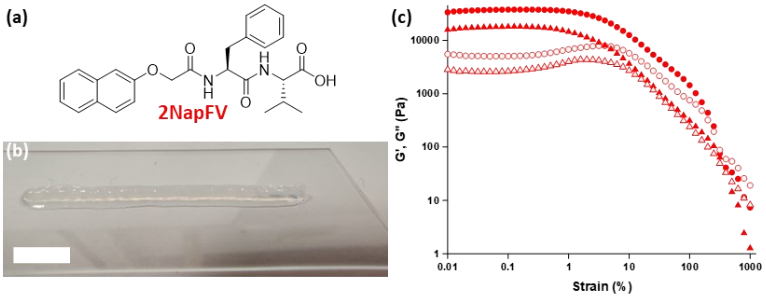

Figure 2.5 a) Chemical structure of 2NapFV. b) Image of a 50 mm strip of 2NapFV gel printed onto a glass microscope slide. c) Rheological strain sweeps comparing samples of single layers of unprinted (circles) and printed (triangles) 2NapFV gel (5 mg mL^{-1}, ϕ_{DMSO} = 0.2, printed at 4 µL mm^{-1}). *G′* is represented by filled shapes and *G′′* hollow shapes. Scale bar (white) = 10 mm.

2.2.2 Different network microstructures of component gels

These choices were, in part, influenced by the distinct differences in microstructure observed in 2NapFV gels compared to those of FmocFF when visualised with confocal microscopy (Figure 2.6). Coupled with the differences in opacity, where 2NapFV gels are turbid whilst FmocFF gels are translucent, these characteristics enable confident identification of the two materials across difference length scales, even when printed in close proximity (Figure 2.6).

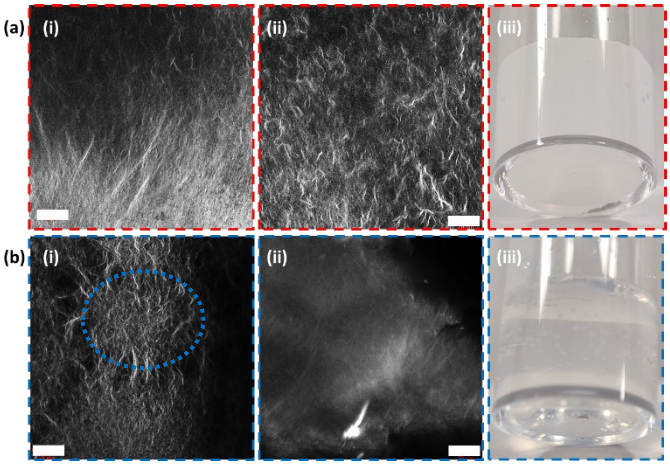

Figure 2.6 Confocal microscopy of (i) unprinted and (ii) printed (4 µL mm^{-1}) (a) 2NapFV & (b) FmocFF gels (5 mg mL^{-1}, ϕ_{DMSO} = 0.2, 400 µL, Nile blue 2 µL mL^{-1} at 0.1 wt%), alongside (iii) exemplar images of their differences in turbidity when formed as bulk gels. Scale bars (white) = 20 µm. An example of a spherulite-like domain is highlighted within image (bi).

Whilst both FmocFF and 2NapFV gels present distinct spherulite-like microstructures when formed *via* a solvent-switch trigger, the fibre and spherulite size within these leads to clear differences under sufficiently high magnification (Figure 2.6). Here, it can be seen that the 2NapFV gels show a seemingly more uniform network with fibres, and thus spherulites, spanning a greater distance compared to those within FmocFF gels. In extruded gels, these visual differences are accentuated, with distinct fibres and clear spherulites no longer seen within the FmocFF gels (Figure 2.6b). This is not the case for the 2NapFV gels, with clear fibres persisting within printed samples, albeit with obvious differences to non-printed gels (Figure 2.6a).

2.2.3 Multi-layered 3D printed gel samples

2NapFV and FmocFF gels were used to produce three layered systems, with all possible combinations being formed as separate samples. Two separate studies were carried out here, with one using layers of non-printed gels and the other using extruded gel (Figure 2.7). The former were cast directly as consecutive layers of solvent-switch triggered gel in full height moulds.[26] The latter were printed in a serpentine pattern within a mould to form the component gel layers. As the printed gels have been pre-formed prior to printing and the cast gels are allowed to fully finish gelation before the addition of a subsequent layer, each layer is formed from a single gelator (Figure 2.7). As demonstrated in Figure 2.4c, samples produced from multiple layers of gel show an increase in rheological moduli compared to single layer equivalents.[26] This is the same trend that would be seen moving from a thinner to a thicker cast layer of gel, due to the increased amount of material within the sample.[26]

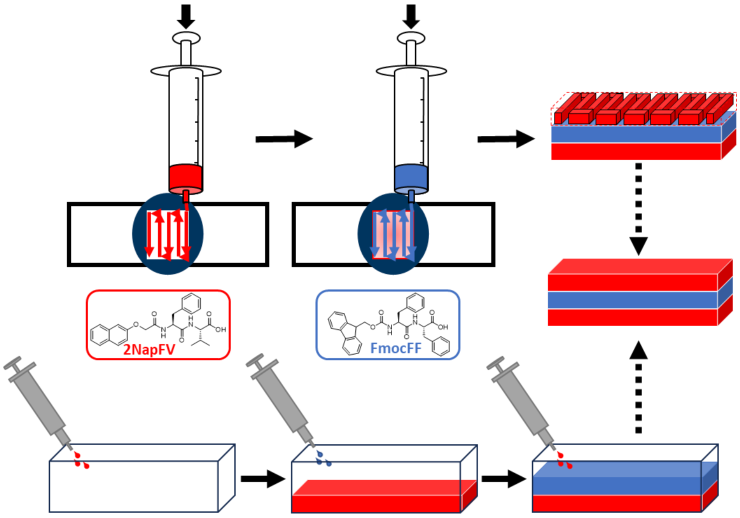

Figure 2.7 Simplified cartoon diagram showing how multi-layered gel samples were formed either though 3D printed (top) or cast (bottom) gel layers. The example shown represents 2NapFV (red) and FmocFF (blue) solvent switch gels (5 mg mL^{-1}, ϕDMSO = 0.2) used to form a multi-layered gel sample with the overall layer order of 2NapFV: FmocFF: 2NapFV gels (top to bottom).

Rheology was carried out on both the printed and non-printed multi-layered samples (Figure 2.8). As expected, the unprinted gel samples consistently displayed higher mechanical stiffness than their printed equivalents (Figure 2.8c), with the results also being more reproducible. This reduction in stiffness for the printed gels may stem from the extrusion process, where high stress is imparted on the printed material.[39] For the set of unprinted samples, no clear trend in G′ values is observed. It is noted that sample composition 4 is significantly stiffer than the rest of the unprinted sample set. Why this occurs is unclear. Whilst it contains mostly the mechanically stiffer FmocFF gel layers, and these are making up the majority of contact with the rheometer geometry, one would expect it to be less stiff than sample composition 1, which only contains FmocFF gel layers. In the printed gel samples, an overall reduction in G′ is seen upon moving from having a majority of FmocFF layers to a majority of 2NapFV layers (Figure 2.8c Sample 4 → 5). This printed set display a greater difference in stiffness between samples formed solely of FmocFF (Figure 2.8c, Sample 1) and those of only 2NapFV (Figure 2.8c, Sample 8) than the unprinted set. This discrepancy may suggest 2NapFV gels to be less suitable for extrusion and printing than FmocFF gels.

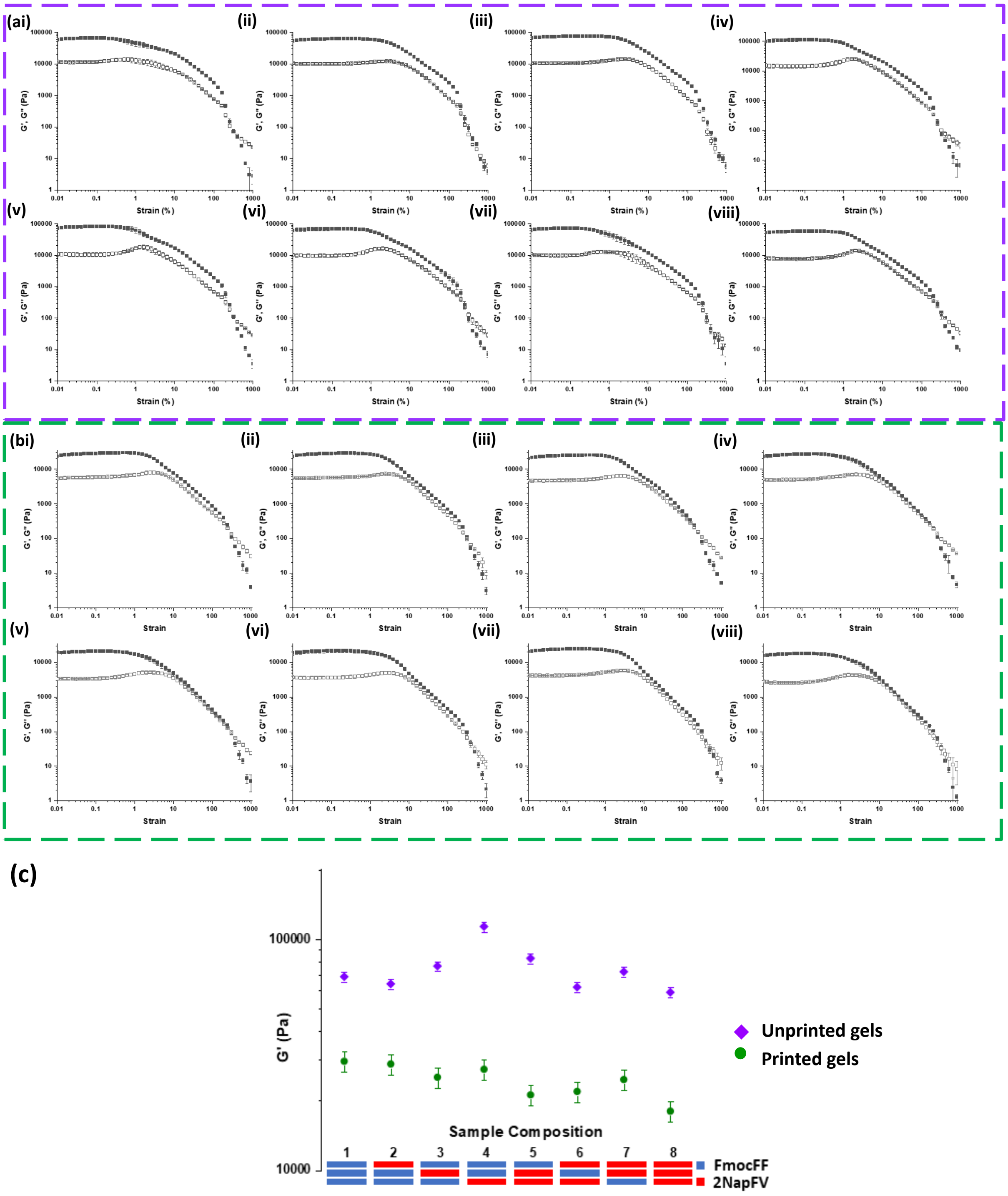

Figure 2.8 Strain sweeps for (a) unprinted and (b) printed multi-layered gel samples (i) **1** (ii) **2** (iii) **3** (iv) **4** (v) **5** (vi) **6** (vii) **7** (viii) **8**. G′ is represented by filled shapes and G′′ hollow shapes. Printed gels were printed at 4 µL/mm and a shear rate (γ) of 1500 s^{-1}. Measurements were carried out on samples prepared in triplicate, with error bars representing the standard deviation derived from averaging the three subsequent results. (c) Summary of averaged G′ values of multi-layered unprinted (purple diamonds) and printed (green circles) gel samples formed from FmocFF (blue and 2NapFV gels (5 mg mL^{-1}, **ϕ**DMSO = 0.2, printed at 4 µL mm^{-1}) with sample layer composition shown. FmocFF gel layers are blue, whilst 2NapFV layers are red.

2.2.4 Probing the borders of close printed gels

To better understand this system as a whole, the interface between printed materials was investigated. The majority of previously demonstrated 3D printed low molecular weight gels extrude a viscous gelator solution rather than the gel itself, with gelation occurring post-extrusion after exiting the extrusion nozzle or shortly thereafter.[12, 13, 40] Typically, extruded material is gelated through solvent exchange in baths of organic solvent or within ‘fixing’ ionic solutions.[12, 13, 31, 40] This may lead to partially formed gels deposited in close proximity to one another, allowing for amalgamation via the formation of crosslinks between the initially separate materials during the ongoing gelation, not dissimilar to the annealing process shown in some low molecular weight gels.[41-43] This integration could produce a final material that is more homogenous and uniform, potentially improving mechanical properties over a sample built up from separate strips of printed gel. Whilst this may allow for printed gels to ‘settle’ into the vessel in which they are printed, it risks losing the spatial control and pre-programmed design that are key advantages 3D printing of these materials would bring.[2, 23]

Given that our system uses the printing of pre-formed low molecular weight gels, in which gelation is fully complete prior to extrusion, integration of separately printed material would be expected not to occur.[23] Gels formed from 2NapFV, FmocFF and related gelators are often thixotropic materials that demonstrate shear recovery.[23] This is especially true of gels formed via a DMSO: H_2O solvent switch trigger. It is thought that the gelator network present within these gels, composed of spherulite-like domains, helps facilitate the partial recovery of a pre-stressed deformed structure once applied shear is removed.[44, 45] The underlying gelator network formed during gelation prior to extrusion persists throughout the printing process. Thus, gel strips printed in close proximity to one another *via* this process would be expected to remain independent. Examining these borders for potential integration of printed gels is important to fully understanding these systems. If distinct borders are maintained, that clearly show a non-interfacing gel-gel boundary between printed strips of gel, then an applied stress would cause a response in which layers within a sample would act independently (Figure 2.9ai). But, if separately extruded layers did integrate with one another, then the overall mechanical properties of the sample may not equate to the sum of contributions of the individual component layers (Figure 2.9aii).

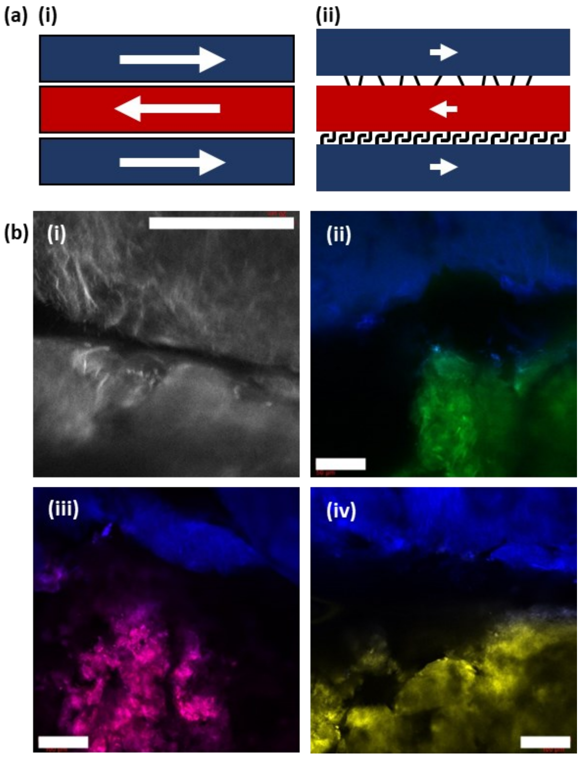

Figure 2.9 (a) Cartoon diagram of multi component 3D printed multi-layered samples in which layers have (i) distinct gel-gel boundaries and (ii) integrated with cross links. (b) Multi-dyed confocal microscopy images of a boundary formed by printing 2NapFV (Nile blue A, 2 µL mL^{-1} at 0.1 wt%, top) and FmocFF (Nile blue A (i), fluorescein (ii), Nile red (iii), thioflavin T (iv), 2 µL mL^{-1} at 0.1 wt%, bottom) gels (5 mg mL^{-1}, ϕ DMSO 0.2, 4 µL mm^{-1}) alongside each other. Scale bars (white) represent 100 µm.

Probing these boundaries was carried out with confocal microscopy to determine the degree of integration between layers printed in close proximity. This was enabled by the incorporation of fluorescent dyes during gelation to allow for effective imaging of the networks present within printed gels. These are typically hydrophobic or lyophilic molecules that are assimilated into the hydrophobic gelator fibres during self-assembly. Initially, strips of the same gel printed alongside one another were examined but making any confident observations and assigned proved difficult.

To remedy this, strips of 2NapFV gel and FmocFF gel were printed alongside one another and imaged. These two different gels are readily distinguishable by their different microstructures via confocal microscopy, even after printing (Figure 2.6). This distinction enables the boundaries between these printed gels to be examined (Figure 2.9b). Even using the same fluorescent dye within both gels (Nile blue A, Figure 2.9bi), two distinct networks are clearly visible. The network of 2NapFV retains its fibrous structure after extrusion, whereas FmocFF appears more amorphous, with not many distinct fibres observed post extrusion (Figure 2.9bi, top and bottom respectively). Most importantly, the two gels remain clearly separate by a solvent filled gap. This gap between gels was checked across different depths of field to ensure confidence in this defined gel-gel border. No integration of gels was shown and the void persists the whole length of printed gel strips. This indicates that the strips of gel do stay separate and maintain a boundary.

To better highlight this, a two-dye setup was adopted (Figure 2.9b). This system gives better contrast and increases confidence in observations when probing the boundaries. 2NapFV gels remained labelled with Nile blue A, whilst FmocFF gels were dyed with Fluorescein (Figure 2.9bii). This imaging highlighted the relative positions of the two gels, allowing easy distinction. Whilst helping confirm the lack of integration of the gels, fine details within the FmocFF gels were no longer seen, likely due to the hydrophilicity of the fluorescein dye. Instead of associating with the gelator fibres within the FmocFF gels, the immobilised water is instead shown. This behaviour led to concerns over the potential diffusion of the dye between the two separate gels, potentially leading to non-representative imaging. To avoid this, two lipophilic dyes, Nile red and thioflavin T, were used to stain FmocFF gels instead of fluorescein (Figure 2.9biii and 2.9biv respectively). These retained the fine detail on the FmocFF gel microstructure whilst supporting the lack of integration between the two separately extruded 2NapFV and FmocFF gels previously observed. Collectively, these observations demonstrate a lack of integration between extruded gels due to a maintained boundary that means these gels layers remain independent. Whilst there is expected to be solvent between layers of printed gel, no indications of slipping are seen within their rheology.

2.3 Conclusion

We have demonstrated the ability to 3D print multi-layered constructs in which the individual gel layers are formed from different gelators. This was achieved through the extrusion of preformed solvent-switch triggered gels rather than post-printing gelation. We have previously shown DMSO : H_2O triggered low molecular weight gels to be more suitable to 3D printing applications than pH triggered gels, owing to the different microstructure produced.[23] Both the overall composition and relative ordering of the different gel layers were shown to be significant in determining the overall mechanical properties of multi-layered systems. The degree of interaction between printed gels was explored *via* confocal microscopy, with different underlying microstructures highlighted with different fluorescent dyes. Initial indications suggest that a distinct boundary between separately extruded material is maintained. This is expected to impact the overall mechanical properties of multi-layered printed gel systems. We hope this system shows the potential for further examples of multi-layered printed gels and provides insight towards future applications of these systems.

2.4 Experimental

Materials:

LMWGs FmocFF (F = phenylalanine) and 2NapFV (V = valine) were synthesized as described previously by Bart Dietrich and Dave Adams (University of Glasgow).[27] De-ionised water was used throughout. DMSO and 3 mL polypropylene syringes were purchased from Fisher Scientific and used as received. Nile blue A, Nile red, fluorescein and thioflavin T fluorescents dyes were purchased from Sigma Aldrich (Merck) and used as received.

Preparation of LMWG solutions and gels:

LMWGs FmocFF (F = phenylalanine) and 2NapFV (V = valine) were used to form solvent-switch triggered hydrogels as previously outlined.[27, 35] A known amount of gelator was dissolved in DMSO (at a concentration of 25 mg mL^{-1}), sonicated for 2 minutes, and diluted with water in one aliquot to give gels at a final gelator concentration of 5 mg mL^{-1}, and a volume fraction (ϕ) of DMSO of 0.2. For printable gels, the gelator DMSO solution was transferred to a 3 mL PP syringe by needle and syringe. The water aliquot was then added after, in the same manner.

Gels were either formed within, or extruded into, 3D printed plastic square shaped moulds (19.5 × 19.5 × 5 mm, Figure 2.10b) adhered to a borosilicate glass microscope slide with Araldite®.[26] Gels were left overnight within a sealed hydrated environment before being printed or characterized. For printed gels, they were sealed within the syringe they were formed in. For non-printed gels, the sample, mould and slide it was mounted on were placed in a large petri dish with wet blue roll and closed with parafilm.

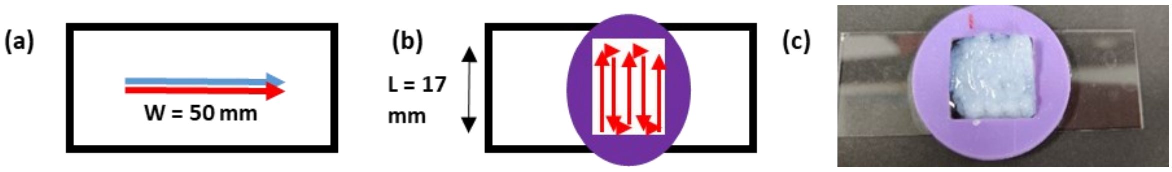

Figure 2.10 Cartoon diagrams for printed (a) confocal and (b) rheological samples. (c) Example of gel 3D printed in a custom 3D printed square shaped holder. Scale bar (white) = 10 mm.

Preparing unprinted multi-layered gels:

For unprinted samples, layers of gel (1.065 mL) were formed directly within the mould. The gelator solution was pipetted in and spread, where necessary, to give even coverage, with an aliquot of water gently pipetted in immediately after to trigger gelation. Each layer was left in a sealed vessel for 30 minutes before the addition of the next layer.[26]

3D printed gels:

A modified RepRap Ormerod 2 (version 528.4) 3D printer was used to extrude 3D printed hydrogels.[23] Printed samples were formed by first making gels (2 mL) within 3 mL polypropylene syringes. The syringes were then loaded into a custom gel 3D printer and used to print layers of pre-formed gel in a serpentine pattern at an extrusion rate of 4 µL mm^{-1} and a shear rate (γ) of 1500 s^{-1} (Figure 2.10b and c), as previously described.[23] Consecutive printed layers were added immediately after one another.

Rheological measurements:

Samples for rheology were created by the sequential formation of either printed or non-printed layers of FmocFF and 2NapFV gels in different combinations.[23, 26] Rheological measurements were carried out using a MCR 301 rheometer (Anton Paar), fitted with a cup and four-bladed vane geometry (ST10-4V-8.8/97.5-SN1910), and Rheoplus/32 v3.40 software. All measurements were carried out in triplicate, at 25 °C, with a measurement gap of 1.8 mm used.

G′ values shown in summary plot for comparison (Figure 2.8c) were taken as an average of those in the linear viscoelastic region from individual strain sweeps (strain = 0.01% to 1000%, frequency = 10 rad s^{-1}, T = 25 °C) of non-printed (Figure 2.8a) and printed (Figure 2.8b) multi-layer samples.

Confocal microscopy:

For imaging, Nile blue A, fluorescein, Nile red and thioflavin T dyes (0.1 wt% aqueous solution, 2 µL per mL of gel) were incorporated into gels to allow for observation by confocal fluorescence microscopy using a Zeiss LSM 710 confocal microscope fitted with Zeiss N-Achroplan 10× and LD EC Epiplan NEUFLUAR 50× (0.55 DIC) objectives. Unprinted gels (5 mg mL^{-1}, 2 mL, ϕ DMSO 0.2) were formed directly within the central well of Greiner Bio-one CELLview dishes.

To study the microstructure of individual printed gels, single lines of either FmocFF or 2NapFV gel were printed directly onto standard microscope slides (Figure 2.10a) To probe the boundary between printed lines of gel, strips of FmocFF and 2NapFV gel were printed on top of one another and then rotated 90°. For multi-dye imaging, 2NapFV gels were formed with Nile blue A dye incorporated and FmocFF gels with Fluorescein, Nile red or thioflavin T.

2.5 References

1. H. N. Chia and B. M. Wu, *J. Biol. Eng.*, 2015, **9**, 4.
2. T. Jungst, W. Smolan, K. Schacht, T. Scheibel and J. Groll, *Chem. Rev.*, 2016, **116**, 1496-1539.
3. T. Boland, V. Mironov, A. Gutowska, E. A. Roth and R. R. Markwald, *Anat. Rec.*, 2003, **272A**, 497-502.
4. N. A. Sather, H. Sai, I. R. Sasselli, K. Sato, W. Ji, C. V. Synatschke, R. T. Zambrotta, J. F. Edelbrock, R. R. Kohlmeyer, J. O. Hardin, J. D. Berrigan, M. F. Durstock, P. Mirau and S. I. Stupp, *Small*, 2021, **17**, 2005743.
5. M. Rodrigues, A. C. Calpena, D. B. Amabilino, M. L. Garduño-Ramírez and L. Pérez-García, *J. Mater. Chem. B*, 2014, **2**, 5419.
6. S. Gupta, M. Singh, A. R. M, P. S. Yavvari, A. Srivastava and A. Bajaj, *RSC Adv*., 2016, **6**, 19751-19757.
7. K. J. Skilling, F. Citossi, T. D. Bradshaw, M. Ashford, B. Kellam and M. Marlow, *Soft Matter*, 2014, **10**, 237-256.
8. X. Li, Y. Wang, C. Yang, S. Shi, L. Jin, Z. Luo, J. Yu, Z. Zhang, Z. Yang and H. Chen, *Nanoscale*, 2014, **6**, 14488-14494.
9. Y. Zhou and X. Li, *Chin. Chem. Lett*., 2017, **28**, 1835-1840.
10. J. L. Drury and D. J. Mooney, *Biomaterials*, 2003, **24**, 4337-4351.
11. J. Li, R. Xing, S. Bai and X. Yan*, Soft Matter*, 2019, **15**, 1704-1715.
12. A. Chalard, M. Mauduit, S. Souleille, P. Joseph, L. Malaquin and J. Fitremann, *Addit. Manuf.*, 2020, **33**, 101162.
13. C. C. Piras, A. G. Kay, P. G. Genever, J. Fitremann and D. K. Smith, *Chem. Sci*., 2022, **13**, 1972-1981.
14. R. Suntornnond, J. An and C. K. Chua, *Macromol. Mater. Eng*., 2017, **302**, 1600266.
15. L. Ouyang, C. B. Highley, C. B. Rodell, W. Sun and J. A. Burdick, *ACS Biomater. Sci. Eng*., 2016, **2**, 1743-1751.
16. L. Ouyang, C. B. Highley, W. Sun and J. A. Burdick, *Adv. Mater.*, 2017, **29**, 1604983.
17. L. C. Hsiao, A. Z. M. Badruddoza, L. C. Cheng and P. S. Doyle, *Soft Matter*, 2017, **13**, 921-929.
18. L. Shi, H. Carstensen, K. Hölzl, M. Lunzer, H. Li, J. Hilborn, A. Ovsianikov and D. A. Ossipov, *Chem. Mater*., 2017, **29**, 5816-5823.
19. Q. Liu, Q. Li, S. Xu, Q. Zheng and X. Cao, *Polymers*, 2018, **10**, 664.
20. C. B. Highley, C. B. Rodell and J. A. Burdick, *Adv. Mater*., 2015, **27**, 5075-5079.
21. F. Andriamiseza, D. Bordignon, B. Payré, L. Vaysse and J. Fitremann, *J. Colloid Interface Sci*., 2022, **617**, 156-170.
22. J. P. Schneider, D. J. Pochan, B. Ozbas, K. Rajagopal, L. Pakstis and J. Kretsinger, *J. Am. Chem. Soc.*, 2002, **124**, 15030-15037.
23. M. C. Nolan, A. M. Fuentes Caparrós, B. Dietrich, M. Barrow, E. R. Cross, M. Bleuel, S. M. King and D. J. Adams, *Soft Matter*, 2017, **13**, 8426-8432.
24. H. H. Susapto, D. Alhattab, S. Abdelrahman, Z. Khan, S. Alshehri, K. Kahin, R. Ge, M. Moretti, A.-H. Emwas and C. A. E. Hauser, *Nano Lett*., 2021, **21**, 2719-2729.
25. B. Raphael, T. Khalil, V. L. Workman, A. Smith, C. P. Brown, C. Streuli, A. Saiani and M. Domingos, *Mater. Lett*., 2017, **190**, 103-106.
26. A. M. Fuentes-Caparrós, Z. Canales-Galarza, M. Barrow, B. Dietrich, J. Läuger, M. Nemeth, E. R. Draper and D. J. Adams, *Biomacromolecules*, 2021, **22**, 1625-1638.

27. D. J. Adams, M. F. Butler, W. J. Frith, M. Kirkland, L. Mullen and P. Sanderson, *Soft Matter*, 2009, **5**, 1856-1862.
28. M. P. Nikolova and M. S. Chavali, *Bioact. Mater*., 2019, **4**, 271-292.
29. G. Liu, Z. Ding, Q. Yuan, H. Xie and Z. Gu, *Front. Chem*., 2018, **6**, 439.
30. F. Yanagawa, S. Sugiura and T. Kanamori, *Regen. Ther*., 2016, **3**, 45-57.
31. H. Jian, M. Wang, Q. Dong, J. Li, A. Wang, X. Li, P. Ren and S. Bai, *ACS Appl. Mater. Interfaces*, 2019, **11**, 46419-46426.
32. V. Jayawarna, M. Ali, T. A. Jowitt, A. F. Miller, A. Saiani, J. E. Gough and R. V. Ulijn, *Adv. Mater*., 2006, **18**, 611-614.
33. A. Mahler, M. Reches, M. Rechter, S. Cohen and E. Gazit, *Adv. Mater*., 2006, **18**, 1365-1370.
34. C. Tang, A. M. Smith, R. F. Collins, R. V. Ulijn and A. Saiani, *Langmuir*, 2009, **25**, 9447-9453.
35. L. Chen, S. Revel, K. Morris, L. C. Serpell and D. J. Adams, *Langmuir*, 2010, **26**, 13466-13471.
36. V. Jayawarna, S. M. Richardson, A. R. Hirst, N. W. Hodson, A. Saiani, J. E. Gough and R. V. Ulijn, *Acta Biomater*., 2009, **5**, 934-943.
37. T. Liebmann, S. Rydholm, V. Akpe and H. Brismar, *BMC Biotechnol*., 2007, **7**, 88.
38. F. M. Menger and K. L. Caran, *J. Am. Chem. Soc.*, 2000, **122**, 11679-11691.
39. J. A. Reid, P. A. Mollica, G. D. Johnson, R. C. Ogle, R. D. Bruno and P. C. Sachs, *Biofabrication*, 2016, **8**, 025017.
40. A. Chalard, P. Joseph, S. Souleille, B. Lonetti, N. Saffon-Merceron, I. Loubinoux, L. Vaysse, L. Malaquin and J. Fitremann, *Nanoscale*, 2019, **11**, 15043-15056.
41. S. Panja, A. M. Fuentes-Caparrós, E. R. Cross, L. Cavalcanti and D. J. Adams, *Chem Mater*., 2020, **32**, 5264-5271.
42. P. Ravarino, S. Panja, S. Bianco, T. Koev, M. Wallace and D. J. Adams, *Angew. Chem. Int. Ed*., 2023, **62**, e202215813.
43. A. M. Fuentes-Caparrós, F. De Paula Gómez-Franco, B. Dietrich, C. Wilson, C. Brasnett, A. Seddon and D. J. Adams, *Nanoscale*, 2019, **11**, 3275-3280.
44. X. Huang, S. R. Raghavan, P. Terech and R. G. Weiss, *J. Am. Chem. Soc.*, 2006, **128**, 15341-15352.
45. C. Yan, A. Altunbas, T. Yucel, R. P. Nagarkar, J. P. Schneider and D. J. Pochan, *Soft Matter*, 2010, **6**, 5143-5156.

Chapter 3

Spatially Constrained Low Molecular Weight Gels

Chapter 3 - Spatially Constrained Low Molecular Weight Gels

This Chapter is adapted in part from the following publication:

‘Effect of Imposing Spatial Constraints on Low Molecular Weight Gels’

Biomacromolecules, 2023, **24**, 9, 4253-4262.

M. J. S. Hill, A. M. Fuentes-Caparrós and D. J. Adams

Open Access: Published under CC-BY

The gelator molecules used in this chapter were synthesised by B. Dietrich, D. J. Adams, and M. J. S. Hill.

Initial experiments and work on 2NapFF solvent-triggered gels (including confocal microscopy imaging and cavitation rheology and processing this data) were carried out by **Ana María Fuentes-Caparrós**. Interpretation of data within this portion was carried out by M. J. S. Hill.

All other experiments within this chapter were carried out by M. J. S. Hill.

3.1 Introduction

Supramolecular gels are inherently dynamic materials due to their non-covalent and reversible underpinnings.[1] This is especially true for gels formed from low molecular weight gelators (LMWGs).[2] Within these materials, the gelation process drives the hierarchical self-assembly of these small organic molecules, leading to a dynamic molecular architecture.[2] This leads to a class of material that is responsive to external stimuli and highly sensitive to the conditions under which the self-assembly is carried out.[3-9]

Within these systems, different gelators form different gels, due to altering the molecular building blocks from which the macroscale material is created. Different gels can also be formed from the *same* gelator through changes in the preparation method or conditions of gelation, each with unique mechanical, or other, properties. [5, 9-15] Various groups have produced distinct materials starting from the same gelators, by employing different gelation triggers or even subtle variations within the same trigger.[6, 7, 10-12, 16-19] Usually this can be attributed to subtle differences in the underpinning solid-like self-assembled gelator network and the microstructure of fibrous aggregates within this network.[20-23] Both Huang et al. and Almohammed et al. demonstrated different microstructures of differing morphology, within gels formed from the same gelator within their respective systems, through altering the temperature during the gelation process.[16, 24, 25] Chen et al. and Dudukovic et al. both produced microstructures of differing morphology within solvent-switch triggered gels, through the use of different solvent ratios.[6, 17] These studies highlight how gelation within these gels is influenced by many variables.

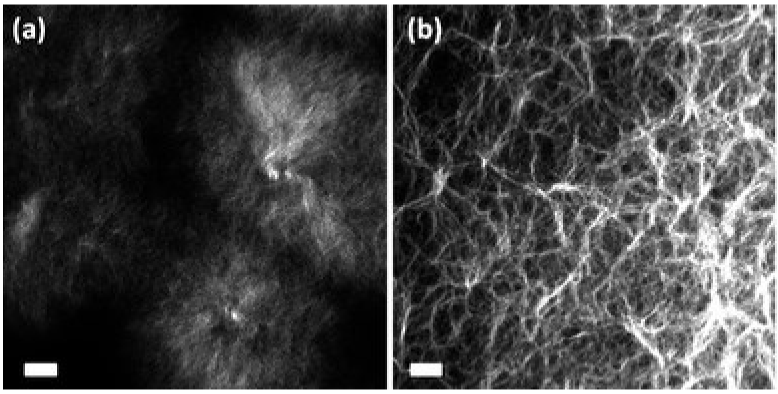

Figure 3.1 Confocal microscope images of gels formed at different volume fractions of DMSO in water at a constant final FmocLG concentration of 5 mg mL^{-1}. (a) Φ_{DMSO} 0.10; (b) 0.30. Scale bars represent 10 µm.[6] Figure is reproduced from ref.[6] with permission from the Royal Society of Chemistry.

The influence of varying vessel size has been studied in the context of protein aggregation and subsequently amyloid fibril formation but, to the best of our knowledge, the effect on the gelation of low molecular weight gels is largely unexplored.[26, 27] During gelation, gels usually take the shape of the vessel in which they are formed. As each potential characterisation technique requires a specific sample container, such as capillaries for scattering or NMR tubes,[28-30] the same gel being studied is made in various scales and shapes. For a uniform material, this would have no effect on the gels produced, but within the above studies it has been demonstrated that for some low molecular weight gels, this is not the case.[6] These gels possess a gelator network consisting of more compartmentalized building blocks, with spanning fibres linking these together, giving rise to a morphology that is non-uniform.[6] Changes in shape or scale would be expected to have an impact when forming these gels.

The fundamental aggregate building blocks from which these networks are built, spherulite-like domains, adopt a certain morphology and size when formed under specific gelation conditions.[6, 17]

Generally, the microscale domains from which supramolecular gels are composed are of little significance when testing bulk properties on macroscale samples. Gels samples are produced on scales that are orders of magnitude larger than that of the constituent domains. But with these materials being idealised for future applications within the biomedical field, e.g., as structural supports for tissue engineering or cell culture, low molecular weight gels of a similar or even smaller scale than these domains, may become necessary.[31, 32] At these scales, the domain size and morphology become significant. This leads to a need to better understand how these materials respond to imposed spatial constraints. Smaller domains may be adopted, like a plant’s growth being limited by the size of the pot it is grown in (Figure 3.2bii). Otherwise, incomplete, or partially formed spherulitic domains may be observed instead, with the fibrous aggregates continuing to grow to the same scale.

A better understanding of the response of these gels and their underpinning networks to imposed spatial constraints is crucial to guiding their use for the above biomedical applications or alternatively as candidates for model protocells.[33, 34] Here, these gels could be employed to mimic cellular membranes or intracellular matrices. The design and inherent limitations within these would be largely dictated by the gelator network and its subsequent morphology.

3.2 Results and Discussion

To explore the effect of imposed spatial constraints during formation of low molecular weight gels, two known LMWGs of the same family, 2NapFF and 2NapFV (Figure 3.2a), were selected.[35-37] Initially, these LMWGs were used to form the same volume of gel within different diameter ring-shaped vessels, giving separate gels of differing thickness. They were then used to form gels in dumbbell-shaped vessels (Figure 3.14). 2NapFF and 2NapFV were selected as they present slightly different microstructures, readily distinguished by confocal microscopy.[38] Completely distinct microstructures are presented by this class of low molecular weight gels when gelation is carried out via different triggers, e.g. solvent switching or pH.[6, 12, 35, 39, 40] The latter yields a uniform fibrous network, whilst the former gives a network consisting of spherulite-like domains, similar to those observed in organogels, under certain solvent ratios (Figure 3.2bi).[6, 16]

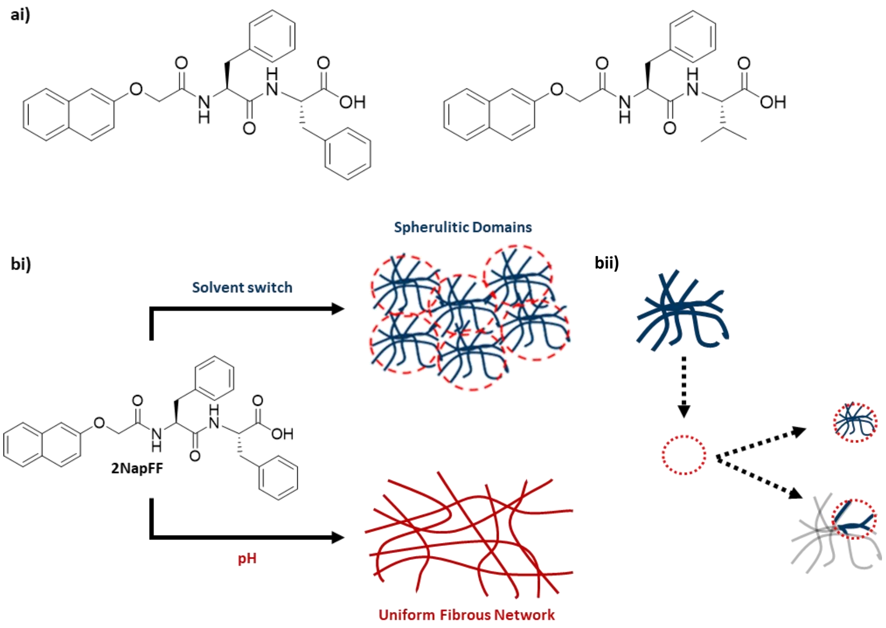

Figure 3.2 (a) Chemical structures of the dipeptide low molecular weight gelators (ai) 2NapFF and (aii) 2NapFV. (bi) Gelation pathways and resulting microstructures for 2NapFF gels formed via a solvent-switch or pH-trigger. A DMSO:H_2O solvent switch ($\phi_{DMSO} < 0.3$) can form a gel consisting of spherulitic domains whilst slow acidification via GdL (pH) forms a gel with a uniform fibrous network. (bii) Cartoon diagram demonstrating potential effect on spherulite growth by imposed spatial constraints during gelation.

To better understand the behaviour of these gels for potential biomedical applications, 2NapFF and 2NapFV gels were formed at different thickness and diameter via either a DMSO:H_2O solvent-switch or pH-trigger. These gels were characterised by confocal microscopy and cavitation rheology.[36, 37, 41-44] These two techniques allow for the observation of changes in microstructure and measurement of the localised mechanical properties respectively.[44] To enable this, 3D printed plastic rings, ranging from 7 to 21 mm in diameter, were adhered to glass microscope slides (Figure 3.13). The same volume of gel was used, creating gels of different diameter and thickness (Table 3.3). To ensure representative data, multiple measurements and images were taken within each gel sample, at different positions.

To be confident that vessel and gel size were responsible for observed difference in microstructure or mechanical properties, different 2NapFF gel volumes were made in the same diameter vessel (Figure 3.3). These produced gels of differing height that showed no significant differences in microstructure. This also helps to rule out varied surface contact with surfaces of different hydrophilicity, such as plastic and glass, as a significant contributing factor to observed differences in microstructure.[45]

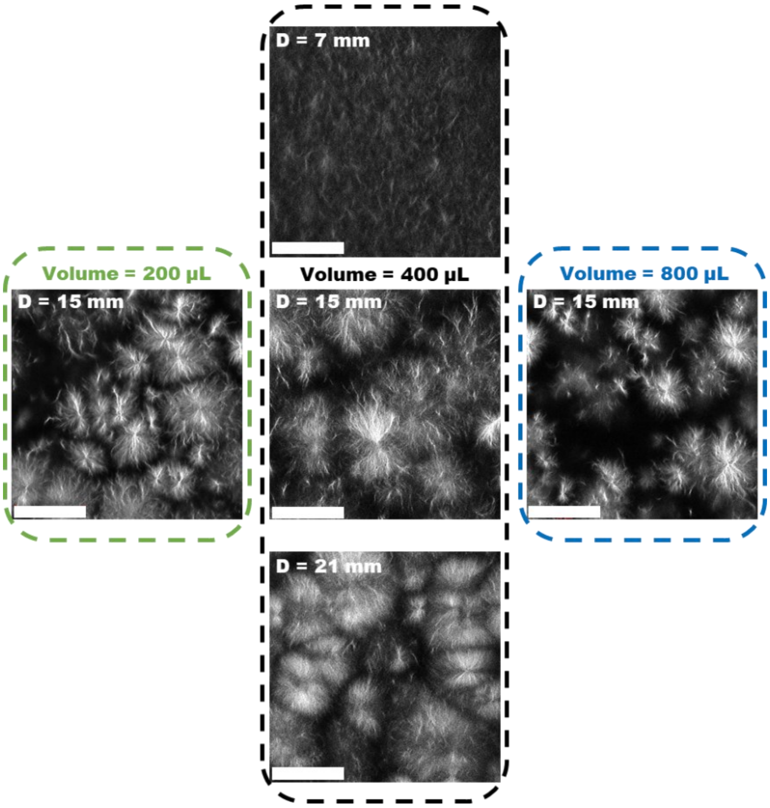

Figure 3.3 Confocal images of solvent-triggered 2NapFF gels prepared in 3D printed ring-shaped vessels with 7 mm (top), 15 mm (middle) and 21 mm (bottom) diameters. All gels were prepared at 5 mg mL^{-1} using a ϕ_{DMSO} = 0.2. Sample volume was varied between 200 µL (left), 400 µL (centre) and 800 µL (right) for gels formed in 15 mm diameter vessels to result in different height gels. Gels in 7 mm and 21 mm diameter vessels were formed at a volume of 400 µL. Nile Blue A dye was incorporated pre-gelation (0.1 wt% aqueous solution at 2 µL per mL of gel). Scale bars (white) represent 50 µm in all cases. D = vessel diameter. Images taken at a depth of 25 µm.

3.2.1 2NapFF

Confocal microscopy and cavitation rheology data of solvent-triggered 2NapFF gels were collected and processed by Ana María Fuentes-Caparrós (University of Glasgow). All other data collection and processing were carried out by Max Hill.

Initially, 2NapFF solvent-switch gels were selected to study, being a well-known LMWG with prior characterisation of its spherulite containing microstructure.[6, 37] Forming thicker gels would be expected to allow for further development of spherulite-like domains during the nucleation and growth phase separation process by providing more available space for growth.[6, 16] We used confocal microscopy to observe and show the morphological changes of these domains when 2NapFF gels were formed in different diameter vessels (Figure 3.4). Confocal microscopy was used preferentially to electron microscopies such as TEM or SEM. These higher resolution techniques provide information on the self-assembled structures instead of the overall microstructure. Also, SEM and TEM risk drying artefacts being observed instead of the true native environment due to sample processing.[46] Cryo-TEM, whilst being a better option for minimising drying effects, requires the sample to be in the form of a thin film (usually < 300 nm), making it unsuitable for this study.[47] Figure 3.4 shows the microstructure present in different thickness 2NapFF gels, with differences in the spherulite size observed.

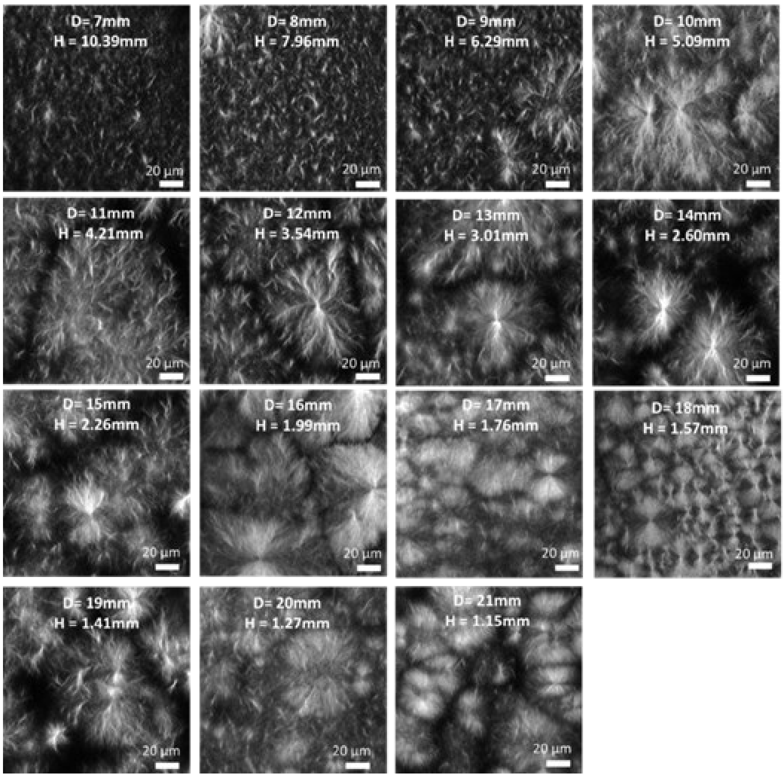

Figure 3.4 Confocal images of solvent-triggered 2NapFF gels prepared in 3D-printed ring-shaped vessels with different diameters. All gels were prepared at 5 mg mL^{-1} using a ϕ_{DMSO} = 0.2 and a total gel volume of 400 µL. Nile Blue A dye was incorporated pre-gelation (0.1 wt % aqueous solution at 2 µL per mL of gel). Scale bars (white) represent 20 µm in all cases. H = height and D = vessel diameter.

To quantify the observed spherulite sizes, ImageJ was used to measure observed perimeters of different spherulites (Table 3.1). An example of this is shown in Figure 3.5. For all imaging, multiple images were taken across each sample, in positions equidistant between the centre and edge of the gel. This was hoped to minimise edge effects and any artefacts from pipetting during gelation. Multiple repeated samples were imaged to verify observations (see Appendix B).

Table 3.1 Perimeter of the spherulitic domains within solvent-triggered 2NapFF gels of different thickness quantified using ImageJ. The deviation was calculated as the standard deviation in measured spherulite perimeters of five spherulites observed in at least two separate samples.

D (mm)	H (mm)	Perimeter (µm)	Deviation
7	10.39	173	13
8	7.96	129	19
9	6.29	284	133
10	5.09	799	167
11	4.21	1167	9
12	3.54	1045	158
13	3.01	828	107
14	2.60	780	148
15	2.26	610	47
16	1.99	766	63
17	1.76	493	36
18	1.57	354	48
19	1.41	604	74
20	1.27	815	137
21	1.15	598	149

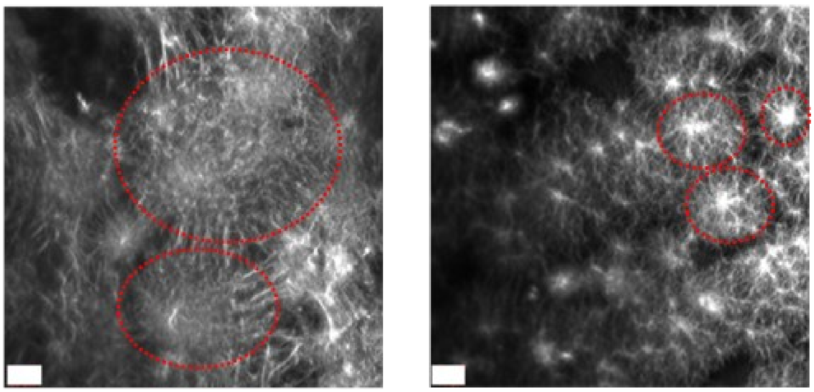

Figure 3.5 Exemplar marked up confocal microscopy images of solvent-triggered 2NapFV gels with examples of individual spherulites as used for quantifying perimeters highlighted (red). Scale bars (white) = 50 µm.

It can clearly be seen from Figures 3.3 and 3.4 that there are significant differences within the microstructure of 2NapFF gels upon changing the thickness. Across the vessel sizes studied, the size of the spherulites increases initially as the gels become thicker. This continues up until 5 mm, where the spherulite size starts to decrease. The size appears to plateau at a perimeter of around 200 µm (Figure 3.4).

The localised mechanical properties of the 2NapFF solvent-triggered gels were then probed via needle-induced cavitation rheology (Figure 3.6).[48] This microrheological technique characterises the localised mechanical properties of a material via the cavitation effect.[43, 44, 48] In short, a needle is inserted into a sample, connected to a system loaded with a fluid that is then pressurised and pumped through. This applies stress to the punctured material, eventually leading to the sudden growth of a cavitation bubble at the tip of the needle. The point at which the bubble cavitates and bursts is deemed the critical pressure (P_c). P_c values can be compared between materials when tested using a common method and even correlated to viscoelastic moduli determined through bulk oscillatory rheology.[43, 44] Bulk oscillatory rheology is typically the gold standard for characterising the viscoelastic properties of this class of material but has its limitations. It was unsuitable for this study due to the samples tested being inherently different preventing a standard testing protocol from being established and thus no effective comparisons could be made.

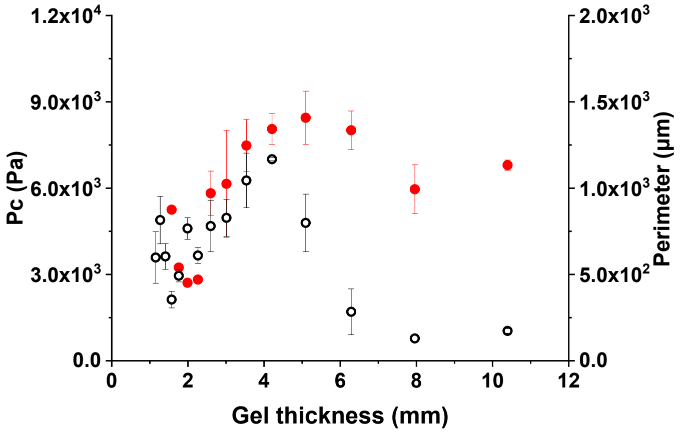

Figure 3.6 Correlation between the critical pressure (Pc) and spherulite perimeters within solvent-triggered 2NapFF gels of different thickness. The perimeter is represented with black hollow circles, and the critical pressure is represented with red circles. The error bars represent the standard deviations of three repeated measurements.

Figure 3.6 displays the correlation between spherulite perimeters and measured critical pressure values of solvent-triggered 2NapFF gels of differing thickness. Moving from thinner to thicker gels, P_c and spherulite perimeter generally increase up to gels around 4 mm thick. Here, both parameters drop upon moving to thicker gels, before appearing to eventually plateau as P_c and perimeter stay at similar values for the thickest gels measured. Within the thinnest gels, the lowest critical pressures may be due to an edge effect stemming from less gel being present to resist the growth of the cavitation bubble. The non-elastic glass bottom of the vessel impedes the growth of a cavitation bubble.

3.2.2 2NapFV

The above experiments were repeated using 2NapFV gels to see whether solvent-triggered gels of a similar but different gelator would show similar trends in microstructure and mechanical properties. When formed with a DMSO: H_2O solvent switch trigger, 2NapFV gels also present a spherulite-like microstructure at certain solvent ratios. As for 2NapFF, gels of varying thickness were formed in different diameter ring-shaped vessels and imaged via confocal microscopy (Figure 3.7). The average spherulite perimeter was measured and quantified with ImageJ (Table 3.2).

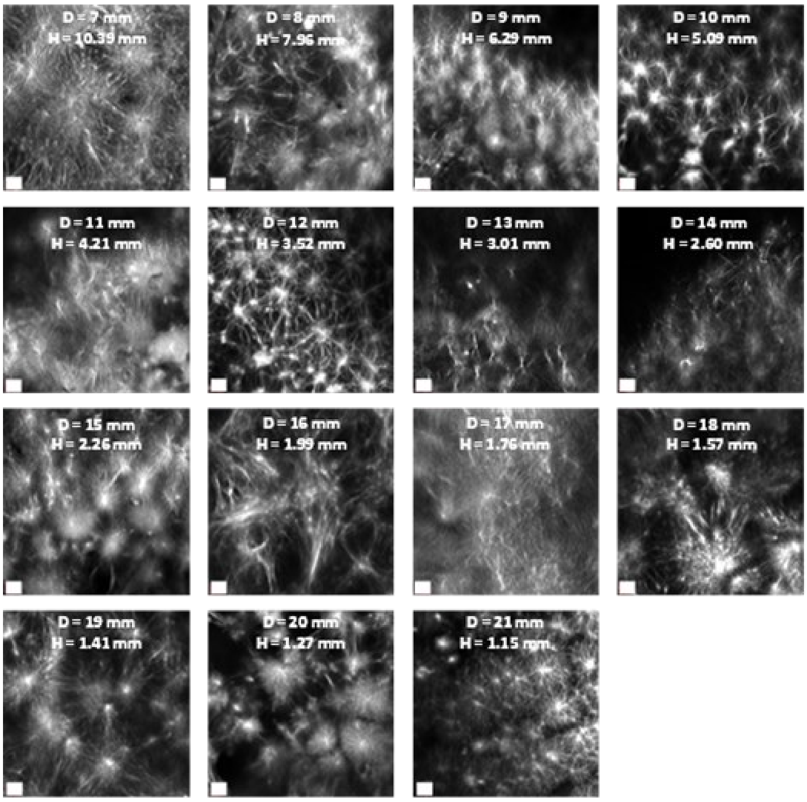

Figure 3.7 Confocal images of the solvent-triggered 2NapFV gels prepared in 3D-printed ring-shaped vessels with different diameters. All gels were prepared at 5 mg mL^{-1} using a ϕ_{DMSO} = 0.2 and a total gel volume of 400 µL. Nile blue A dye was incorporated pre-gelation (0.1 wt% aqueous solution at 2 µL per mL of gel). Scale bars (white) represent 50 µm. H = height and D = vessel diameter.

Table 3.2 Perimeter of the spherulitic domains within solvent-triggered 2NapFV gels of different thickness quantified using ImageJ. The deviation was calculated as the standard deviation in measured spherulite perimeters of five spherulites observed in at least two separate samples.

D (mm)	H (mm)	Perimeter (µm)	Deviation
7	10.39	1153	114
8	7.96	713	79
9	6.29	465	19
10	5.09	466	53
11	4.21	707	37
12	3.54	482	39
13	3.01	860	77
14	2.60	739	53
15	2.26	666	54
16	1.99	1301	126
17	1.76	1207	157
18	1.57	1469	55
19	1.41	1243	139
20	1.27	1103	165
21	1.15	1263	123

From Figure 3.7 the changes in morphology of the spherulite-like microstructure present within solvent-triggered 2NapFV gels can be seen. As gel thickness increases, spherulite size decreases, up until the 6 mm thick gels where it starts to increase again. This differs from the trend seen within the 2NapFF gels previously.

Figure 3.8 compares the measured critical pressures with the spherulite perimeters observed for DMSO:H_2O 2NapFV gels. Here, it appears there is an inverse relationship between the spherulite size and P_c values as the smallest spherulites correlate with the highest P_c and the largest spherulites are associated with the lowest P_c. Within the thinnest gels, the lowest critical pressures measured may stem from edge effects from proximity to the vessel bottom, as outlined earlier for 2NapFF. The thickest 2NapFV gels presented significantly larger spherulites than the same size 2NapFF gels.

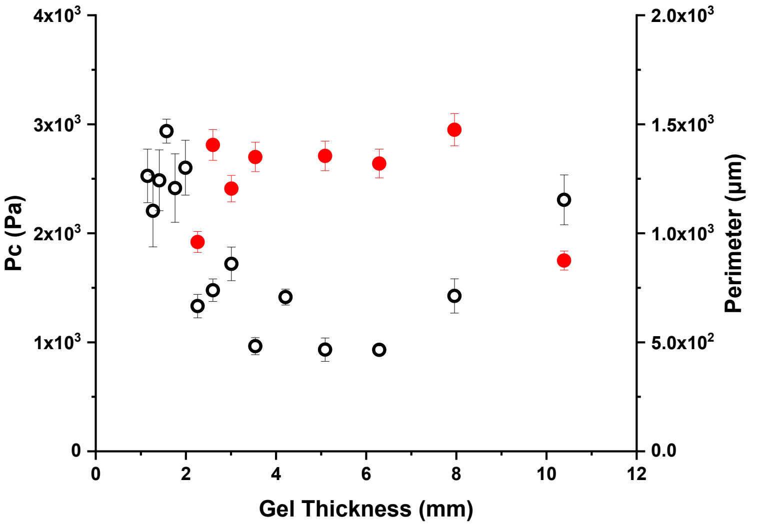

Figure 3.8 Correlation between the critical pressure (P_c) and spherulite perimeters measured within solvent-triggered 2NapFV gels of different thickness. The perimeter is represented with black hollow circles and the critical pressure with red circles. The error bars represent the standard deviation of three repeated measurements.

The spherulite-like domains constituting the microstructure of the 2NapFF and 2NapFV gels shown here are the product of a nucleation and growth phase separation process. Here, this network of aggregated fibres grow radially from dispersed droplets of aggregated LMWG solvated in the DMSO.[3, 6, 16, 49-51] A few of these nucleation centres continue to develop radially, consuming others through Ostwald ripening.[4] This process causes a microstructure that differs from the uniform fibrous network that is typical for low molecular weight, and other, gels.[1, 6, 50] This non-uniform network consists of densely populated radial aggregates of fibres, interconnected with adjacent clusters through fibres spanning the more sparsely populated space. Due to the nucleation and growth process and the subsequent radial propagation during gelation and the heterogenous network composition that this leads to, it is unsurprising that formation within a different environment leads to changes in the microstructure, just like a change within the gelation does.[5-8, 10, 11]

3.2.3 pH triggered gels

2NapFF and 2NapFV, as well as many other gelators within this family of LMWGs, can undergo gelation via a pH trigger.[2] Whilst this is possible with mineral acid, the current preferred method by many is through the slow acidification of the high pH LMWG solution by the hydrolysis of glucono-δ-lactone (GdL).[12, 52] This leads to more reproducible and homogenous gels, that contain a near uniform fibrous microstructure, due to gelation occurring over a significantly longer period of time than equivalent solvent-triggered systems.[12] pH-triggered 2NapFF and 2NapFV gels were formed in various diameter ring shaped vessels as above to see whether their response to imposed spatial constraints differs from that of their solvent-triggered counterparts.

Figure 3.9 presents the microstructure observed within GdL-triggered 2NapFF and 2NapFV gels in different diameter vessels. There are expected differences between the gelator networks within these two different gels with respect to fibre size and density, resulting from the respective self-assemblies of the two LMWGs. This is clearly seen, with 2NapFV fibres being thicker and less densely packed than those within the 2NapFF network (Figure 3.9b and a, respectively). However, there is little variation within each gel set, with fibre size and density remain largely consistent within each material, regardless of the size of the vessel in which they are formed.

The underlying networks of fibres become more populated, and thus progressively denser, over time once the sample pH has dropped below the gelators pK_a.[53] This process continues until gelation is complete. These fibres are produced through shape changes of micellar aggregates that become insoluble as pH drops below the pK_a. In contrast to the solvent-triggered gels nucleation and growth mechanism, this process is not diffusion limited due to the rate of pH decrease being slower than the diffusion rate of GdL. Therefore, the pH-triggered gels form consistently regardless of the space available during gelation, unlike their solvent based equivalents.

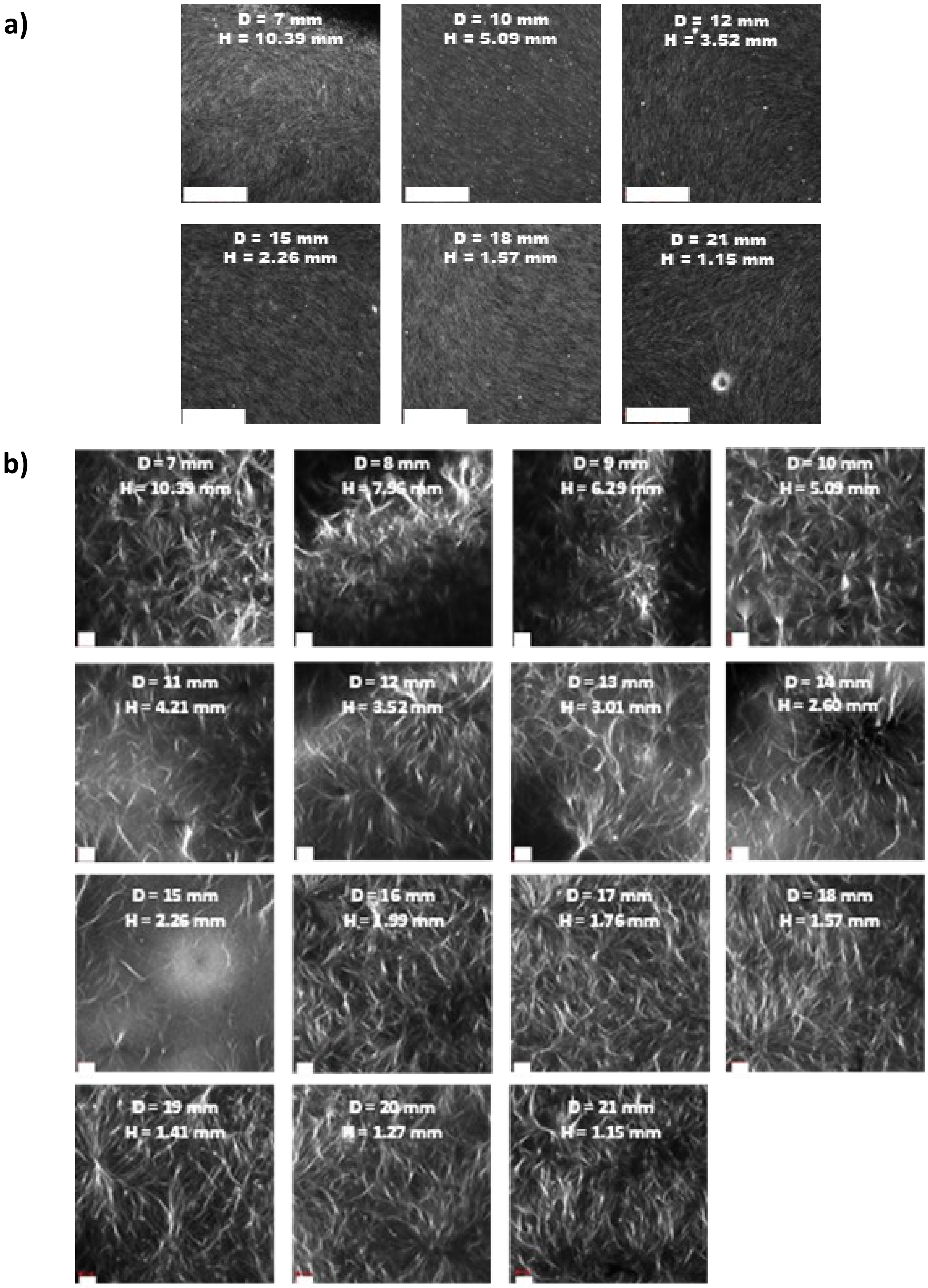

Figure 3.9 Confocal microscopy images of GdL-triggered (a) 2NapFF and (b) 2NapFV gels prepared in 3D printed ring-shaped vessels with different diameters. All gels were prepared at 5 mg mL^{-1} using 8 mg mL^{-1} GdL and a total gel volume of 400 µL. Nile blue A dye was incorporated pre-gelation (0.1 wt % aqueous solution at 2 µL per mL of gel). Scale bars (white) represent 50 µm. H = gel height and D = vessel diameter.

Cavitation rheology was used to determine critical pressures with different thickness 2NapFF and 2NapFV GdL-triggered gels (Figure 3.10). Due to the consistent observed microstructure present within each set of gels (Figure 3.9), similar P_c values were measured, with no significant variations in magnitude seen across either set of pH-triggered gels. P_c values for 2NapFF pH-triggered gels were consistently higher than those seen for 2NapFV. This may be due to the more densely packed networks seen within enabling them to further resist cavitation bubble growth, necessitating a higher pressure within the system. These observed pressure values support an independence of localised mechanical properties to scale of formation with these pH-triggered low molecular weight gels systems.

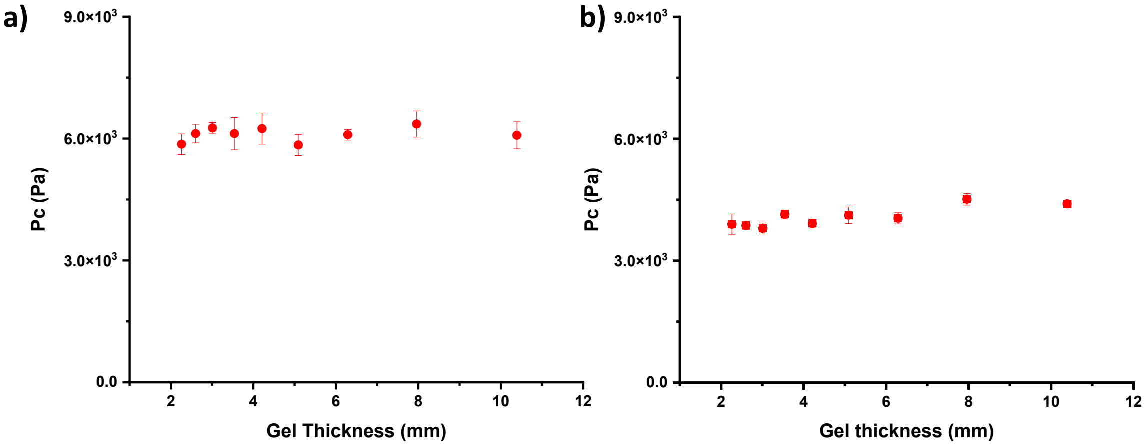

Figure 3.10 Measured critical pressures (P_c) of GdL-triggered (a) 2NapFF and (b) 2NapFV gels of differing thickness.

3.2.4 Multi-size vessels

To clearly highlight the effect of imposing spatial constraints on solvent-triggered gels, and their spherulite-like microstructure, vessels with regions of different width were used to form gels (Figure 3.11a). These were realised through a dumbbell or H shaped mould (Figure 3.14). Gels formed within these moulds would encounter different spatial constraints throughout the vessels. Confocal images of a 2NapFV gel within such a mould were collected (Figure 3.11). The gels within the wider ends of the mould displayed significantly larger, presumably more developed spherulite-like domains than that within the thinner connecting section. The spherulite-like domains found within the gel in the central section were smaller and more distinct, with less interconnecting links observed. These were reminiscent of the more distinct domains often seen within solvent-triggered 2NapFF gels (Figure 3.4).

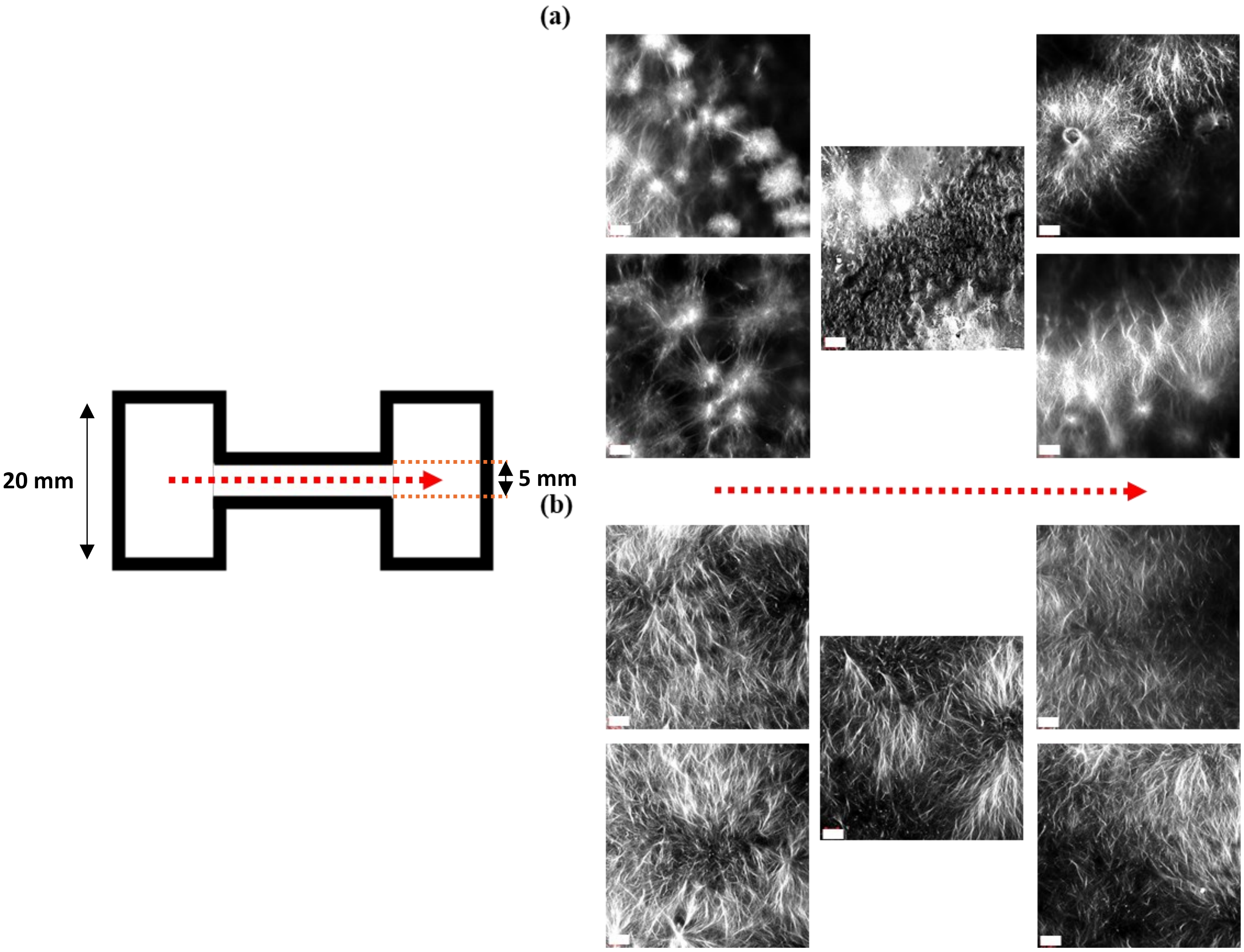

Figure 3.11 Confocal images of (a) solvent and (b) pH-triggered 2NapFV gels prepared in 3D printed dumbbell shape moulds (Figure 3.4.2). All solvent-triggered gels were prepared at 5 mg mL^{-1} using ϕ_{DMSO} = 0.2. All pH-triggered gels were prepared at 5 mg mL^{-1} using a GdL concentration of 8 mg mL^{-1}. Gel volumes were chosen to produce 2 mm tall gels. Nile blue A dye was incorporated pre-gelation (0.1 wt % aqueous solution at 2 µL per mL of gel). Scale bars (white) represent 50 µm. The direction of imaging is indicated with red arrows.

This experiment was then repeated with GdL-triggered 2NapFV gels, formed in the same vessels and imaged via confocal microscopy (Figure 3.11b). As expected from the previous observation within separate gels, the pH-triggered gel presented a consistent microstructure across the entire gel. Within both the wider end and thinner central portions of the gel, a uniform fibrous gelator network was present that displayed no clear differences in morphology across regions (Figure 3.11b). The microstructure seen here was also consistent with that seen in previous separately sized 2NapFV GdL gels (Figure 3.9b), reinforcing a lack of sensitivity to spatial constraints within these pH-triggered LMWG systems.

From the above and earlier results, we see a sensitivity to imposed spatial constraints in 2NapFF and 2NapFV gels when formed via a solvent-switch trigger, but not when formed via a pH trigger (Figure 3.12).

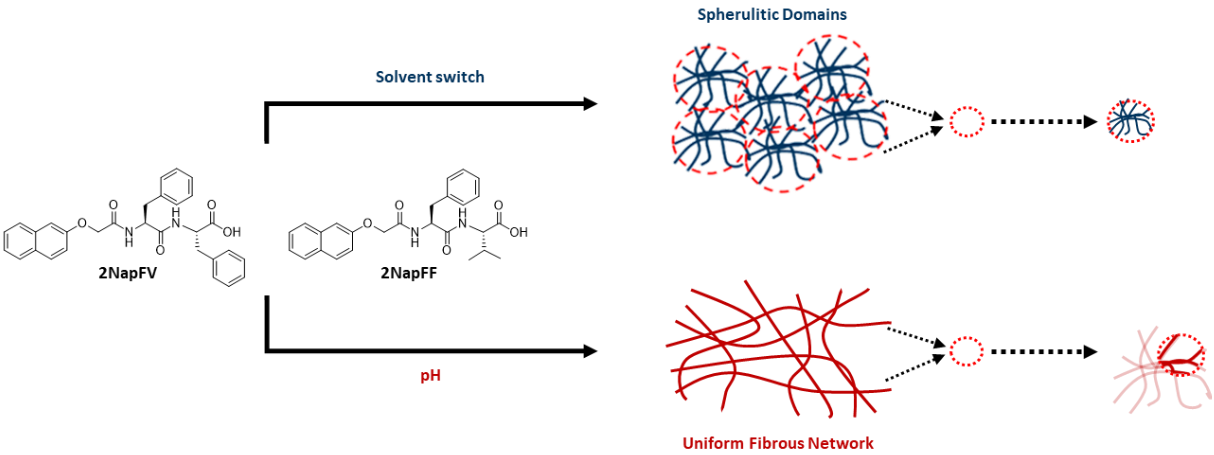

Figure 3.12 The response of 2NapFF and 2NapFV solvent and pH-triggered gels to imposed spatial constraints. The more compartmentalised network of the solvent-triggered gels shows differences in the size of its component spherulite-like domains (top), whilst the pH-triggered gel network remains consistent, regardless of the vessel (bottom).

3.3 Conclusion

The differences in morphological and mechanical properties observed within individual different scale solvent-triggered low molecular weight 2NapFF and 2NapFV gels indicates a sensitivity to spatial constraints within these specific materials. The size and morphology of individual domains that comprise the overall microstructure are influenced through simply altering the vessel size in which these gels are formed, as observed through confocal microscopy. These changes in spherulite size correlate with changes in localised mechanical properties measured by cavitation rheology.

The morphological and mechanical properties of pH-triggered equivalents of these low molecular weight gels were seen to be independent of spatial constraints. A consistent uniform fibrous microstructure is produced, regardless of the scale or shape of the vessel in which these pH-triggered gels are formed. This results in consistent localised mechanical properties measured across these samples.

The results above highlight yet another parameter which must carefully be controlled, or at least evaluated, when producing low molecular weight gels. It is evident that when working with solvent-triggered low molecular weight gels it is crucial to maintain consistency with respect to sample size and shape or, if unavoidable, acknowledge any potential influence differences in these may have for these materials. Clear observable differences in microstructure are shown and differences within the localised mechanical properties may be induced simply by formation of gels within different vessels. This data also gives confidence that for some systems, such as pH-triggered low molecular weight gels, these considerations are moot but preliminary evaluations to be certain of this are crucial. These observed sensitivities, or lack thereof, should help better inform the future characterisation and applications of these gels.

We hope that this study provides initial insight into a previously unexplored aspect of working with these materials, whilst also encouraging the further refinement of the considerations and methodologies used in their production. It is evident that the overarching statement of “everything matters”, unless explicitly proven otherwise, continues to be relevant to these materials.[2, 9]

3.4 Experimental

Materials:

2NapFF (F = phenylalanine) and 2NapFV (V = valine) were synthesized as described previously by Bart Dietrich, Dave Adams (University of Glasgow) and myself.[12] DMSO was purchased from Fisher Scientific and Nile Blue A was purchased from Sigma-Aldrich (Merck), with all used as received. Deionized water was used throughout.

Different sized vessels:

The same volume of gel (400 µL) was formed within ring-shaped vessels of different diameters, resulting in gels of different thickness. These vessels were created by 3D printing plastic rings of different diameters (from 7 to 21 mm) and adhering these to standard borosilicate glass microscope slides with Araldite two-part glue (Figure 3.13). This allowed for gels of varying thickness to be formed (ranging from 1 to 10 mm), as shown in Table 3.3. Gel thickness was calculated using the formula for the volume of a cylinder (Equation 3.1), where V = 400 µL, r = vessel radius and h = gel thickness.

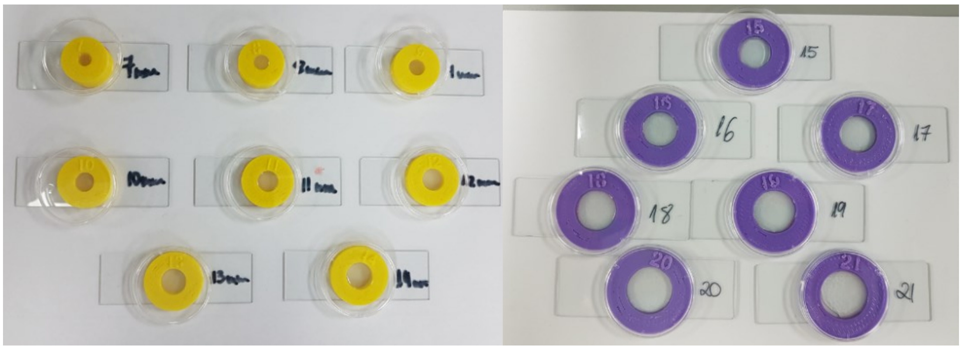

Figure 3.13 Photograph of the 3D printed ring-shaped vessels used to prepare gels of differing thickness. Ring diameter (mm) is labelled on each ring/slide and increases in 1 mm increments from 7 to 21 mm. Clear plastic lids from Greiner CellStar cell culture dishes were used as shown to reduce potential evaporation during gelation.

Table 3.3 Vessel Diameters and Corresponding Calculated Gel Thickness

Cavity diameter (mm)	Calculated gel thickness (mm)	Gel volume (µL)
7	10.39	400
8	7.96	400
9	6.29	400
10	5.09	400
11	4.21	400
12	3.54	400
13	3.01	400
14	2.60	400
15	2.26	400
16	1.99	400
17	1.76	400
18	1.57	400
19	1.41	400
20	1.27	400
21	1.15	400

Equation 3.1

$$V = \pi r^2 h$$

Non-uniform vessels:

To subject portions of a single gel to different spatial constraints, 3D printed dumbbell-shaped vessels were produced (Figure 3.14), with the shape below printed to form the walls of the vessel and then stuck to a glass microscope slide as for the rings (Figure 3.13).

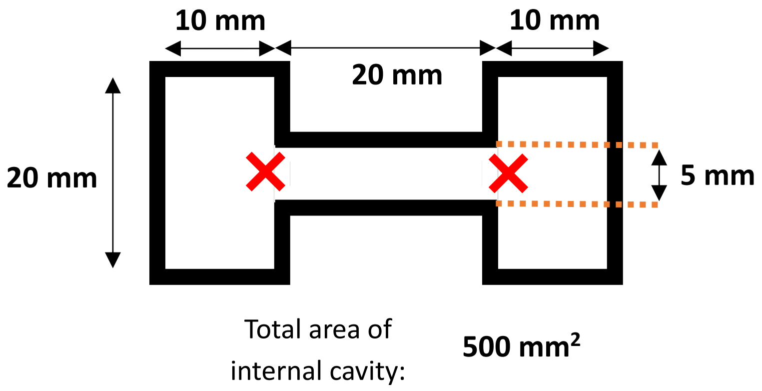

Figure 3.14 Schematic diagram of custom 3D printed gel moulds in a dumbbell shape. Dimensions are given in millimetres and represent those of the internal cavity in which gel was formed, not to scale. The positions from which water aliquots were pipetted in are highlighted with red crosses.

Forming gels of different thickness in ring-shaped vessels:

For the solvent-triggered gels, a gelator was dissolved in DMSO (25 mg mL^{-1}). 80 µL of this stock solution was pipetted into the desired ring-shaped vessel, with care taken to evenly cover the bottom of the vessel. 320 µL of water was then added via a 1 mL automatic pipet as a single aliquot to the centre of the vessel, forming a homogeneous low molecular weight gel (400 µL, 5 mg mL^{-1}) with ϕ_{DMSO} = 0.2 (Figure 3.15).

For the pH-triggered gels, a basic aqueous gelator solution was formed by the addition of gelator to water (5 mg mL^{-1}) and 1 molar equivalent of 0.1 M NaOH, before being left to stir overnight. This aqueous stock solution was then adjusted to pH 10.5 using aliquots of 0.1 M NaOH. A 400 µL portion of this aqueous stock solution was pipetted into a vial containing GdL (8 mg mL^{-1}), mixed thoroughly with a spatula for 5 s, and quickly transferred to the centre of the desired ring-shaped vessel to form a homogeneous gel (400 µL, 5 mg mL^{-1}). Samples were left to gel overnight within sealed Petri dishes containing wet tissue to prevent samples drying.

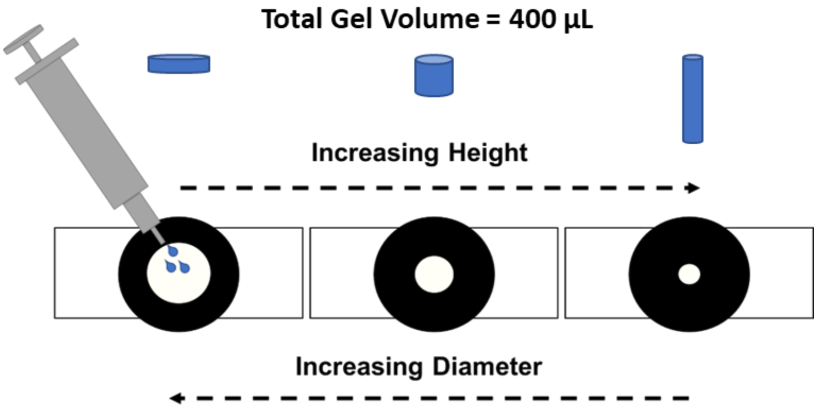

Figure 3.15 Cartoon of different thickness gels being formed within different diameter ring-shaped vessels.

Forming gels in non-uniform vessels:

As for the ring-shaped vessels, an aliquot of gelator stock solution in DMSO (25 mg mL^{-1}) was pipetted into the mould and spread evenly to give uniform coverage. This was then followed by an aliquot of water administered as two equal portions at different positions within the mould (Figure 3.14). This gave gels with a final gelator concentration of 5 mg mL^{-1}and ϕ_{DMSO} of 0.2. Gels were formed at volumes resulting in a final gel height of 2 mm in each mould.

For the pH-triggered gels, a basic aqueous gelator solution was formed by the addition of gelator to water (5 mg mL^{-1}) and 1 molar equivalent of 0.1 M NaOH, before being left to stir overnight. This stock solution was then adjusted to pH 10.5 using 0.1 M NaOH. An aliquot of this stock solution was transferred to a vial containing GdL (8 mg mL^{-1}), mixed thoroughly with a spatula for 5 seconds, and pipetted into the dumbbell-shaped mould. Samples were then left to gel overnight within sealed Petri dishes containing wet tissue to prevent samples drying. Gels were formed at volumes resulting in a final gel height of 2 mm in each mould.

Confocal microscopy

A Zeiss LSM 710 confocal microscope fitted with Zeiss N-Achroplan 10× and LD EC Epiplan NEUFLUAR 50× (0.55 DIC) objectives was used for confocal fluorescence microscopy imaging. Nile Blue A dye (0.1 wt % aqueous solution, 2 μL per mL of gel) was incorporated into gels to allow for imaging. The dye was added either dissolved within the water aliquot for the solvent-triggered gels or directly into the aqueous stock solution before GdL addition for the pH-triggered gels. Gels were prepared in custom ring-shaped vessels with glass microscope slide bottoms. Nile Blue fluorescence was achieved by excitation with a 634 nm He–Ne laser and emission detected between 650 and 710 nm. Multiple images were captured for each sample to ensure reproducibility. Images were taken at different points around the sample, equidistant from the centre and edge to minimise edge and pipetting effects. All images taken at a depth of 25 μm.

ImageJ analysis

ImageJ image processing software was used to quantify the perimeters of assigned spherulitic domains within gels. Generally, 5 different spherulites were chosen and measured across at least 2 images of each sample, with the perimeters analysed with ImageJ. Exemplified perimeter assignments for solvent-triggered 2NapFV are shown below. For microstructures presenting less distinct spherulites, domain boundaries were determined by eye as the point away from the densely populated centres where fibre density noticeably decreased to sparser spanning fibres, typically equidistant from the respective centres of the neighbouring domains (Figure 3.16).

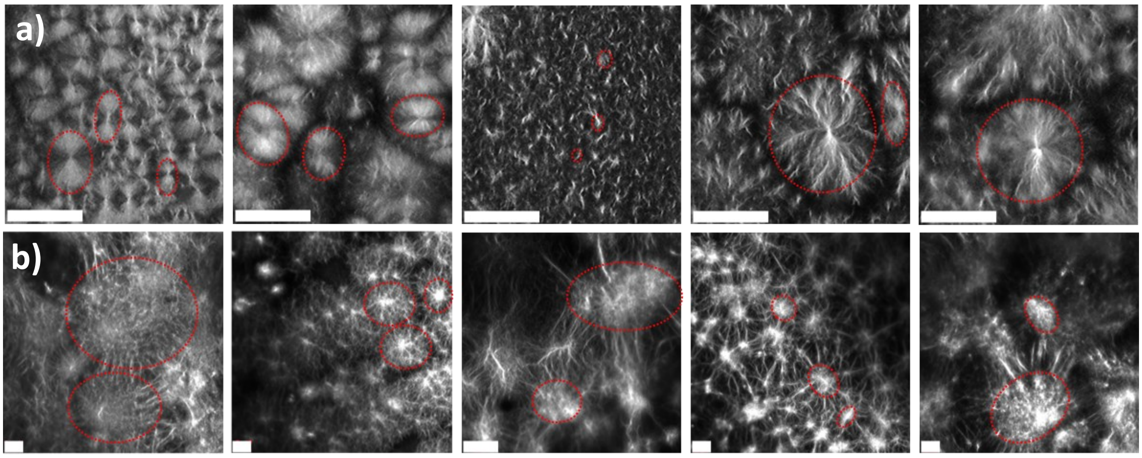

Figure 3.16 Exemplar marked up confocal microscopy images of solvent-triggered (a) 2NapFF and (b) 2NapFV gels with examples of individual spherulites highlighted (red). Scale bars (white) = 50 µm.

Cavitation rheology

A bespoke instrument produced in-house was used for cavitation rheology measurements as described previously (Figure 3.17).[43, 44] Air was pumped at a rate of 0.5 mL min^{-1} from a 10 mL Hamilton 1000 gastight syringe. For measurements, the tip of the needle (22 gauge) was set to a depth of 1 mm below the detected surface of the sample. The tip of the needle was positioned centrally in the sample. The critical pressure (Pc) was defined as the maximum pressure achieved within the system before the cavitation bubble formed with the sample burst, and the pressure subsequently fell. Measurements were performed on three separate samples prepared in triplicate.

Use of this technique is limited by a minimum gel thickness, at which reliable measurements can be achieved. A 1 mm working depth was used during the experiment, so very thin gels approaching this depth would not provide reproducible data due to edge effects. Here, growth of the cavitation bubble is disturbed or impeded by the proximity to the bottom of the container, making the observed Pc values unreliable. We found that the minimum gel thickness at which cavitation rheology could be reliably performed was 2.5 mm (corresponding to a 14 mm diameter vessel). Therefore, only gels thicker than 2.5 mm (vessel diameter $\leqslant$14 mm) could be analysed via cavitation rheology using our existing setup.[44] Edge effects were also expected to affect measurements taken close to the edge of the sample. Here, the solid walls of the vessel could interfere with or impede the growth of the cavitation bubble.

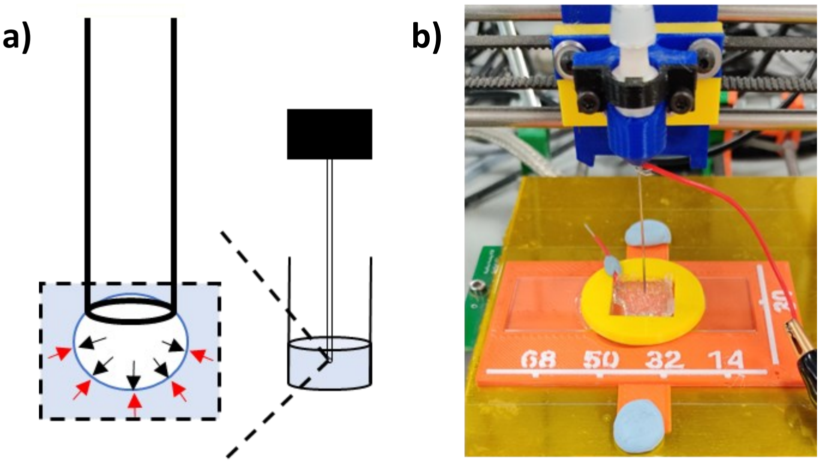

Figure 3.17 (a) Cartoon diagram of a cavitation bubble being formed within a gel via cavitation rheology. (b) Image of a 3D printed gel (see Chapter 2) being analysed by our cavitation rheology setup.[38, 44, 54]

3.5 References

1. J. W. Steed, *Chem. Comm*., 2011, **47**, 1379-1383.
2. E. R. Draper and D. J. Adams, *Chem*, 2017, **3**, 390-410.
3. M. Djabourov, *Polym. Int*., 1991, **25**, 135-143.
4. J. L. Andrews, E. Pearson, D. S. Yufit, J. W. Steed and K. Edkins, *Cryst. Growth Des*., 2018, **18**, 7690-7700.
5. J. Raeburn, A. Z. Cardoso and D. J. Adams, *Chem. Soc. Rev.*, 2013, **42**, 5143-5156.
6. L. Chen, J. Raeburn, S. Sutton, D. G. Spiller, J. Williams, J. S. Sharp, P. C. Griffiths, R. K. Heenan, S. M. King, A. Paul, S. Furzeland, D. Atkins and D. J. Adams, *Soft Matter*, 2011, **7**, 9721-9727.
7. J. Raeburn, G. Pont, L. Chen, Y. Cesbron, R. Lévy and D. J. Adams, *Soft Matter*, 2012, **8**, 1168-1174.
8. H. Wang, Z. Yang and D. J. Adams, *Mater. Today*, 2012, **15**, 500-507.
9. E. R. Draper and D. J. Adams, *Nat. Mater*., 2024, **23**, 13-15.
10. C. Colquhoun, E. R. Draper, R. Schweins, M. Marcello, D. Vadukul, L. C. Serpell and D. J. Adams, *Soft Matter*, 2017, **13**, 1914-1919.
11. J. Raeburn, C. Mendoza-Cuenca, B. N. Cattoz, M. A. Little, A. E. Terry, A. Z. Cardoso, P. C. Griffiths and D. J. Adams, *Soft Matter*, 2015, **11**, 927-935.
12. D. J. Adams, M. F. Butler, W. J. Frith, M. Kirkland, L. Mullen and P. Sanderson, *Soft Matter*, 2009, **5**, 1856-1862.
13. W. Helen, P. De Leonardis, R. V. Ulijn, J. Gough and N. Tirelli, *Soft Matter*, 2011, **7**, 1732-1740.
14. J. Smilek, S. Jarábková, T. Velcer and M. Pekař, *Polymers*, 2019, **11**, 927.
15. F. Tantakitti, J. Boekhoven, X. Wang, R. V. Kazantsev, T. Yu, J. Li, E. Zhuang, R. Zandi, J. H. Ortony, C. J. Newcomb, L. C. Palmer, G. S. Shekhawat, M. O. De La Cruz, G. C. Schatz and S. I. Stupp, *Nat. Mater*., 2016, **15**, 469-476.
16. X. Huang, S. R. Raghavan, P. Terech and R. G. Weiss, *J. Am. Chem. Soc.*, 2006, **128**, 15341-15352.
17. N. A. Dudukovic and C. F. Zukoski, *Langmuir*, 2014, **30**, 4493-4500.
18. N. A. Dudukovic and C. F. Zukoski, *Soft Matt*er, 2014, **10**, 7849-7856.
19. M. A. Greenfield, J. R. Hoffman, M. Olvera de la Cruz and S. I. Stupp, *Langmuir*, 2010, **26**, 3641-3647.
20. I. Heertje and F. S. M. Kleef, *Food Structure*, 1986, **5**, 91-98.
21. M. George and R. G. Weiss, *Acc. Chem. Res*., 2006, **39**, 489-497.
22. R. M. B. Prado, S. Mishra, H. Ahmad, W. R. Burghardt and S. Kundu, *Macromolecules*, 2021, **54**, 8946-8959.
23. P. Terech and R. G. Weiss, *Chem. Rev.*, 1997, **97**, 3133-3160.
24. V. A. Mallia, P. D. Butler, B. Sarkar, K. T. Holman and R. G. Weiss, *J. Am. Chem. Soc.*, 2011, **133**, 15045-15054.
25. S. Almohammed, M. B. Kanoun, S. Goumri‐Said, M. W. Alam, A. Fularz, A. Alnaim, J. H. Rice and B. J. Rodriguez, *Pept. Sci*., 2023, **115**, e24304.
26. W. Chen, Y. Yang, C. H. Lee and A. Q. Shen, *Langmuir*, 2008, **24**, 10432-10436.
27. J. Jayamani and G. Shanmugam, *Int. J. Biol. Macromol*., 2017, **101**, 290-298.
28. M. Wallace, D. J. Adams and J. A. Iggo, *Soft Matter*, 2013, **9**, 5483-5491.
29. E. R. Draper, B. Dietrich, K. McAulay, C. Brasnett, H. Abdizadeh, I. Patmanidis, S. J. Marrink, H. Su, H. Cui, R. Schweins, A. Seddon and D. J. Adams, *Matter*, 2020, **2**, 764-778.
30. D. McDowall, D. J. Adams and A. M. Seddon, *Soft Matter*, 2022, **18**, 1577-1590.

31. A. K. Das and P. K. Gavel, *Soft Matter*, 2020, **16**, 10065-10095.
32. S. R. Caliari and J. A. Burdick, *Nat. Methods*, 2016, **13**, 405-414.
33. R. Krishna Kumar, X. Yu, A. J. Patil, M. Li and S. Mann, *Angew. Chem. Int. Ed.*, 2011, **50**, 9343-9347.
34. A. S. Caldwell, B. A. Aguado and K. S. Anseth, *Adv. Funct. Mater*., 2020, **30**, 1907670.
35. L. Chen, S. Revel, K. Morris, L. C. Serpell and D. J. Adams, *Langmuir*, 2010, **26**, 13466-13471.
36. V. Jayawarna, M. Ali, T. A. Jowitt, A. F. Miller, A. Saiani, J. E. Gough and R. V. Ulijn, *Adv. Mater*., 2006, **18**, 611-614.
37. A. Mahler, M. Reches, M. Rechter, S. Cohen and E. Gazit, *Adv. Mater*., 2006, **18**, 1365-1370.
38. M. J. S. Hill and D. J. Adams, *Soft Matter*, 2022, **18**, 5960-5965.
39. C. Tang, A. M. Smith, R. F. Collins, R. V. Ulijn and A. Saiani, *Langmuir*, 2009, **25**, 9447-9453.
40. V. Jayawarna, S. M. Richardson, A. R. Hirst, N. W. Hodson, A. Saiani, J. E. Gough and R. V. Ulijn, *Acta Biomater*., 2009, **5**, 934-943.
41. M. P. Nikolova and M. S. Chavali, *Bioact. Mater*., 2019, **4**, 271-292.
42. T. Liebmann, S. Rydholm, V. Akpe and H. Brismar, *BMC Biotechnol*., 2007, **7**, 88.
43. J. A. Zimberlin, N. Sanabria-Delong, G. N. Tew and A. J. Crosby, *Soft Matter*, 2007, **3**, 763-767.
44. A. M. Fuentes-Caparrós, B. Dietrich, L. Thomson, C. Chauveau and D. J. Adams, *Soft Matter*, 2019, **15**, 6340-6347.
45. M. G. F. Angelerou, A. Sabri, R. Creasey, P. Angelerou, M. Marlow and M. Zelzer, *Chem. Comm.*, 2016, **52**, 4298-4300.
46. L. L. E. Mears, E. R. Draper, A. M. Castilla, H. Su, Zhuola, B. Dietrich, M. C. Nolan, G. N. Smith, J. Doutch, S. Rogers, R. Akhtar, H. Cui and D. J. Adams, *Biomacromolecules*, 2017, **18**, 3531-3540.
47. K. McAulay, H. Wang, A. M. Fuentes-Caparrós, L. Thomson, N. Khunti, N. Cowieson, H. Cui, A. Seddon and D. J. Adams, *Langmuir*, 2020, **36**, 8626-8631.
48. C. W. Barney, C. E. Dougan, K. R. McLeod, A. Kazemi-Moridani, Y. Zheng, Z. Ye, S. Tiwari, I. Sacligil, R. A. Riggleman, S. Cai, J.-H. Lee, S. R. Peyton, G. N. Tew and A. J. Crosby, *Proc. Nat. Acad. Sci*., 2020, **117**, 9157-9165.
49. J. M. Guenet, *Gels*, 2021, **7**, 65.
50. X. Huang, P. Terech, S. R. Raghavan and R. G. Weiss, *J. Am. Chem. Soc.*, 2005, **127**, 4336-4344.
51. R. Y. Wang, X. Y. Liu, J. Narayanan, J. Y. Xiong and J. L. Li, *J. Phys. Chem. B*, 2006, **110**, 25797-25802.
52. Y. Pocker and E. Green, *J. Am. Chem. Soc.*, 1973, **95**, 113-119.
53. L. Chen, K. Morris, A. Laybourn, D. Elias, M. R. Hicks, A. Rodger, L. Serpell and D. J. Adams, *Langmuir*, 2010, **26**, 5232-5242.
54. M. C. Nolan, A. M. Fuentes Caparrós, B. Dietrich, M. Barrow, E. R. Cross, M. Bleuel, S. M. King and D. J. Adams, *Soft Matter*, 2017, **13**, 8426-8432.

Chapter 4

Probing the Gel-Air Interface in Low Molecular Weight Gels

Chapter 4 – Probing the Gel-Air Interface in Low Molecular Weight Gels

Puncture tests water controls were carried out by **Jennifer Quigley** (University of Massachusetts, Amherst (UMass)). Nanoindentation data was collected by **Dr Dipankar Ghosh.** Interpretation of these data sets was carried out by **M. J. S. Hill**.

All other experiments were carried out by **M. J. S. Hill**.

Gel puncture experiments were carried out at the University of Massachusetts, Amherst on a research visit to, or subsequent collaboration with, the group of **Professor Al Crosby**.

Dr Ben Russel & Dr Chris Syme (University of Glasgow) provided technical support with the departmental confocal microscope during this time.

4.1 Introduction

Due to their reversible non-covalent underpinnings, supramolecular hydrogels can be influenced by a wide range of factors during their formation.[1-8] Many different properties can be produced from the same or different gels stemming from the same gelator, for example by using a solvent-switch or pH trigger.[6, 9-15] Typically these bulk properties can be linked to directly observable differences within the underlying gelator network and its adopted microstructure.[6, 14, 16, 17] One feature that has been relatively unexplored is the network morphology at the surface of a gel. Here, the phase interface with air might be expected to have a different influence on the network assembly than would be incurred at the other boundaries with the container walls. Similar effects have been studied in gels formed as thin-films, where the significantly greater surface area and interface would be expected to play a much larger role towards influencing the properties of these materials.[18-20] Whilst expecting a lower contribution of this surface to occur within bulk gels upon moving away from thin-film applications as this area becomes a much smaller fraction of the bulk material, the surface's influence may still hold relevant for certain applications.

For biomedical applications that use these supramolecular hydrogels as suitable models for cells and tissue,[21, 22] understanding the puncture of these gel surfaces is highly relevant.[23, 24] These materials are also hoped to become advanced 3D cell culture supports.[25-27] In this role, cells would grow into the gel support. For systems in which the cells are introduced on the top surface of the gel this would require the gel surface to be well understood to be better able to predict and enable cell growth that can penetrate the supporting material effectively.

Some 3D printed gel systems print into a pre-existing gel support matrix, similar to some of the gelation inducing support baths described earlier.[28-30] Here, effective printing may be enabled by a well understood soft surface that must be punctured to deliver printed substrate.

Finally, needle-induced cavitation rheology, a technique with wide-ranging scope within the soft materials field, necessitates the successful puncture of the tested material with a needle for measurements. [24, 31, 32] A current lack of standardised testing protocols within the field typically results in measurements taken using a methodology developed in-house.[31-33] For the successful development and iteration of these procedures, or pioneering of new protocols, an appreciation of gel surface properties is crucial.[24, 32]

4.2 Results and Discussion

The previous chapter demonstrated how gels of 2NapFF and related LMWGs can be sensitive to changes in the vessel in which they are formed depending on the gelation trigger used.[34] The importance of cavitation rheology as a means to probe this system was highlighted. This analytical technique holds great promise within the characterisation of low molecular weight gels, but to date its use in the field is still rarely reported.[35] Whether this is a result of typically less reproducible data compared to oscillatory rheology or a lack of rugged supporting theoretical models specifically relevant to this class of materials is unclear.[31] Most studies into the underlying mechanics and attempts to link this to appropriate theoretical and subsequent computational models of this technique have largely been limited to covalent polymer gels.[31, 36-39] This is perhaps unsurprising due to their typically more reproducible mechanical properties,[40] higher strength and easier to model underlying networks as compared to many low molecular weight gels.[41-44] Indeed even the definitions of cavitation and fracture, the two main failure mechanisms observed within soft materials during cavitation rheology, are tied to the manner in which a model end-linked network is affected.[36, 45-48] It is therefore clear that further efforts are needed towards better understanding of the application of cavitation rheology within different low molecular weight gel systems.

To this end, a logical initial step was to explore the different behaviours of 2NapFF solvent and pH triggered gels when subject to cavitation rheology. The starkly different microstructures present would be expected to favour different failure mechanisms due to the more compartmentalised gelator network of the solvent triggered gels and largely uniform network of the pH triggered gels. 2NapFF was initially chosen as a well-reported LMWG that multiple gelation triggers can be applied to produce different gels.[9] A sensible starting point to better understand cavitation rheology and thus applying needle-induced cavitation within these gels was to explore the puncture behaviour during needle penetration of the gel.[24]

4.2.1 Gel puncture

Initial puncture data of 2NapFF solvent and pH triggered gels (Figure 4.1) were collected, collated, processed, and interpreted by Max Hill personally on a research visit to the University of Massachusetts (UMass). Processing and interpretation of this data was carried out by Max Hill.

2NapFF gels were formed via a DMSO:H_2O solvent-switch or GdL pH trigger as 6 mL samples within vials for puncture studies using a range of different diameter flat-tipped hollow-bore needles (⌀ = 0.7, 0.5, 0.4, 0.3, 0.2 mm). Gels were produced at these volumes to facilitate adequate depth of travel to allow for a 20 mm puncture test to be conducted. Puncture tests with a 20 mm puncture and retraction protocol were carried out (Figure 4.1).

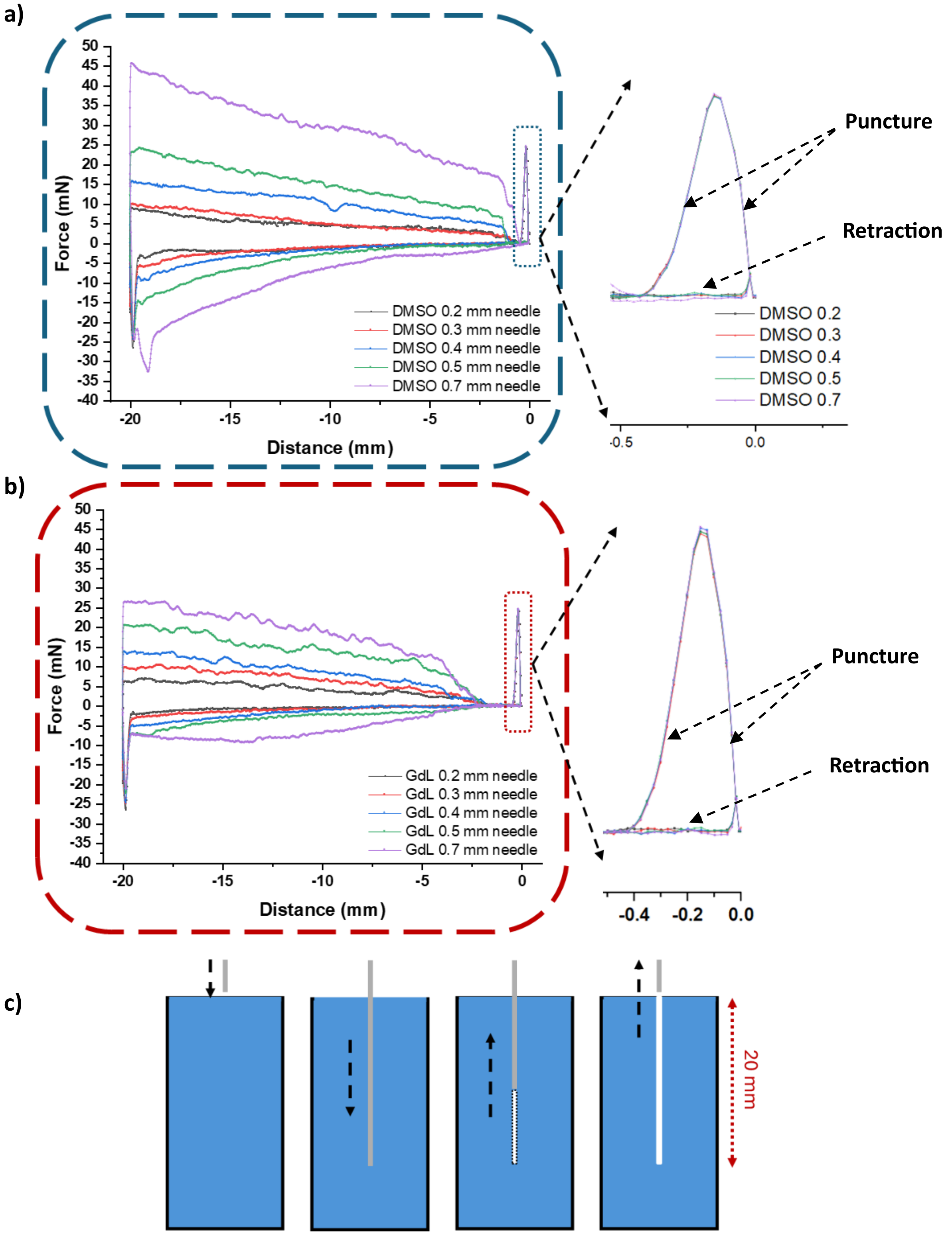

Figure 4.1 Force distance profiles from the puncture of 2NapFF (a) solvent and (b) pH triggered gels by hollow-bore flat-tipped needles with ⌀ = 0.7, 0.5, 0.4, 0.3, 0.2 mm. Tests were started with the needle positioned just above the gel surface, with a puncture and retraction of 20 mm at a speed of 5 mm s^{-1}. Initial force peaks are highlighted and magnified. c) Cartoon schematic showing the needle puncture and retraction in a gel sample (blue).

From Figure 4.1 we see that there is a general similar trend seen in the 2NapFF DMSO:H_2O solvent and GdL pH triggered gels. As needle diameter increases, so too does the force generated during puncture (0 to -20 mm). This would be expected due to the larger needle creating a larger hole within the gel as it passes through, shifting more material out of its path, thus resulting in a greater measured force. Within the pH triggered gels, the forces observed increase consistently with increasing needle diameter (Figure 4.1b). For the solvent triggered gels, the force generated with the 0.2 and 0.3 mm needles are very similar, with equal increases in force then seen between 0.3, 0.4 and 0.5 mm needles (Figure 4.1a). Then, upon moving up to the largest diameter needle, there is a larger increase in force observed, matching more closely with the bigger difference in diameter between the largest two needles. For the lower two needle sizes, the internal bore diameter may be of a similar size to or even slightly smaller than some of the larger spherulitic domains observed with solvent triggered 2NapFF gels. This could mean that spherulites within the network are shifted aside rather than destroyed or plugging the needle, leading to lower resistance than for larger needles. The more uniform fibrous pH triggered network is unable to rearrange in this manner, instead having to break fibres to accommodate the needles travel for all needle diameters.

From the initial data, something interesting appears to arise. A sharp non-insignificant peak in measured force was consistently seen at an indentation distance of around 0.15 mm. Within both datasets the peak was seen for every run with each of the different diameter needles, falling at the same needle depth. The consistent identical nature of the peak seen throughout both experimental data sets caused suspicion of a systematic experimental error, likely manifesting as an instrument operational artefact. However, due to time constraints, control experiments had to be carried out a later point.

Whilst waiting for control experiments to be carried out to verify the validity of these initial peaks, attempts to rationalise them were explored. Despite not being a perfectly representative system, similar peaks are seen within the indentation/puncture profile of a model polymer gel (Figure 4.2).[24]

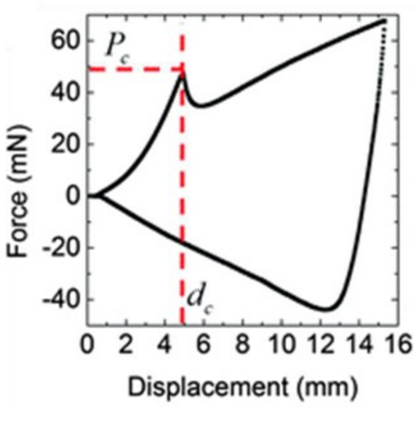

Figure 4.2 Force displacement profile of a model acrylic triblock copolymer gels (PMMA, PnBA, $A_{25}B_{116}A_{25}$). Figure is reproduced from ref.*[24]* with permission from the Royal Society of Chemistry.

Here, the initial peak is defined as the critical depth, d_C, which is the puncture force and depth associated with the indenter breaking through the top surface of the tested material. Whilst not a perfect model for our system due to the significantly increased elasticity of the polymer gels used, the results may give some insight as to the nature of the unexpected peak for the 2NapFF gels. This peak may have represented puncture of the surface of these low molecular weight gels and would be in line with the relatively brittle nature that is seen in some examples of these gels.

The different gels show different force responses after these initial events. The solvent triggered gels almost immediately start to increase in force again, whilst there is a delay seen within the pH triggered gels. This could be explained by the different microstructure observed between the two. The more uniform network within the pH triggered gels may facilitate a crack propagating from the initial fracture event, meaning the needle is encountering minimal resistance for the first few millimetres. Then once the needle tip eventually reaches the end of this initial crack, the force begins to increase once more as gel is broken again. The more compartmentalised microstructure of the solvent triggered gels may prevent the initial fault propagating much beyond the surface of the gel as the domains can more easily rearrange and accommodate the network failure. New spanning links within the network must therefore be broken much closer to the original surface puncture than in the pH triggered gels, so forces generated start to increase again almost immediately.

Upon retraction, both systems show an instantaneous shift to negative force values, indicating the gels pulling on the needles as they are removed. Again, differences in behaviour are seen between the two systems. Within the pH triggered gels, an almost immediate sudden release of tension is observed, falling to a near zero reading in most cases. On the other hand, the solvent triggered gels show more gradual decay in the tension, more closely resembling the retraction profile seen above for the model polymer gels (Figure 4.2). The more uniform network of the pH triggered gels would be expected to show reduced self-healing of the network from fracture than the more compartmentalised solvent triggered gel network, due to fewer interconnecting links needing to reform in the latter for the network to effectively recover. For the pH triggered gels the needle retracts largely unhindered through the channel created during puncture but has to further disrupt the network that has started to recover around it within the solvent triggered gels.

As a result of these data, efforts were turned towards further exploring the unexpected initial peaks within the force-distance profiles of both types of 2NapFF gel by confocal microscopy, rheology and nanoindentation.

Subsequent puncture data for water control tests shown in Figure 4.3 were collected and collated by Jennifer Quigley, UMass. Processing and interpretation of this data was carried out by Max Hill. Puncture speed tests shown in Figure 4.4 were carried out by Max Hill personally on the research visit to UMass. Control tests were only able to be carried out a few months after collection of initial data due to time constraints. Confocal microscopy, rheology and nanoindentation tests were carried out during this delay.

Water needle puncture tests were later run as control experiments to attempt to verify the unexpected potential surface puncture peaks seen earlier within the 2NapFF gels (Figure 4.1). The same puncture protocol of 20 mm indentation and retraction was repeated (Figure 4.3), with the same volume of water as gel used previously.

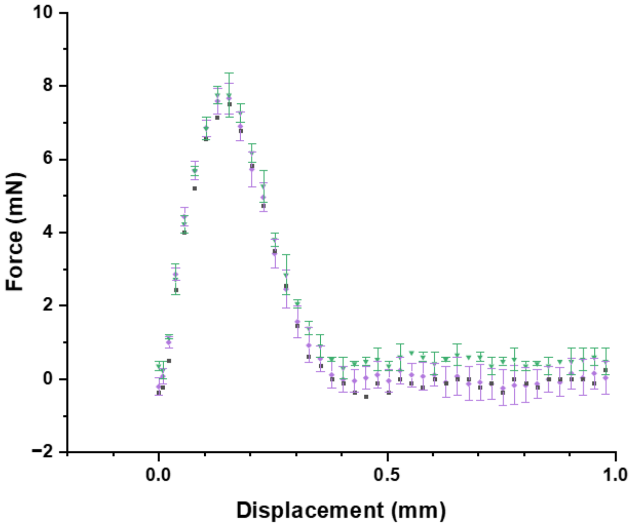

Figure 4.3 Force displacement profiles from the puncture of water by hollow-bore flat-tipped needles with ⌀ = 0.7 (purple diamonds), 0.5 (green triangles), 0.2 mm (grey squares). Tests were started with the needle positioned just above the gel surface, with a puncture of 20 mm at a speed of 5 mm s^{-1}.

When water is tested, Figure 4.3 clearly also shows an initial force peak at a depth of around 0.15mm after which the force falls back to near 0 mN, as was seen earlier for 2NapFF gels. This discredits the initial force peaks observed in part 4.2.1 and shows that they are not indicative of puncture of the gel surface, instead a systematic error from the experimental procedure. Given the very similar nature of the peaks seen, it was suspected to be an instrument artefact, likely caused by an excessively high indentation and retraction rate. This was confirmed from data collected earlier as part of an initial test into the effect of different puncture speeds on 2NapFF solvent and pH-triggered gels (Figure 4.4)

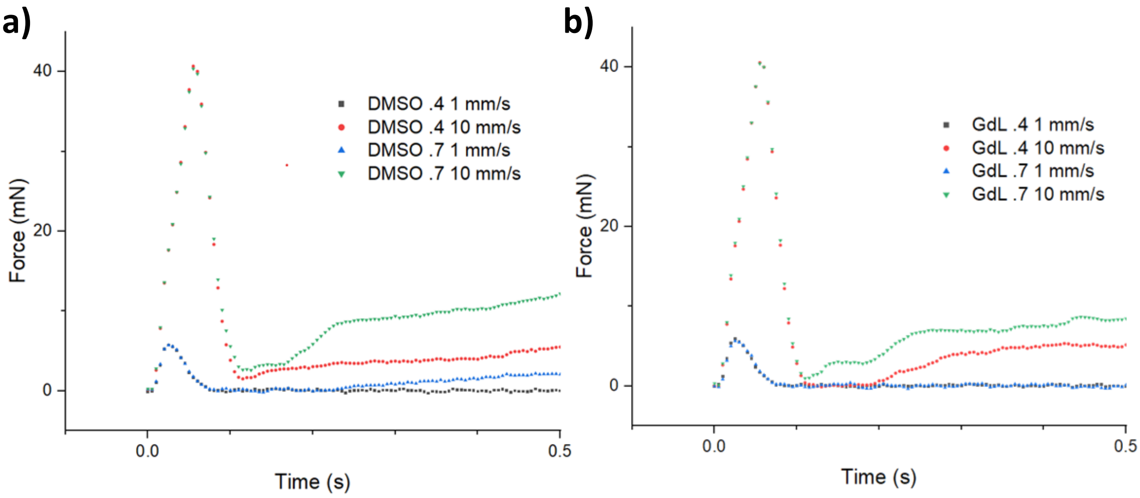

Figure 4.4 Initial force-time profiles from the puncture of 2NapFF (a) solvent and (b) pH triggered gels by hollow-bore flat-tipped needles with ⌀ = 0.7 and 0.4 at indentation rates of either 1 or 10 mm s^{-1}. Tests were started with the needle positioned just above the gel surface.

The initial force peak within both gel systems is smaller for the lower indentation and retraction rate of 1 mm s^{-1} compared to a rate of 10 mm s^{-1}, strongly indicating an instrument operational artefact.

This outcome was only confirmed at the end of the experimental time and whilst waiting for the data from our collaborators, we had carried out a number of key follow up experiments in an effort to understand whether the observed peak was due to differences in the gel at the surface. Since these led to interesting observations despite the observed peak turning out to be artefactual, the data from these experiments are discussed below.

4.2.2 Confocal microscopy

If a crust were formed at the air-gel interface, differences in the microstructure of the gelator, such as fibre density or pore size, might be observable through a suitable network scale imaging technique like confocal microscopy. Initial experiments involved collecting Z-stacks of 2NapFF solvent triggered gels (Figure 4.5). The microstructure of the gelator network within these gels was predicted to allow for easier visualisation of changes in morphology at the gel surface. It was hoped that images could be captured deep enough into the gel to effectively probe any network differences at the surface.

The images within Figure 4.5a indicate that there may be some morphological difference at the gel surface but is hard to be certain that it is not simply artefacts arising from an out of focus sample. After the initial focussed frame (Figure 4.5av), there appears to be little observable difference. The image set within Figure 4.5b was then collected spanning a smaller distance, with reduced intervals between images. This provided stronger evidence for a difference within the network at the surface, with seemingly more densely packed individual domains seen in Figures 4.5bii and 4.5biii than the rest of the image set.

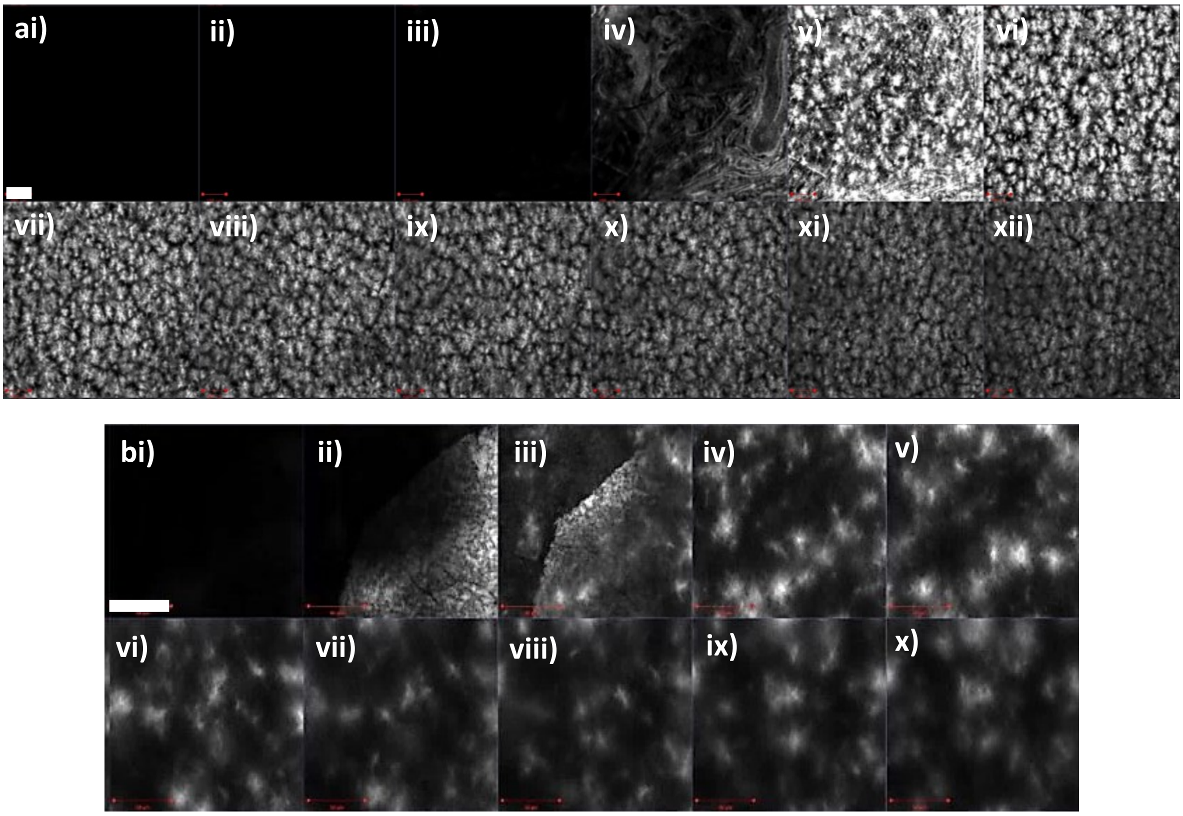

Figure 4.5 Confocal microscope Z-stacks of 2NapFF solvent triggered gels (5 mg mL^{-1}, DMSO: H_2O, 20%) formed and imaged within cut down Sterilin 7 mL vials. Nile blue A dye (2 µl of a 0.1 wt% aqueous solution per mL of gel) was incorporated into sample to be imaged. (a) is from a 3 mm stack taken at 50 µm intervals, cut down to the first 12 relevant images. Scale bar (white) = 100 µm. (b) is from a 0.7 mm stack taken at 10 µm intervals, cut down to the first 10 relevant images. Scale bar (white) = 50 µm. Imaging was started above the surface of the gel, with the focus being shifted down through the sample (i→ii→iii).

To improve upon this, an alternate imaging method was adopted (Figure 4.6). Gels were formed within syringes to produce hockey puck shaped samples. These were cut to produce a cross section of the gel and manipulated to lay flat. In this manner, sequential confocal images could then be taken across this cross section in the microscopes standard imaging plane that would translate to the original samples vertical (Z) axis. In this way, sets of images could be collected akin to collecting a Z-stack of images, but with a much greater sample depth.

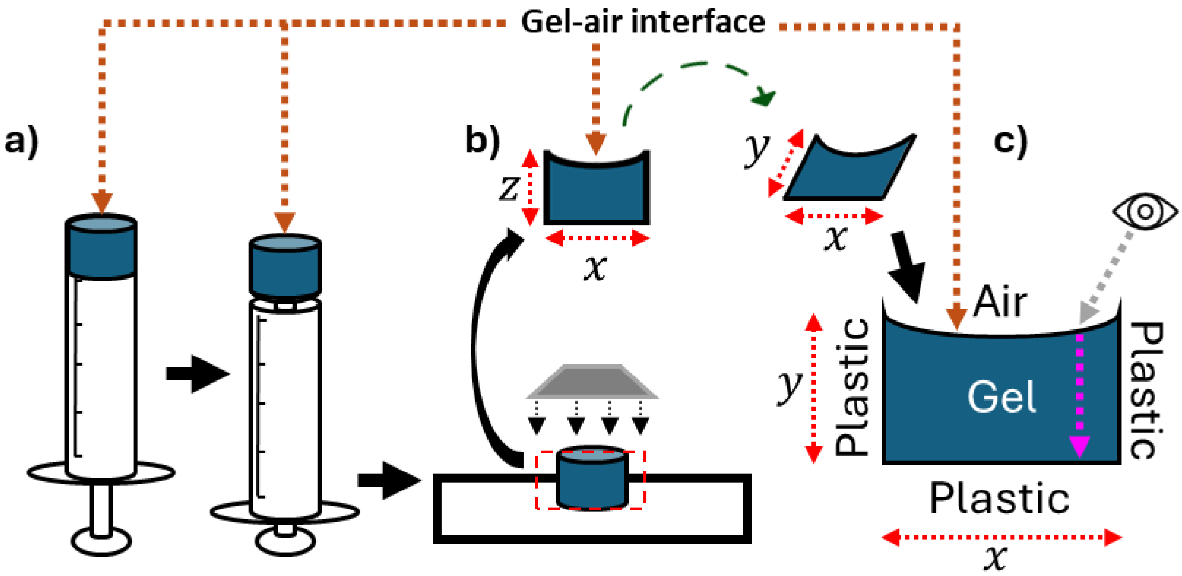

Figure 4.6 Schematic diagram of a) gel pucks formed in syringes, b) cutting a cross section for imaging and c) rotating this to enable confocal microscope imaging along what was originally the gels Z plane. Images where typically taken from the original air-gel interface into the bulk gel and towards/ through to the original gel-plastic interface (violet dashed arrow). Processing samples in this way allows a manual set of sequential images to be taken from the air-gel interface into the bulk of the gel, akin to a Z-stack.

Through this method, it was possible to reliably image the microstructure of the gelator network right at the air-gel interface (Figure 4.6c). This was first trialled with 2NapFF solvent triggered gels (Figure 4.7).

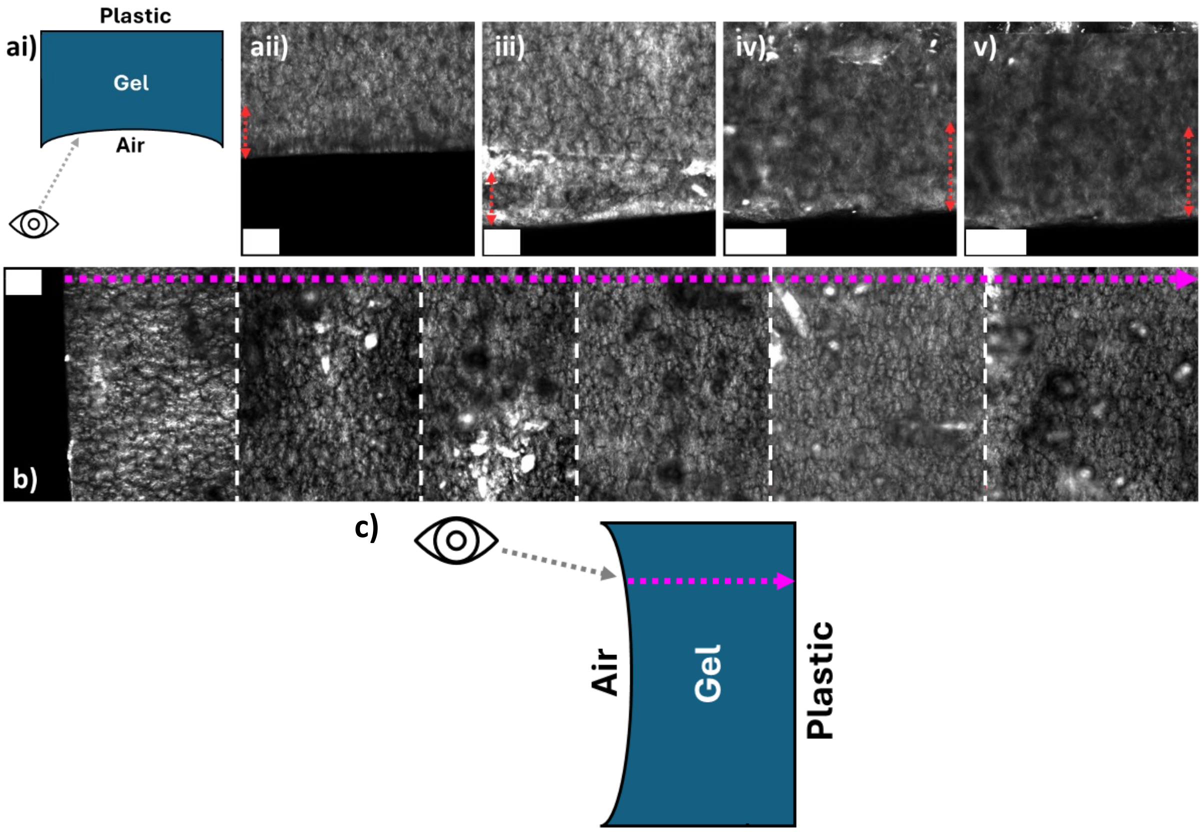

Figure 4.7 Confocal microscope images of 2NapFF solvent triggered gel cross sections (5 mg mL^{-1}, DMSO: H_2O, 20%). Nile blue A dye (2 µl of a 0.1 wt% aqueous solution per mL of gel) was incorporated into imaged gels. Scale bars (white) = 100 µm. (a) The gelator network present at the air-gel interface within separate 2NapFF gel samples (aii – av) along with cartoon schematic to show area imaged (ai). Red dashed arrows that correspond to 150 µm in length have been added. (b) A combined set of images of the gelator network within a single gel from the air-gel interface (left) through to the bulk gel (right). Individual images are highlighted with white dashed lines. c) A cartoon schematic showing how sequential confocal images were taken across a sliced and rotated gel sample. The pink dashed arrow represents the direction of imaging.

Network microstructure observed at the gel-air interface differs from that within the bulk gel (Figure 4.7a). In Figure 4.7aii, there seems to be greater alignment of the constituent domain fibres right at the edge of the gel. In figures 4.5aiii to 4.5av, a region of tighter packed spherulite-like domains is seen at this edge, with smaller, or in some cases no, gaps seen between the spherulites. Overall, this layer of differing domain morphology aligns with the 150 µm suspected critical depth seen earlier within the puncture data. The contrast in morphology here to the bulk gel is even more apparent when compared to a set of images taken sequentially from the air-gel interface across the bulk gel (Figure 4.7b). Here, the network further into the bulk of the gel displays more frequent and larger pores in the network alongside less densely packed spherulitic domains than is present at the gels surface. Next pH triggered 2NapFF gels were imaged in the same way to see if similar behaviour was present within the more uniform networks these gels have been shown to present (Figure 4.8).[6, 9]

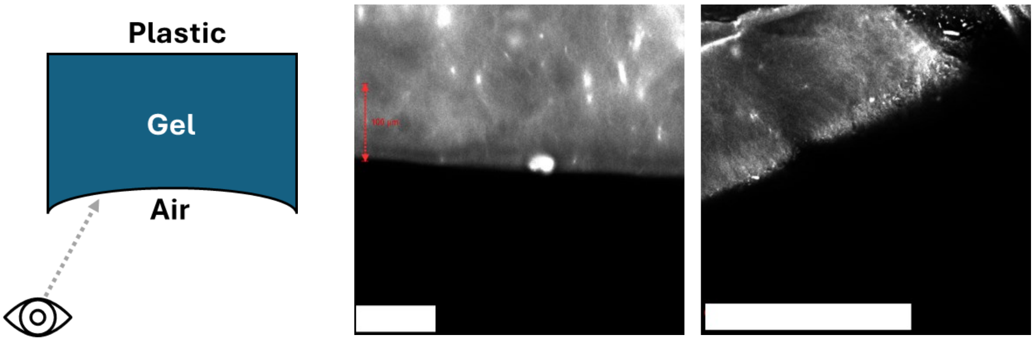

Figure 4.8 Confocal microscope images of 2NapFF pH triggered gel cross sections (5 mg mL^{-1}, GdL 8 mg mL^{-1}). Nile blue A dye (2 µl of a 0.1 wt% aqueous solution per mL of gel) was incorporated into imaged gels. Scale bars (white) = 100 µm. Red dashed arrows that correspond to 100 µm in length have been added. Cartoon schematic shows position of imaging with respect to sliced gel sample. Different orientations are a result of imaging at different positions along the curved air-gel interface.

Whilst it does seem that there are slight morphological differences present within the network at the surface of these gels, it is difficult to be certain of this. The underlying gelator fibres within these networks are thinner and much more densely packed as shown in Chapter 3, making clear imaging hard to achieve. For this reason, 2NapFV solvent and pH triggered gels were also imaged in the same manner (Figure 4.9). In Chapter 3 this was shown to allow for better network visualization via confocal microscopy due to increased fibre diameter.

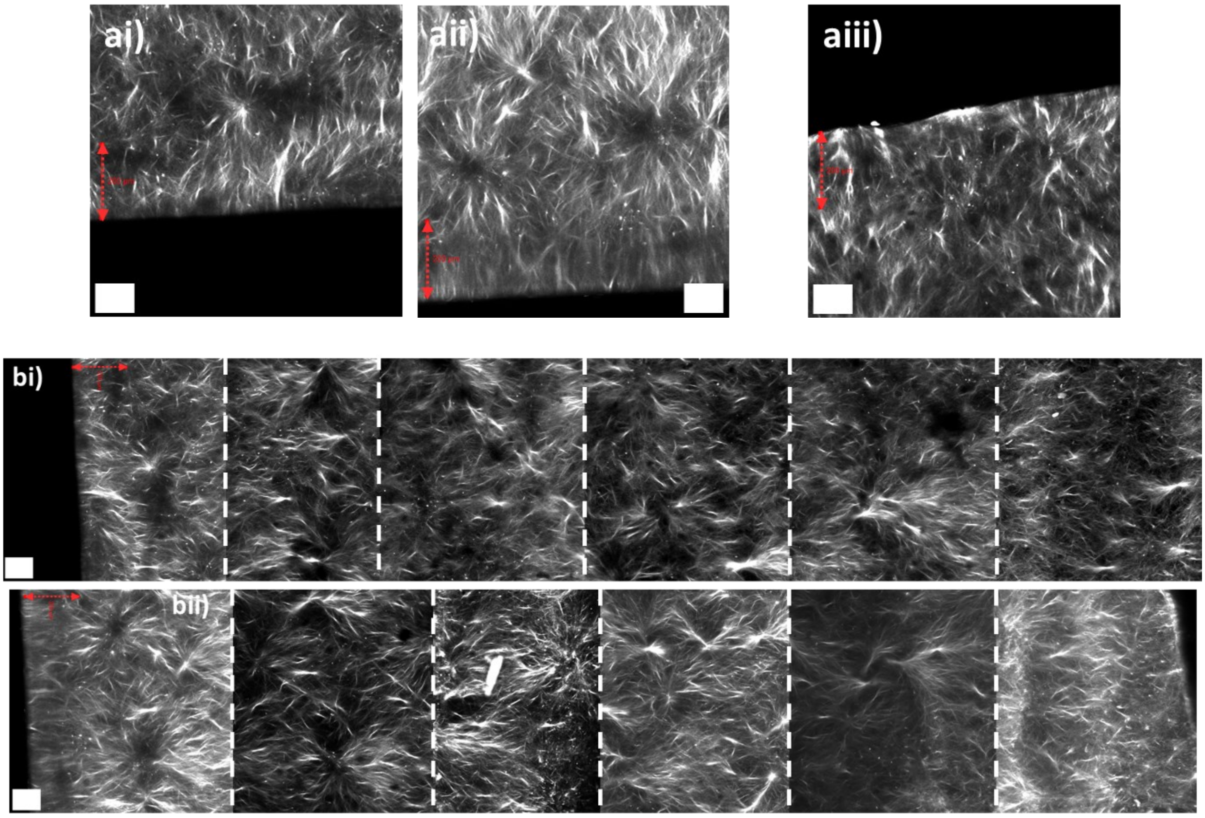

Figure 4.9 Confocal microscope images of 2NapFV pH triggered gel cross sections (5 mg mL^{-1}, GdL 8 mg mL^{-1}). Nile blue A dye (2 µl of a 0.1 wt% aqueous solution per mL of gel) was incorporated into imaged gels. Scale bars (white) = 100 µm. Red dashed arrows that correspond to 200 µm in length have been added. (a) The gelator networks present at the (i & ii) air-gel and (iii) gel-plastic interfaces within separate gel samples. (b) Two compiled sets of images of the gelator network within a gel from the air-gel interface (left) through to the bulk gel/ gel-plastic interface (right). Individual images are highlighted with white dashed lines. Imaging was carried out in the same way as highlighted in Figures 4.7ai & 4.7c.

Within Figure 4.9a, clear fibre alignment within a more densely packed region of the gelator network can be observed at the air-gel interfaces (4.9ai & 4.9aii). The length of this area closely matches that of the 150 µm critical depth observed in similar gels during puncture testing. Figure 4.9aiii shows the opposite gel-plastic border with a 2NapFV pH triggered gel. Here slight differences of the network within the gel at the border appear to be seen but are less obvious and appear to be localised to a smaller area (around 50 µm in length). These morphological network differences are highlighted when compared to additional images from within the bulk gel (Figure 4.9b). Solvent triggered 2NapFV gels were also examined via confocal microscopy (Figure 4.10). The more readily visualised fibres were hoped to provide further support of gel surface network differences.

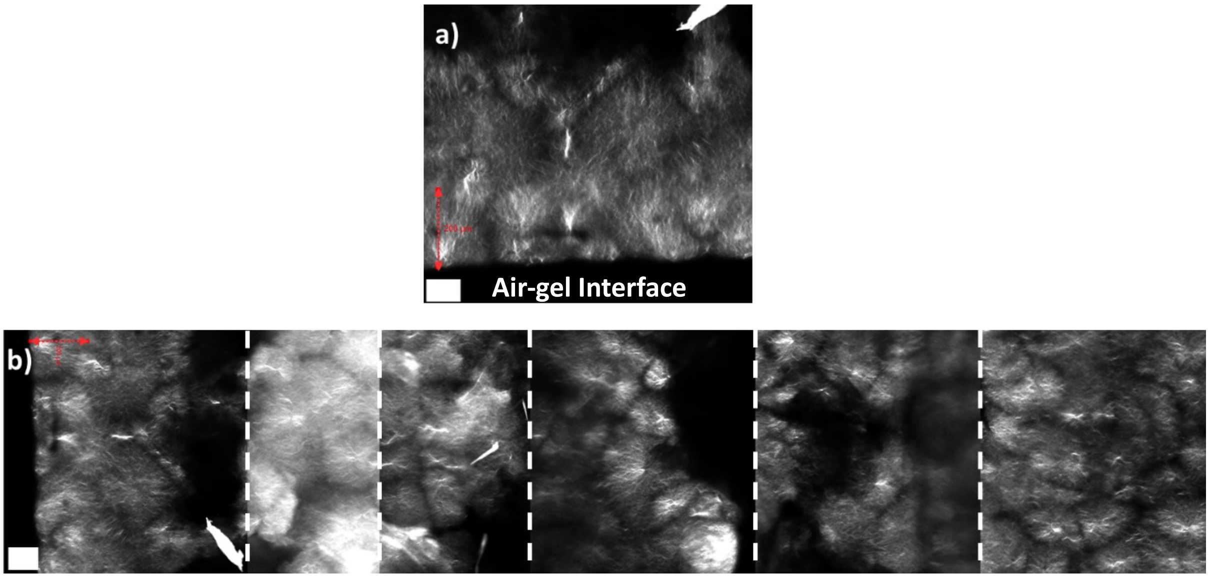

Figure 4.10 Confocal microscope images of 2NapFV solvent triggered gel cross sections (5 mg mL^{-1}, DMSO: H_2O, 20%). Nile blue A dye (2 µl of a 0.1 wt% aqueous solution per mL of gel) was incorporated into imaged gels. Scale bars (white) = 100 µm. Red dashed arrows that correspond to 200 µm in length have been added. (a) The gelator network present at the air-gel interface within a gel. (b) A combined set of images of the gelator network within a single gel from the air-gel interface (left) through to the bulk gel (right). Individual images are highlighted with white dashed lines. Imaging was carried out in the same way as highlighted in Figures 4.7ai & 4.7c, with the air-gel interface aligned with the bottom of the image (a) or the left hand side (b).

From Figure 4.10a, a layer within the gelator network consisting of more densely packed domains is again seen, corresponding to a depth of around 100 µm into the gel. Compared to the bulk gel, a more closely packed layer is maintained at the gel surface (Figure 4.10b). To explore this phenomenon, the study was expanded to include heat-cool triggered gels. As neither 2NapFF nor 2NapFV readily form gels via this method, owing to their inherent low solubility in water, other systems were explored. Initially agarose gels were proposed as good candidates as agarose is commonly available and produces very reproducible and well-reported gels under relatively mild conditions.[49, 50] This was used for the rheological portion of this study however despite trialling multiple dyes systems available, no clear confocal microscopy images could be achieved on the instrument available. As such, a different known LMWG, DBS-hydrazide (Figure 4.11a), was used as an example of a heat-cool low molecular weight gel instead (Figure 4.11).[40]

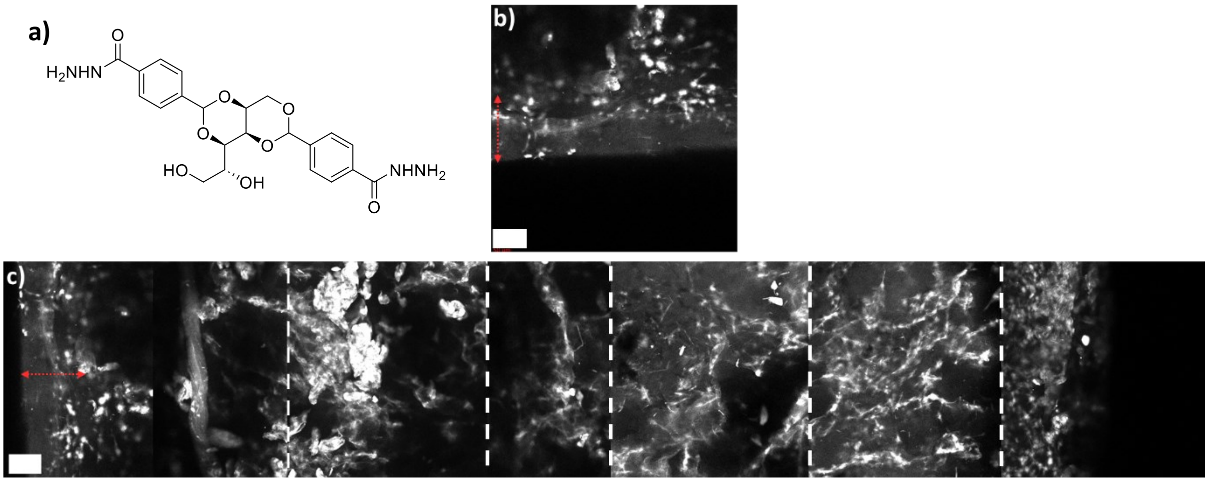

Figure 4.11 a) Chemical structure of the LMWG DBS-hydrazide. (b & c) Confocal microscope images of DBS-hydrazide heat-cool triggered gel cross sections (4 mg mL^{-1}). Nile blue A dye (2 µl of a 0.1 wt% aqueous solution per mL of gel) was incorporated into imaged gels. Scale bars (white) = 100 µm. Red dashed arrows that correspond to 200 µm in length have been added. (b) The gelator network present at the air-gel interface within a gel. (c) A combined set of images of the gelator network within a single gel from the air-gel interface (left) through to the bulk gel (right). Individual images are highlighted with white dashed lines. Imaging was carried out in the same way as highlighted in Figures 4.7ai & 4.7c.

From Figure 4.11a, it can be seen that the DBS-hydrazide gels are in good agreement with earlier findings for the pH and solvent triggered dipeptide gels, again presenting a gel layer differing from the bulk network microstructure. Individual gelator fibres are less readily distinguished within these gels, preventing evaluations as to fibre packing and density at this border. However, a clear boundary layer of the expected length scale is still observed, with differences to the overall microstructure present in the rest of the gel.

4.2.3 Rheology

With a gel surface layer of differing network morphology clearly observed from confocal microscopy studies, it was hoped that this could be correlated with a measurable difference in mechanical properties via oscillatory rheology. 2NapFF solvent and pH triggered gels as well as agarose and DBS-hydrazide heat-cool gels were selected as rheological samples for testing. The first experiment involved probing any potential differences in mechanical properties between the top and bottom surfaces of the gel, i.e. the gel in contact with the atmosphere (air) or the vessel (plastic) during gelation (Figure 4.12). This was achieved through the formation of disc shaped gels, reminiscent of hockey pucks. These gel pucks were then tested using a parallel plate geometry with the gel upright, upside down (inverted) or upright with the top layer removed (Figure 4.12e). In this way the top plate that oscillates and imparts the rotational shear stress would be acting on different surfaces or the bulk of the gel.

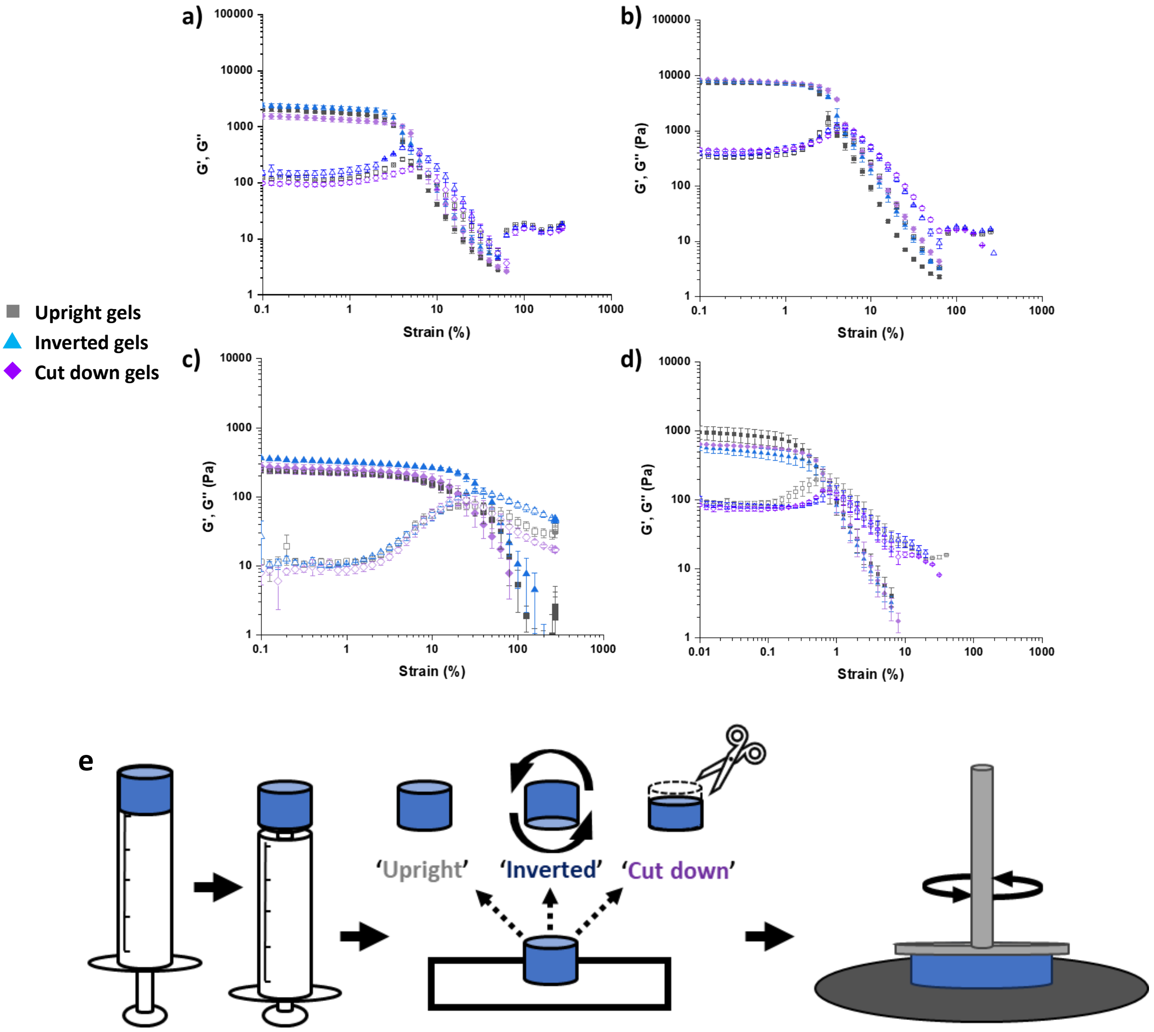

Figure 4.12 Rheological strain sweeps (Strain = 0.1 – 1000 %, Frequency = 10 rad s^{-1}) of (a) 2NapFF solvent (5 mg mL^{-1}, 2 mL, 20% DMSO), (b) 2NapFF pH (5 mg mL^{-1}, 2 mL, GdL (8 mg mL^{-1})), (c) agarose (5 mg mL^{-1}, 2 mL,), (d) DBS-hydrazide (4 mg mL^{-1}, 2 mL,) gels. For each experiment: upright gels are shown with grey squares, inverted gels with blue triangles and cut down gels with purple diamonds. G′ and G″ are represented by solid and hollow shapes respectively. (e) Cartoon schematic of how gel 'puck' samples were formed and modified for rheology. For corresponding frequency data, see Appendix, Figure C.1.

However, it is evident from Figure 4.12 that very little difference in viscoelastic response is seen between any of the three differently processed samples within each of the gel systems. This indicates that, at least on this scale and with respect to oscillatory shear, any existing surface layers are having no effect on the overall gel mechanical properties. The next experiment tested different volumes of each gel to produce shorter and taller samples (Figure 4.13). Any changes in mechanical properties caused as a result of the surface layers would be expected to have a greater effect within smaller samples, owing to a higher ratio of gel within the surface layers compared to the bulk of the sample.

Here differences are seen in viscoelastic response between the smaller and larger samples of each gel, with the shorter gels in most cases possessing lower G′ and G″ values except for the 2NapFF pH triggered gels where the shorter gel instead shows an increase in G′ and G″. Whilst it is likely that a factor contributing to this difference in mechanical properties is simply the reduction in sample volume;

a smaller gel means less material to resist any applied shear stress, the differing gelator network within the surface layer may play a part here too. As the same geometry is utilised to test the same sized top surface of gels in the same vessels, it is expected that some sensitivity to network differences with the surface layer of gel would be seen. A reduction in sample volume would be expected to have a significantly higher effect if testing with a cup and vane geometry, due to less material being in direct contact with the vane.

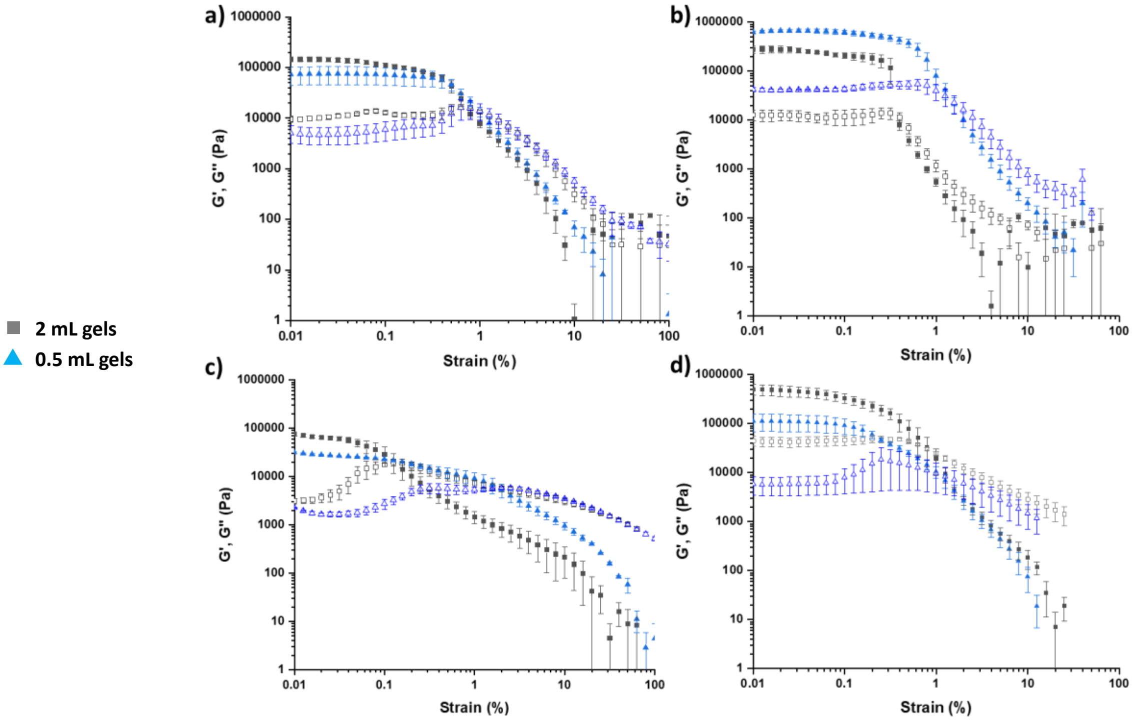

Figure 4.13 Rheological strain sweeps (Strain = 0.01 – 100 %, Frequency = 10 rad s^{-1}) of (a) 2NapFF solvent (5 mg mL^{-1}, 20% DMSO), (b) 2NapFF pH (5 mg mL^{-1}, GdL (8 mg mL^{-1})), (c) agarose (5 mg mL^{-1}), (d) DBS-hydrazide (4 mg mL^{-1}) gels. For each experiment: 2 mL gels are represented by black squares and 0.5 mL gels with blue triangles. G' and G'' are represented by solid and hollow shapes respectively. For corresponding frequency data, see Appendix, Figure C.2.

A final set of rheological experiments were carried out to directly see the impact of a gel layer possessing a higher gelator concentration (Figure 4.14). To achieve this, a 1.8 mL 2NapFF (solvent or pH) or agarose gel was formed at the standard 5 mg mL^{-1} gelator concentration used in earlier experiments. These were allowed to set and left long enough to ensure gelation was complete. Next a 0.2 mL gel of the same gelator, but at a higher concentration of 15 mg mL^{-1} was formed on top. Once complete, multi-layered gels containing a higher gelator concentration (and thus possessing more densely packed gelator networks) were produced and tested via both parallel plate 12.5 (PP) and cup and vane geometries. These were tested alongside equivalent gels at either 5 or 15 mg mL^{-1}. Attempts were made to implement the DBS-hydrazide system in the same way, but gels could not be produced at higher gelator loadings. This is owing to poor solubility of the LMWG in water. During gelation at lower LMWG concentration (4 mg mL^{-1}), complete dissolution is only achieved very close to the solvents boiling point. Therefore, increasing the gelator concentration prevents complete dissolution, meaning no gels can be produced.

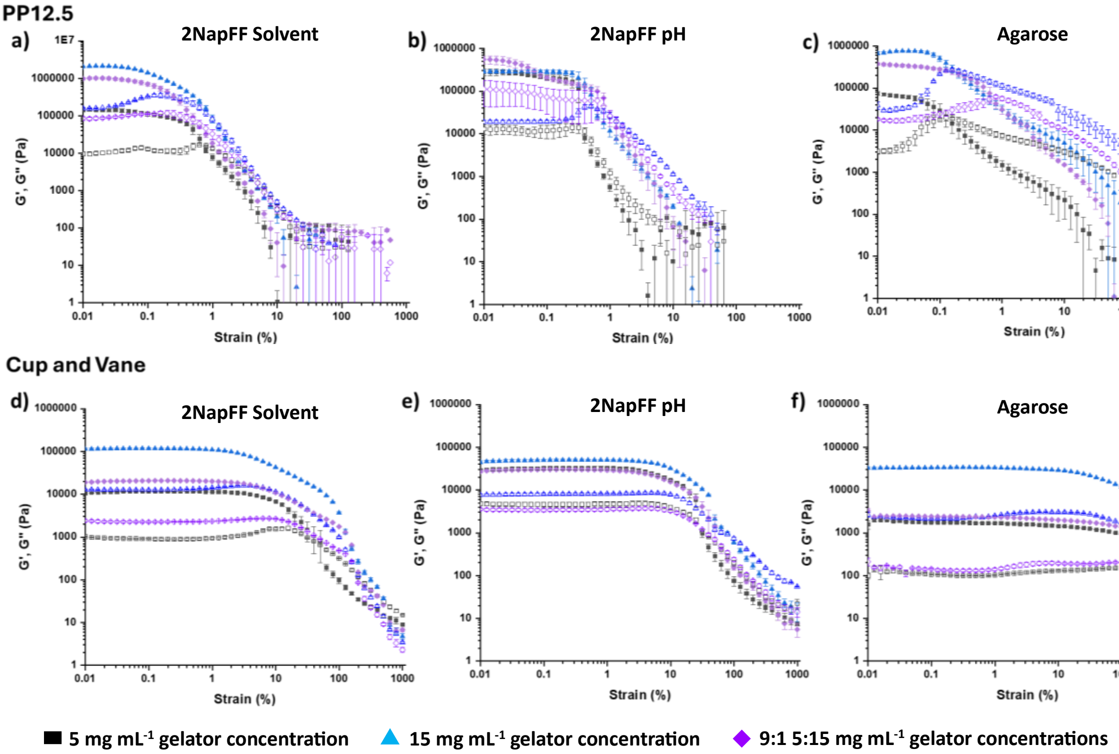

Figure 4.14 Rheological strain sweeps (Strain = 0.01 – 1000 %, Frequency = 10 rad s^{-1}) of (a & d) 2NapFF solvent (2 mL, 20% DMSO), (b & e) 2NapFF pH (2 mL, GdL (8 or 24 mg mL^{-1})), (c & f) agarose (2 mL) gels. Gels with a LMWG concentration of 5 mg mL^{-1} are represented by black squares, 15 mg mL^{-1} blue triangles and those with a 9:1 volume composition of 5 mg mL^{-1} to 15 mg mL^{-1} by purple diamonds. G′ and G′′ are represented by solid and hollow shapes respectively. Both parallel plate (12.5 mm, a – c) and cup and vane (d-f) geometries were used. For corresponding frequency data, see Appendix, Figure C.3.

From Figure 4.14, a clear difference in rheological profiles for the same material is seen between geometries. This is unsurprising as the vane will always have significantly more intimate contact with the sample than the parallel plate, which is only imparting rotational shear on the samples top surface.[51, 52] Lower G′ and G′′ values as well as a more detailed deviation of these from the linear viscoelastic region (LVER) as gel network breakdown occurs show this. Overall, the higher gelator concentration gels were stiffer than their lower concentration equivalents, possessing higher G′ and G′′ values.

For the 2NapFF solvent triggered gels (Figures 4.14a & 4.14d) and agarose gels (Figures 4.14c & 4.14f), it can be seen that the mechanical properties of the multi-layered gels samples of differing concentrations are more aligned with either the higher or lower single concentration gels, depending on the geometry used. When tested with the PP, G′ and G′′ values of the multi-layered gels for both 2NapFF and agarose gels were close to those of the solely higher concentration equivalent gels (Figure 4.14a & 4.14c). But when using the cup and vane, G′ and G′′ values for the same multi-layered gels were far closer to those of the lower concentration equivalent gels (Figure 4.14d & 4.14f). For the 2NapFF pH triggered gels when tested via cup and vane, there is a closer alignment of G′ and G′′ of the multi-layered gels to those of the lower gelator concentration equivalent gels (Figure 4.14e). But the difference in stiffness between the 5 and 15 mg mL^{-1} of the pH triggered 2NapFF gels is minimal. This is likely due to the already relatively uniform gelator network, that will just become more densely populated with fibres, whereas the non-uniform network of the solvent triggered gels will become more populated, either causing extended domain growth or potentially transitioning closer to a uniform network through additional domain formation. Surprisingly, the multi-layered 2NapFF pH triggered gel displayed higher G′ and G″ values than the solely 15 mg mL^{-1} gel when tested via PP. The cause behind this is unclear.

4.2.4 Nanoindentation

Nanoindentation data were collected and processed by Dipankar Ghosh (University of Glasgow).

After no clear trend of bulk mechanical properties influenced by differing microstructure from rheology, focus was turned to nanoindentation.[53] It was hoped this would provide an alternate means of probing any potentially affected mechanical properties at the gels surface on a smaller operational length scale than oscillatory rheology.[54] 2NapFF gels were formed as 2 mL gel pucks and sliced into cross sections as per earlier confocal microscopy studies. The bulk gel at the centre of the sample and the gel as close as possible to the air-gel interface face were both probed (Figure 4.15).

No significant differences between the Young's moduli at the surface or within the bulk gel were measured in either 2NapFF solvent or pH triggered gels (Figure 4.15). Nanoindentation generated data does typically show a larger spread, as clearly demonstrated by the significant errors reported here.[54] Whilst these may improve through further testing of additional samples, a larger flaw here may be accurate positioning of the probe during measurements. It was difficult to reliably set up surface tests with the probe positioned at a suitable depth within the gel to effectively probe the region containing observed network differences.

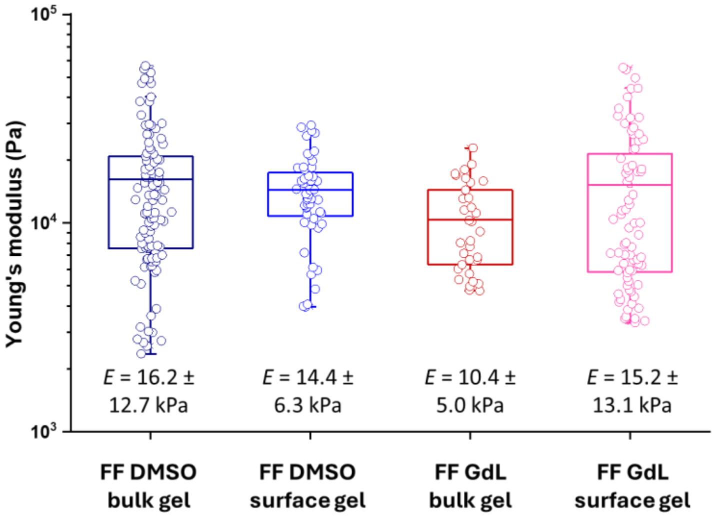

Figure 4.15 Plots of Young's moduli (*E)* measured via nanoindentation of 2NapFF (5 mg mL^{-1}) (blue) solvent and (red) pH triggered gel at the surface (light blue and pink) or within the bulk gel (dark blue and red). Gels were probed with a 3 µm spherical tip indenter.

4.3 Conclusion

As a first step towards furthering the understanding of cavitation rheology for application to our dipeptide based low molecular weight gels, puncture of exemplar gels by needle was undertaken. Within these tests, unexpected results arose that may have indicated a tougher surface layer formed at the air-gel interface. From confocal microscopy, observed microstructure of the gelator network present at the gels surface showed morphological changes within solvent and pH triggered dipeptide low molecular weight gels, as well as thermally triggered low molecular weight gels. Differences in microstructure domain packing, corresponding network pore size as well as fibre alignment and density were observed across different gel systems. The size of this region corresponds to the suspected critical depth values from the unexpected peaks initially observed within the puncture study.

A correlation of these gel surface layer to differences in mechanical properties was explored through oscillatory rheological and nanoindentation studies. But, whilst some of the studies may suggest this to be the case, no definitive evidence confirming this was found using these techniques. Subsequent control tests for the gel puncture study confirmed the unexpected peaks to be an instrument artefact, in agreement with the rheological and nanoindentation data.

From these results, yet another facet of these materials that has long been largely overlooked and ignored has been explored. Whilst there is some evidence of differences present within the gelator network microstructure at the air-gel interface, these were not seen to have a significant measurable impact on the bulk properties of the gels tested here.

4.4 Experimental

Materials:

LMWGs 2NapFF (F = phenylalanine), 2NapFV (V = valine) and DBS-Hydrazide were synthesized using methods previously described in the literature.[55, 56] Agarose (Type 1, low EEO) and Nile Blue A dye were both purchased from Sigma Aldrich (Merck). DMSO was purchased from Fisher Scientific. All purchased chemicals were used as received. Deionized water was used throughout.

Preparation of LMWG solutions and gels:

LMWGs NapFF (F = phenylalanine) and 2NapFV (V = valine) were used to form solvent-switch triggered hydrogels as previously outlined.[6] A known amount of gelator was dissolved in DMSO (at a concentration of 25 or 75 mg mL^{-1}), sonicated for 2 minutes, and diluted with water in one aliquot to produce gels at a final gelator concentration of 5 or 15 mg mL^{-1}, and a volume fraction (ϕ) of DMSO of 0.2.

LMWGs NapFF (F = phenylalanine) and 2NapFV (V = valine) were used to form pH triggered hydrogels as previously outlined.[57] Gelator was added to water and NaOH (0.1 M, 1 molar equivalent) to produce a high pH aqueous LMWG solution at 5 or 15 mg mL^{-1}. Aliquots of NaOH (1 M) were used to pH adjust the gelator solution to pH 10.5. Desired volumes of gelator solution were decanted into appropriate vessels and triggered with the addition of GdL (8 or 24 mg mL^{-1} depending on gelator concentration). After trigger addition, solutions were briefly stirred manually before being left to gel overnight.

Agarose gels were prepared via a heat-cool method.[50] Agarose was added to water at 5 or 15 mg mL^{-1} in a conical flask fitted with reflux condenser. This was heated and stirred until complete dissolution and then for a further ten minutes. Hot gelator solutions were allowed to cool for 3 minutes before transfer of a desired amount into an appropriate vessel by automatic pipette. Solutions were allowed to cool overnight forming gels.

DBS-hydrazide gels were also prepared via a heat-cool method, as previously outlined.[58] Gelator was added to water in a screw top glass vial at 4 mg mL^{-1}. The vial was closed tightly and sonicated for 10 minutes to produce a cloudy white suspension. The suspension was heated with a heat-gun until subsequent gelator dissolution (around 90 °C) , yielding a transparent solution (typically just before the water started to boil). These gelator solutions were then poured into an appropriate pre-heated vessel. Solutions were allowed to cool overnight, forming gels.

For rheology gels were either made in Sterilin vials or in 12 mL plastic syringes with the end removed.

Within the Sterilin vials, gels were made as either 2 mL (5 or 15 mg mL^{-1}) gelator concentration samples, 2 or 0.5 mL (5 mg mL^{-1}) samples or gels with a high gelator concentration top layer. The latter were made by first making a 1.8 mL 5 mg mL^{-1} gel and making a 0.2 mL 15 mg mL^{-1} gel of the same gelator on top of this (Figure 4.16). The lower layer gels were left overnight to ensure full gelation before casting the second layer on top. Solutions were briefly rolled around the vial during gelation to ensure even coverage by this thinner layer. Reliably creating consistent higher concentration gel layers at volumes smaller than 0.2 mL was not possible.

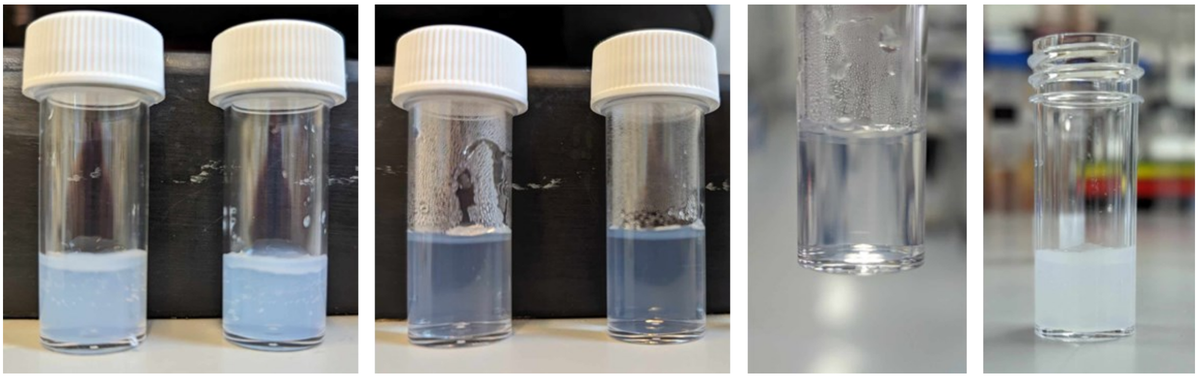

Figure 4.16 Images of exemplar gels samples with a thin second higher gelator concentration layer created on top of a bigger lower gelator concentration.

To make disc shaped gel 'pucks', gels were made as 2 mL gels with a gelator concentration of 5 mg mL^{-1}, except for the DBS-hydrazide gels which were formed at 4 mg mL^{-1}. These were made within 12 mL plastic syringes with the end sliced off, so as to be able to eject the gel from the syringe as a hockey puck shaped disc.

For gel puncture studies, gels were formed at 5 mg mL^{-1} for 2NapFF and 2NapFV and 4 mg mL^{-1} for DBS-hydrazide. These were produced using the above solvent and pH triggered methods for 2NapFF and 2NapFV and heat-cool method for DBS-hydrazide. Gels were produced as scaled up 6 mL samples within 7 mL Sterilin vials to allow for adequate testing depth.

Gel puncture measurements:

Gel puncture studies were carried out using hollow bore flat tipped stainless steel needles (Hamilton Company), with outer diameter (⌀) = 0.7, 0.5, 0.4, 0.3 and 0.2 mm. These were fixed and used in conjunction with a TA.XT Plus Texture Analyzer (Textile Technologies), fitted with a 50 N load cell to measure generated force and displacement.

Gels (6 mL in Sterilin vials) were raised onto the needle at a displacement rate of 5 mm s^{-1}. Force generated was measured through the base of the sample mounted in an appropriate holder affixed to the Texture Analyzer.[38]

Confocal microscopy:

For imaging, Nile blue A dye (0.1 wt% aqueous solution, 2 µL per mL of gel) was incorporated into gels to allow for observation by confocal fluorescence microscopy using a Zeiss LSM 710 confocal microscope fitted with Zeiss N-Achroplan 10× and LD EC Epiplan NEUFLUAR 50× (0.55 DIC) objectives.[6] Nile Blue fluorescence was achieved by excitation with a 634 nm He–Ne laser and emission detected between 650 and 710 nm.

Initial Z-stack imaging trials were attempted on 2 mL gels formed in cut down 7 mL Sterilin vials to enable an appropriate working distance to be reached. Slice interval and specific distance spanned per stack is reported alongside data.

For 'manual Z-stack' imaging gels were prepared as puck shaped samples as described above for rheology. These gels pucks were then ejected from the syringes and moved onto a clean microscope slide. Gels were then sliced with a fresh razor blade to form a gel cross section (Figure 4.6). This was manipulated to lay flat, allowing the microstructure of the gel to be imaged to a greater depth than a standard Z stack by imaging whilst moving horizontally along what was the original Z axis of the formed gel (Figure 4.6). These sets of images were taken from the air-gel interface moving towards the bulk of the gel, in some cases continuing to the gel-plastic interface (Figure 4.6).

Rheological measurements:

Samples for rheology were created as above. Rheological measurements were carried out using both MCR 301 and 101 rheometers (Anton Paar), fitted with either a cup and four-bladed vane geometry (ST10-4V-8.8/97.5-SN1910), 12.5 mm smooth (PP12.5-SN50710) or 25 mm (PP25/S-SN3135) sandblasted parallel plate geometries. The sandblasted parallel plate was used in conjunction with a sandpaper covered plate to reduce sample slippage during measurements.[59] The 12.5 mm parallel plate was used with a custom 3D printed vial holder mounted on the original stationary plate (Figure 4.17). Rheoplus/32 v3.40 software was used. All measurements were carried out in triplicate, at 25 °C. Cup and vane measurements were ran at a measuring gap of 1.8 mm. Parallel plate measurements were ran at measuring gaps resulting in a normal force of 0.1 N when initial geometry contact was made with the surface of the gel sample.

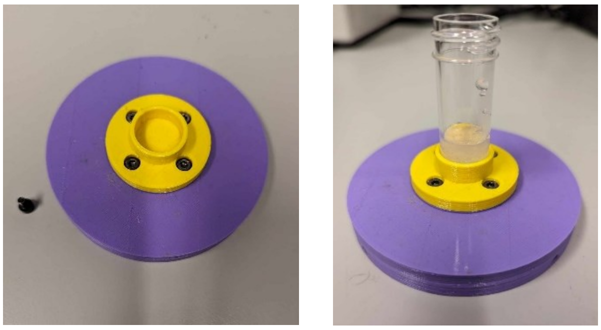

Figure 4.17 Image of a custom 3D printed Sterilin vial holder, mountable onto a standard Anton Paar MCR rheometer parallel plate.

Strain sweeps were run with strain = 0.01 to 1000 % at a frequency of 10 rad s^{-1}, unless sample slippage occurred in which case the run was terminated earlier at a strain value < 1000%. Frequency sweeps were run with frequency = 1 to 100 rad s^{-1} at a strain value located comfortably within the LVER of the material, derived from the corresponding strain sweep. Gels of differing height and concentrations (included those topped with a higher concentration gelator layer) within Sterilin vials were run on the MCR 301 instrument and the gel pucks were run on the MCR 101 101 instrument. Frequency data is included in the Appendix.

For the gel pucks, measurements were run on the MCR 101 instrument. Gels were ejected from syringes and slid onto glass microscope slides. These samples were then run as they were ("upright"), flipped upside down ("inverted"), or upright with a thin (~ 1-2 mm) layer of the top surface (the gel-air interface during gelation) sliced off with a fresh razor blade ("cutdown"). For the latter set, the top layer was removed before ejection from syringe (Figure 4.18).

Figure 4.18 Picture of a freshly prepared cut-down gel as a rheology sample. The gel would be ejected from the syringe and loaded onto rheometer after trimming down.

Nanoindentation:

Nanoindentation tests were carried out with a Chiaro instrument (Optics11, The Netherlands), following an established protocol.[54] The device contains a cantilever equipped with a 3 µm radius (R) spherical tip and a stiffness of 0.52 N m^{-1}. This nanoindenter was fitted on the top of an inverted Zeiss Axiovert 200M microscope.

Gels were sliced with a razor blade for nanoindentation measurements via the same method outlined above for confocal microscopy (Figure 4.6). The cut cross section of gel produced was positioned in a glass petri dish using a scalpel and glass microscope slide. To stop the gel from moving, a metal washer was used to weight it down. Deionised water was then added to cover the gel to keep it hydrated. The petri dish was then placed on the microscope's stage, aligning the surface of the gel in the Y-axis direction of the instrument. First, the indenter was positioned as close to the edge of the gel corresponding to the original air-gel interface and a matrix scan was performed along Y-axis, following this edge. Each sample underwent at least two matrix scans, with each scan comprising 25 indentations spaced 6 µm apart. Then to collect the measurements on the central bulk portion of gel, the cantilever was placed on the middle of the gel slice, and a matrix scan was performed along both X- and Y-directions to collect data from all regions.

For the data analysis, the forward segment of the force-displacement (F-z) curves was examined with a specialised open-source software.[54] A goodness of fit (GoF) algorithm was employed to transition from F-z to force-indentation (F-δ) curves. These F-δ curves were then fitted to the Hertz model for indentations up to δ = 0.1R to determine the gels' elastic characteristics.

4.5 References

1. J. W. Steed, *Chem. Comm.*, 2011, **47**, 1379-1383.
2. E. R. Draper and D. J. Adams, *Chem*, 2017, **3**, 390-410.
3. M. Djabourov, *Polym. Int.,* 1991, **25**, 135-143.
4. J. L. Andrews, E. Pearson, D. S. Yufit, J. W. Steed and K. Edkins, *Crys. Growth Des.*, 2018, **18**, 7690-7700.
5. J. Raeburn, A. Z. Cardoso and D. J. Adams, *Chem. Soc. Rev.*, 2013, **42**, 5143-5156.
6. L. Chen, J. Raeburn, S. Sutton, D. G. Spiller, J. Williams, J. S. Sharp, P. C. Griffiths, R. K. Heenan, S. M. King, A. Paul, S. Furzeland, D. Atkins and D. J. Adams, *Soft Matter*, 2011, **7**, 9721-9727.
7. J. Raeburn, G. Pont, L. Chen, Y. Cesbron, R. Lévy and D. J. Adams, *Soft Matter*, 2012, **8**, 1168-1174.
8. H. Wang, Z. Yang and D. J. Adams, *Mater. Today*, 2012, **15**, 500-507.
9. C. Colquhoun, E. R. Draper, R. Schweins, M. Marcello, D. Vadukul, L. C. Serpell and D. J. Adams, *Soft Matter*, 2017, **13**, 1914-1919.
10. E. R. Draper and D. J. Adams, *Nat. Mater.*, 2024, **23**, 13-15.
11. E. R. Draper and D. J. Adams, *Langmuir*, 2019, **35**, 6506-6521.
12. J. Raeburn, C. Mendoza-Cuenca, B. N. Cattoz, M. A. Little, A. E. Terry, A. Z. Cardoso, P. C. Griffiths and D. J. Adams, *Soft Matter*, 2015, **11**, 927-935.
13. W. Helen, P. De Leonardis, R. V. Ulijn, J. Gough and N. Tirelli, *Soft Matter*, 2011, **7**, 1732-1740.
14. X. Huang, S. R. Raghavan, P. Terech and R. G. Weiss, *J. Am. Chem. Soc.*, 2006, **128**, 15341-15352.
15. M. A. Greenfield, J. R. Hoffman, M. Olvera de la Cruz and S. I. Stupp, *Langmuir*, 2010, **26**, 3641-3647.
16. M. C. Nolan, A. M. Fuentes Caparrós, B. Dietrich, M. Barrow, E. R. Cross, M. Bleuel, S. M. King and D. J. Adams, *Soft Matter*, 2017, **13**, 8426-8432.
17. N. A. Dudukovic and C. F. Zukoski, *Langmuir*, 2014, **30**, 4493-4500.
18. D. Orsi, A. Vezzani, R. Burioni, A. Pucci, G. Ruggeri and L. Cristofolini, *Colloids Surf. A Physicochem. Eng. Asp.*, 2014, **441**, 912-918.
19. S. Cheng, Z. Lou, L. Zhang, H. Guo, Z. Wang, C. Guo, K. Fukuda, S. Ma, G. Wang, T. Someya, H. M. Cheng and X. Xu, *Adv. Mater.*, 2023, **35**, 2206793.
20. Z. J. He, C. Chu, R. Dickson, K. Okuda and L. H. Cai, *Am. J. Physiol. Lung Cell. Mol. Physiol.*, 2024, **326**, L292-L302.
21. L. Saunders and P. X. Ma, *Macromol. Biosci.*, 2019, **19**, 1800313.
22. A. J. Feliciano, C. Van Blitterswijk, L. Moroni and M. B. Baker, *Acta Biomater.*, 2021, **124**, 1-14.
23. S. Das and A. Ghatak, *J. Mater. Sci.*, 2011, **46**, 2895-2904.
24. S. Fakhouri, S. B. Hutchens and A. J. Crosby, *Soft Matter*, 2015, **11**, 4723-4730.
25. W. Wang, H. Wang, C. Ren, J. Wang, M. Tan, J. Shen, Z. Yang, P. G. Wang and L. Wang, *Carbohydr. Res.*, 2011, **346**, 1013-1017.
26. X. Q. Dou and C. L. Feng, *Adv. Mater.*, 2017, **29**, 1604062.
27. H. Shigemitsu and I. Hamachi, *Acc. Chem. Res.*, 2017, **50**, 740-750.
28. T. Boland, V. Mironov, A. Gutowska, E. A. Roth and R. R. Markwald, *Anat. Rec.*, 2003, **272A**, 497-502.
29. T. J. Hinton, A. Hudson, K. Pusch, A. Lee and A. W. Feinberg, *ACS Biomater. Sci. Eng.*, 2016, **2**, 1781-1786.
30. I. M. Lei, D. Zhang, W. Gu, J. Liu, Y. Zi and Y. Y. S. Huang, *Adv. Mater. Technol.*, 2023, **8**, 2300001.

31. C. W. Barney, C. E. Dougan, K. R. McLeod, A. Kazemi-Moridani, Y. Zheng, Z. Ye, S. Tiwari, I. Sacligil, R. A. Riggleman, S. Cai, J. H. Lee, S. R. Peyton, G. N. Tew and A. J. Crosby, *Proc. Nat. Acad. Sci.*, 2020, **117**, 9157-9165.
32. J. A. Zimberlin, N. Sanabria-Delong, G. N. Tew and A. J. Crosby, *Soft Matter*, 2007, **3**, 763-767.
33. A. M. Fuentes-Caparrós, B. Dietrich, L. Thomson, C. Chauveau and D. J. Adams, *Soft Matter*, 2019, **15**, 6340-6347.
34. M. J. S. Hill, A. M. Fuentes-Caparrós and D. J. Adams, *Biomacromolecules*, 2023, **24**, 4253-4262.
35. K. C. Bentz, N. Sultan and D. A. Savin, *Soft Matter*, 2018, **14**, 8395-8400.
36. C. W. Barney, I. Sacligil, G. N. Tew and A. J. Crosby, *Soft Matter*, 2022, **18**, 4220-4226.
37. C. W. Barney, Z. Ye, I. Sacligil, K. R. McLeod, H. Zhang, G. N. Tew, R. A. Riggleman and A. J. Crosby, *Proc. Nat. Acad. Sci.*, 2022, **119**, e2112389119.
38. C. W. Barney, Y. Zheng, S. Wu, S. Cai and A. J. Crosby, *Soft Matter*, 2019, **15**, 7390-7397.
39. S. B. Hutchens, S. Fakhouri and A. J. Crosby, *Soft Matter*, 2016, **12**, 2557-2566.
40. D. J. Cornwell, B. O. Okesola and D. K. Smith, *Soft Matter*, 2013, **9**, 8730-8736.
41. F. Horkay and G. B. McKenna, in *Physical Properties of Polymers Handbook*, ed. J. E. Mark, Springer, New York, 2nd edn, 2007, ch. 29, pp. 497-523.
42. S. Seiffert and J. Sprakel, *Chem. Soc. Rev.*, 2012, **41**, 909-930.
43. T. Rossow and S. Seiffert, *Polym. Chem.*, 2014, **5**, 3018-3029.
44. R. Van Lommel, W. M. De Borggraeve, F. De Proft and M. Alonso, *Gels*, 2021, **7**, 87.
45. G. Hild, *Prog. Polym. Sci.*, 1998, **23**, 1019-1149.
46. A. N. Gent and C. Wang, *J. Mater. Sci.*, 1991, **26**, 3392-3395.
47. S. Kundu and A. J. Crosby, *Soft Matter*, 2009, **5**, 3963-3968.
48. S. Raayai-Ardakani, D. R. Earl and T. Cohen, *Soft Matter*, 2019, **15**, 4999-5005.
49. M. R. Letherby and D. A. Young*, J. Chem. Soc., Faraday Trans. 1*, 1981, **77**, 1953-1966.
50. P. Serwer, *Electrophoresis*, 1983, **4**, 375-382.
51. C. Servais, S. Ravji, C. Sansonnens and I. Bauwens, *J. Texture Stud.*, 2002, **33**, 487-504.
52. A. M. Fuentes-Caparrós, Z. Canales-Galarza, M. Barrow, B. Dietrich, J. Läuger, M. Nemeth, E. R. Draper and D. J. Adams, *Biomacromolecules*, 2021, **22**, 1625-1638.
53. B. Bhushan and M. L. B. Palacio, in *Encyclopedia of Nanotechnology*, ed. B. Bhushan, Springer, Dordrecht, 1st edn, 2012, pp. 1576-1596.
54. G. Ciccone, M. Azevedo Gonzalez Oliva, N. Antonovaite, I. Lüchtefeld, M. Salmeron-Sanchez and M. Vassalli, *J. Vis. Exp.*, 2022, **179**, e63401.
55. Z. Yang, G. Liang, M. Ma, Y. Gao and B. Xu, *J. Mater. Chem.*, 2007, **17**, 850-854.
56. L. Chen, S. Revel, K. Morris, L. C. Serpell and D. J. Adams, *Langmuir*, 2010, **26**, 13466-13471.
57. D. J. Adams, M. F. Butler, W. J. Frith, M. Kirkland, L. Mullen and P. Sanderson, *Soft Matter*, 2009, **5**, 1856-1862.
58. B. O. Okesola, V. M. P. Vieira, D. J. Cornwell, N. K. Whitelaw and D. K. Smith, *Soft Matter*, 2015, **11**, 4768-4787.
59. C. Carotenuto and M. Minale, *J. Nonnewton. Fluid Mech.*, 2013, **198**, 39-47.

Chapter 5

Conclusions

5. Conclusions

Low molecular weight hydrogels of *N*-protected dipeptide LMWGs are a class of material with significant potential for a wide range of applications, from stimuli-responsive smart materials to the biomedical field. Their versatility stems from the inherent modular nature of these LMWGs, thus allowing for tuneable material properties in the resulting gels. This is bolstered by the different gelation triggers available, wherein distinct gels possessing unique properties can be produced from the same starting LMWG. Procedures within gelation protocols must be consistent, with variables carefully controlled to accurately reproduce gels. Whilst many aspects of these methods have been explored, many are still overlooked, some of which may significantly impact the final gel properties. To further develop our grasp of these materials that are still at times poorly understood, it is vital to continue to explore factors that may affect their formation. A deeper understanding of these factors would help guide and drive future innovation within the applications of low molecular weight gels.

Effective 3D printing of solvent-triggered dipeptide, and other, LMWG based gels has previously been shown. These have largely been based off a single printed gel component, with different layers produced by varying concentration of the same LMWG. We have demonstrated the successful construction of 3D printed multi-layered gel samples, through the combination of printed layers of the gels of two different dipeptide LMWGs. Each of these inherently has different mechanical properties and thus the specific combinations and ordering of these different gel layers influences the overall sample mechanical properties. To the best of our knowledge, this is the first time 3D printed multi-layer gel constructs have been printed from two different gels that are pre-formed prior to extrusion, with most examples typically printing gelator solutions, with gelation subsequently taking place during or post extrusion. The interaction of separately printed gels extruded in very close proximity to one another was probed to assess the extent to which they integrate, if at all. Two LMWGs that produce networks that are easily distinguishable when observed *via* confocal microscopy were chosen to facilitate this. This was then accentuated through the incorporation of a different fluorescent dye in each resulting gel, clearly showing conserved borders between separately printed gels. The different gels remained discrete, with no amalgamation of the two. It is hoped that these findings will help guide the further development of 3D printed low molecular weight gel samples with heterogenous mechanical properties, improving their suitability for biomedical applications.

The use of different gelation triggers and even subtle variations within these, such as solvent type or relative solvent ratios, has been previously shown to produce different gels, even when using the same initial LMWG. One factor that, to the best of our knowledge, has largely been previously ignored is the vessel size in which these low molecular weight gels are formed, with gels formed on varying scales and in different vessels assumed to be identical. We have clearly demonstrated that this is not always the case, with different responses to imposed spatial constraints seen between solvent and pH-triggered gels of two different dipeptide LMWGs. Through confocal microscopy the solvent-triggered gels display clear differences in network morphology within different sized vessels, whereas pH-triggered equivalents do not. This is a result of the nucleation and growth process that generates the gelator network within solvent-triggered gels, producing more compartmentalised spherulite-like domains and the formation of a uniform fibrous network with the pH-triggered gels. During the former, the domain growth is affected by available space, whereas for the latter a uniform network is produced regardless. This correlates with the localised mechanical properties measured *via* cavitation rheology, with critical pressures varying with vessel size in solvent-triggered gels and remaining consistent for pH-triggered equivalents. Experiments were carried out to demonstrate multiple domain sizes formed within a single solvent-triggered gel using a vessel consisting of compartments of differing size. These findings highlight the importance of vessel size as a consideration when producing some low molecular weight gels. With the wide plethora of characterisation techniques available within the soft materials field which typically mandate different sample volumes and shapes, this is of wide relevance.

Finally, we investigated potential network differences at the surface of some supramolecular gels. Preliminary results from an investigation into the puncture of different low molecular weight gels by needle as an initial step to better understanding needle-induced cavitation rheology when applied to these materials indicated a difference in properties at the surface of these gels. Variations in the network microstructure were observed *via* confocal microscopy at the gel-air surface interface within the gels of multiple LMWGs, produced through solvent-switch, pH and heat-cool gelation triggers. Changes to fibre morphology and alignment were seen within this region. However, subsequent rheological and nanoindentation experiments showed no changes to mechanical properties measured at the gel surface by comparing the bulk and surface within samples of the aforementioned gels. These findings align with further needle puncture experiments that confirmed surface related data as instrument artefacts. Future testing with a modified protocol and a more sensitive detector may allow for accurate investigations into puncture of the surface of these gels. A better understanding of this would help secure a foundation to a more in-depth investigation into the use of cavitation rheology within the low molecular weight gel field, with the aim of augmenting its current capabilities.

In conclusion, we have investigated vessel spatial constraints during gelation and surface network differences, two largely unexplored novel aspects for consideration when producing low molecular weight gels. We have shown the former to be an important factor for consideration for some low molecular weight gels and for others, a variable to at least rule out. Towards the useful application of these materials, we have further developed on our initial 3D printed low molecular weight gel system. Whilst currently still a very long way away from viability for real world biomedical applications, the expansion of this systems capabilities as demonstrated here moves it a step closer. Through this Thesis we hope to have contributed to a deeper understanding of hydrogels formed from *N*-protected dipeptide LMWGs and their applications.

6. Appendix: A

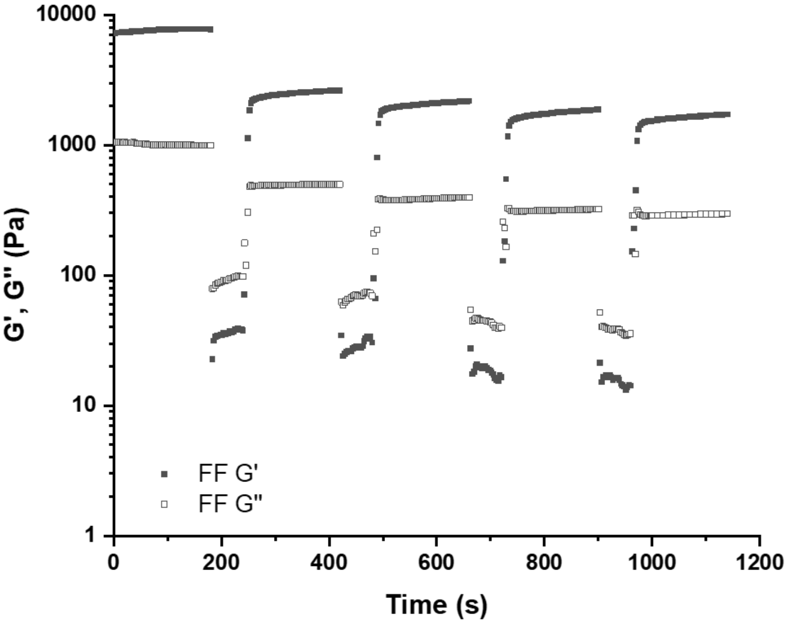

Figure A.1 Oscillatory shear recovery of G′ (filled shapes) and G′′ (hollow shapes) for solvent-triggered FmocFF (2 mL, 5 mg ml^{-1}, ϕ_{DMSO} 0.2) gels. Gels were subject to a constant frequency of 10 rad s^{-1} and an alternating strain of 0.5 % (200 s) and 300% (60 s). Destruction of underlying gelator network is seen in periods of high strain, evidenced by G′′ > G′, with recovery of mechanical properties seen upon returning to low strain (G′ < G′′).

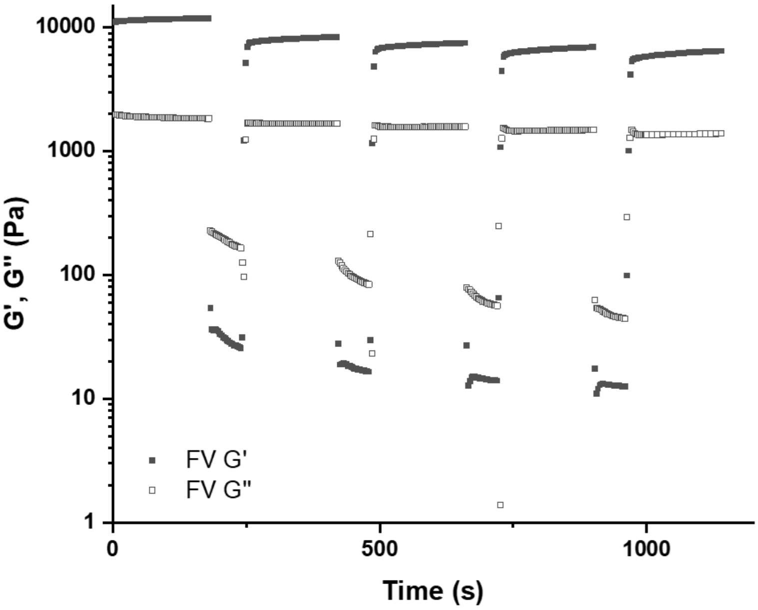

Figure A.2 Oscillatory shear recovery of G′ (filled shapes) and G′′ (hollow shapes) for solvent-triggered NapFV (2 mL, 5 mg ml^{-1}, ϕ_{DMSO} 0.2) gels. Gels were subject to a constant frequency of 10 rad s^{-1} and an alternating strain of 0.5 % (200 s) and 300% (60 s). Destruction of underlying gelator network is seen in periods of high strain, evidenced by G′′ > G′, with recovery of mechanical properties seen upon returning to low strain (G′ < G′′).

Appendix: B

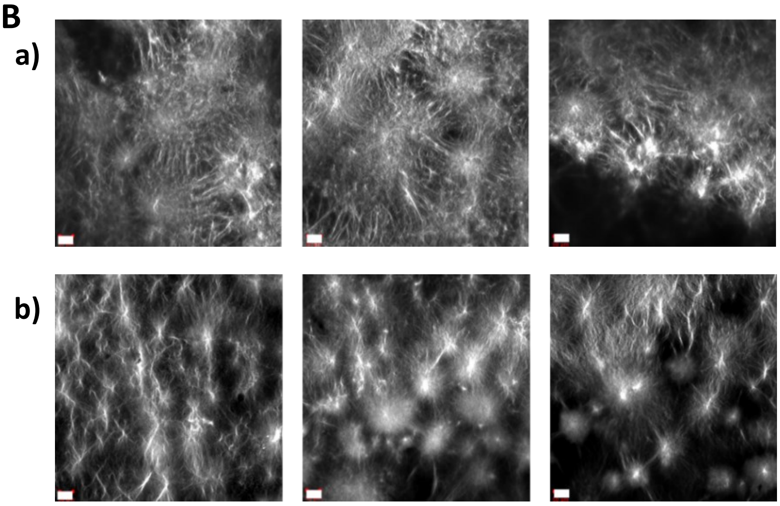

Figure B.1 Supplementary confocal microscopy images of solvent-triggered 2NapFV gels from 3 separate samples in a) 7 mm and b) 15 mm diameter vessels. Scale bars (white) = 50 µm.

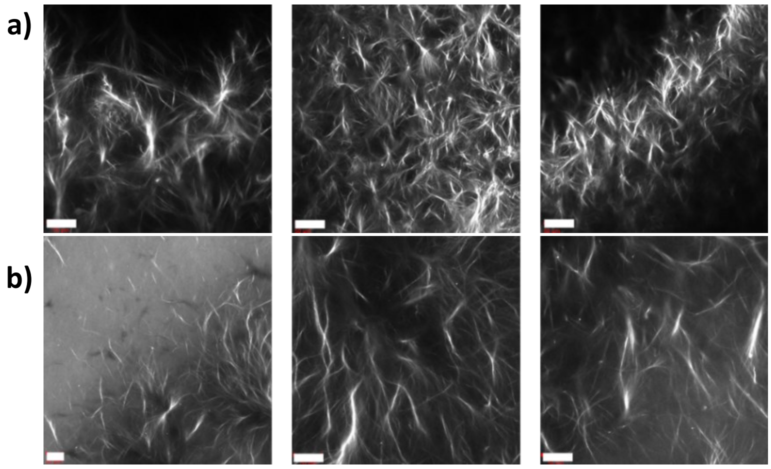

Figure B.2 Supplementary confocal microscopy images of pH-triggered 2NapFV gels from 3 separate samples in a) 7 mm and b) 15 mm diameter vessels. Scale bars (white) = 50 µm.

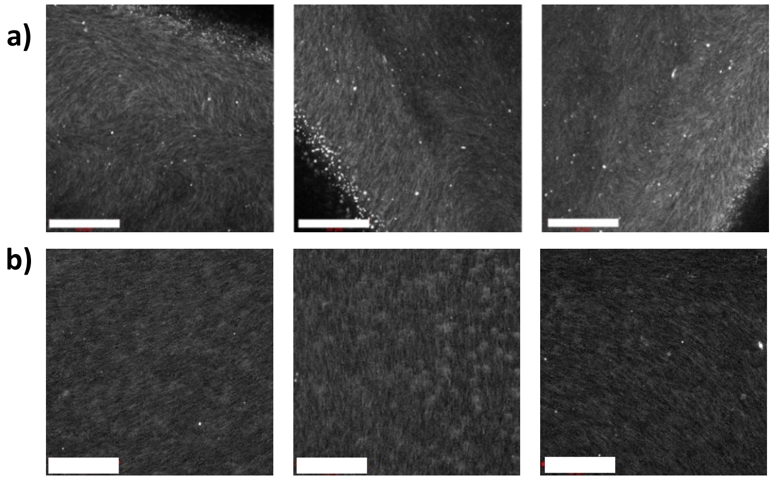

Figure B.3 Supplementary confocal microscopy images of pH-triggered 2NapFF gels from 3 separate samples in a) 7 mm and b) 15 mm diameter vessels. Scale bars (white) = 50 µm.

Appendix: C

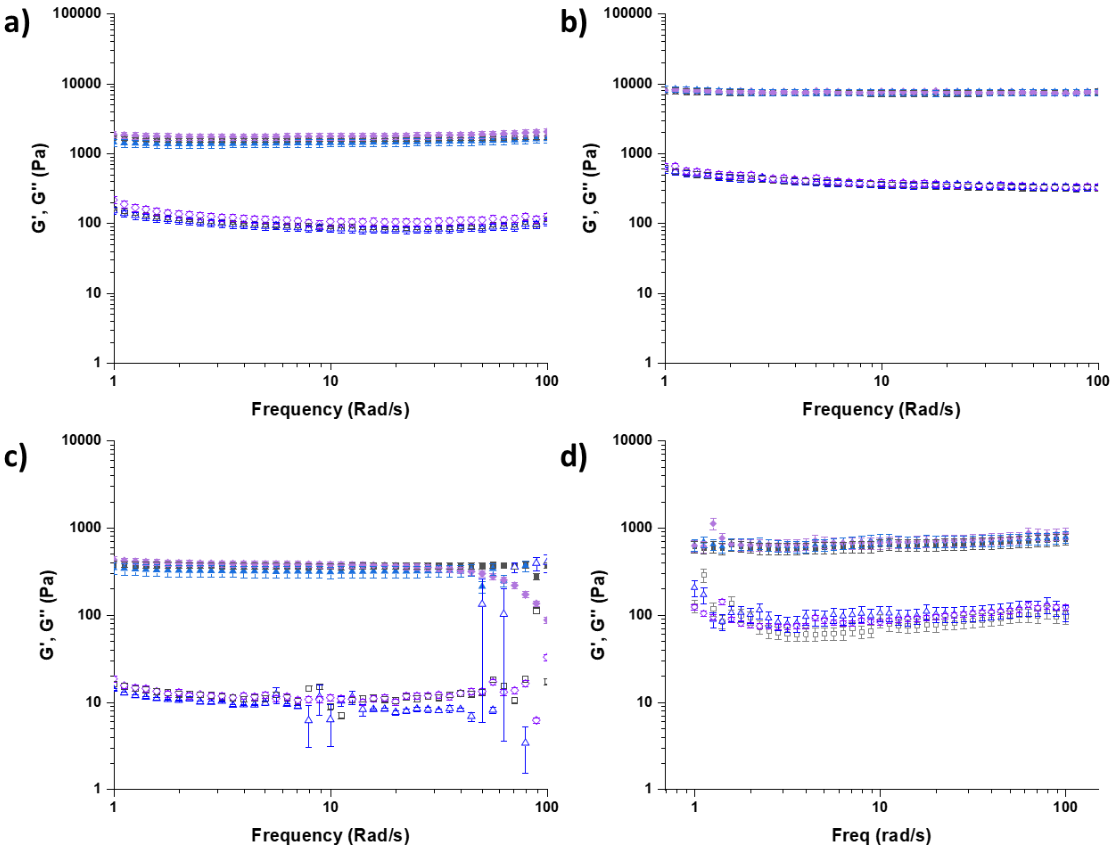

Figure C.1 Rheological frequency sweeps (Strain = 0.25 %, Frequency = 1 – 100 rad s^{-1}) of (a) 2NapFF solvent (5 mg mL^{-1}, 2 mL, 20% DMSO), (b) 2NapFF pH (5 mg mL^{-1}, 2 mL, GdL (8 mg mL^{-1})), (c) agarose (5 mg mL^{-1}, 2 mL,), (d) DBS-hydrazide (4 mg mL^{-1}, 2 mL,) gels. For each experiment: upright gels are shown with grey squares, inverted gels with blue triangles and cut down gels with purple diamonds. G′ and G′′ are represented by solid and hollow shapes respectively.

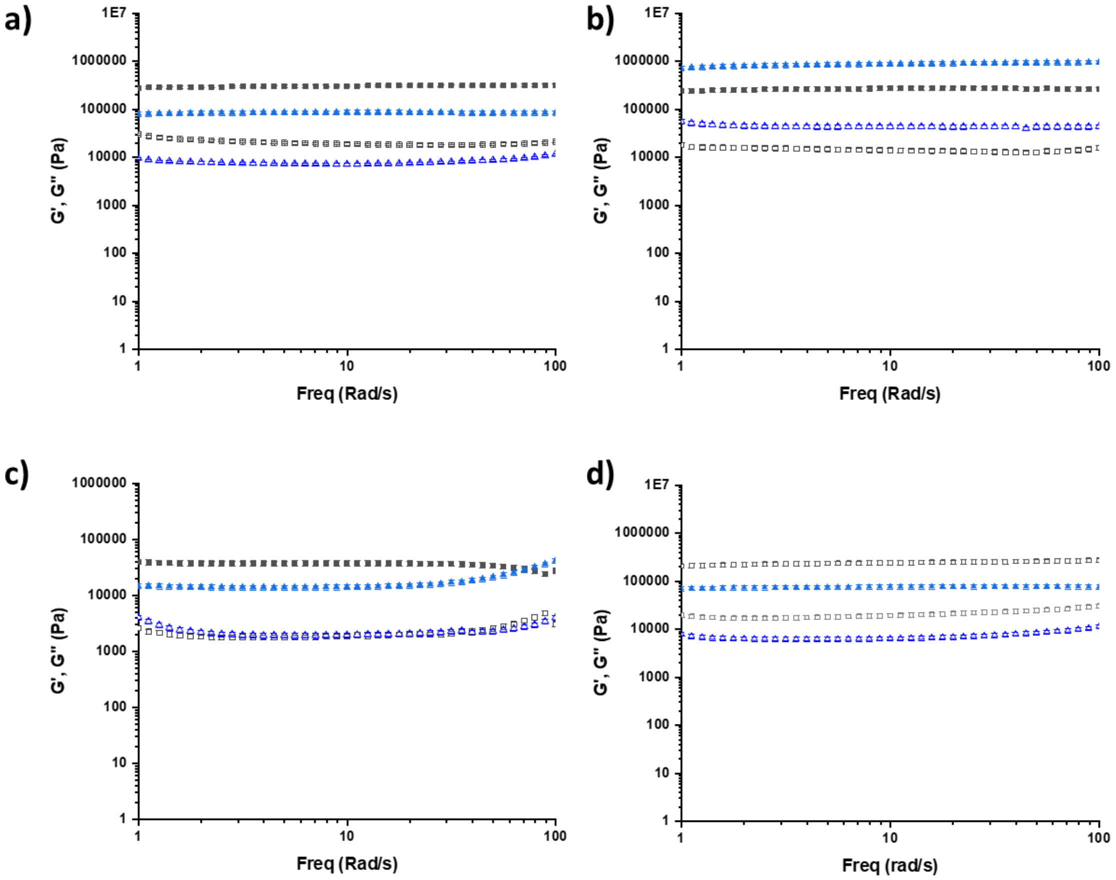

Figure C.2 Rheological frequency sweeps (Strain = 0.025 %, Frequency = 1 – 100 rad s^{-1}) of (a) 2NapFF solvent (5 mg mL^{-1}, 20% DMSO), (b) 2NapFF pH (5 mg mL^{-1}, GdL (8 mg mL^{-1})), (c) agarose (5 mg mL^{-1}), (d) DBS-hydrazide (4 mg mL^{-1}) gels. For each experiment: 2 mL gels are represented by black squares and 0.5 mL gels with blue triangles. G′ and G′′ are represented by solid and hollow shapes respectively.

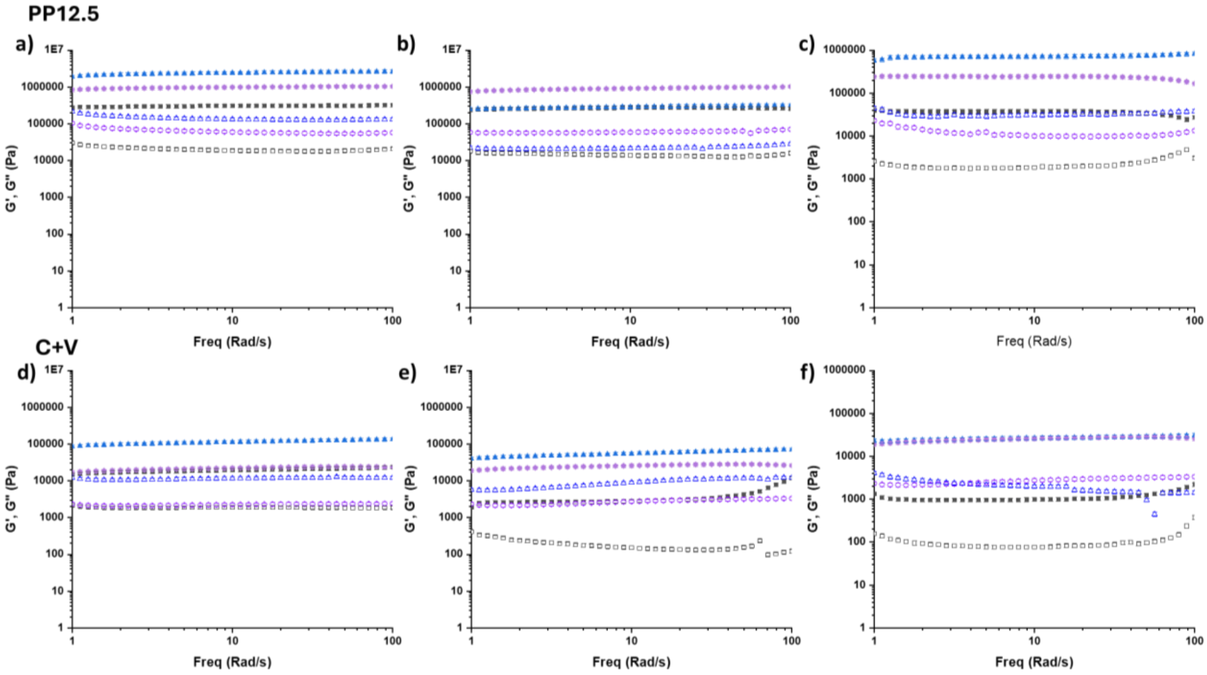

Figure C.3 Rheological frequency sweeps (Strain = 0.025 % (PP12.5) or 0.25 % (C+V), Frequency = 1 – 100 rad s^{-1}) of (a & d) 2NapFF solvent (2 mL, 20% DMSO), (b & e) 2NapFF pH (2 mL, GdL (8 or 24 mg mL^{-1})), (c & f) agarose (2 mL) gels. Gels with a LMWG concentration of 5 mg mL^{-1} are represented by black squares, 15 mg mL^{-1} blue triangles and those with a 9:1 volume composition of 5 mg mL^{-1} to 15 mg mL^{-1} by purple diamonds. G' and G'' are represented by solid and hollow shapes respectively.